Studies on non-oxidative conversion of methane and ethane over metal oxide photocatalysts

Surya Pratap Singh

Table of Contents

Preface

Climate change and the global warming are the main challenges faced by the humanity today in the modern world and the solutions to mitigate their effect are now the need of the hour for the scientific community. Methane is one of the main greenhouse gases which although makes up a tiny fraction of the atmosphere, but is nearly 80 times more powerful in comparison to carbon dioxide in warming the Earth's atmosphere by trapping the heat. Besides curbing the emissions of methane into the atmosphere by various sources of human and livestock origin, conversion of methane to useful chemical feedstock is also needed to be developed. Contrary to the traditional thermal catalysis, photocatalysis is a green technology which can drive various catalytic processes at moderately to room temperature employing the widely available and renewable solar energy. In the present study, we devoted our interest to the photocatalytic conversion of methane and ethane under the non-oxidative reaction conditions and developed various metal oxide photocatalysts for these reactions. The research work was conducted at the Graduate School of Human and Environmental Studies, Kyoto University, Japan under the supervision of Prof. Hisao Yoshida.

Prof. Hisao Yoshida has always been a source of encouragement for the author throughout his stay at the laboratory and the author would like to express his sincere gratitude to him for his guidance, insightful comments, fruitful discussions about the study and for his kindness. The author is very much thankful to Dr. Akira Yamamoto, Assistant Professor, Kyoto University for his help with the experiments and XAFS measurements, sincere comments and discussion during every phase of the progress of the research.

The author would like to appreciate and thank Prof Naoki Komatsu at the Graduate School of Human and Environmental Studies, Kyoto University for the technical support.

The author is also thankful to Dr. Eri Fudo, Prof. Atsuhiro Tanaka, and Prof. Hiroshi Kominami at the Kindai University for their assistance in the performing the TEM and STEM-EDX measurements. The author also thanks Mr. Tsutomu Kiyomura at the Institute for Chemical Research, Kyoto University for the measurements of TEM and STEM-HAADF images.

The author thanks Prof. Setsuhisa Tanabe and Prof. Toshihiro Nakamura at the Graduate School of Human and Environmental Studies, Kyoto University for the evaluation of the doctoral dissertation and their insightful comments to improve this dissertation.

The author also expresses his appreciation to Prof. Tomoko Yoshida at Osaka City University for fruitful discussions at various conferences and warm-hearted advices.

The author also thanks Mr. Satoru Kawaharasaki for the initial investigations to lay the foundation of this study for the author. The author is also very much grateful to Dr. Akihiko Anzai for his support in the beginning of this study, for instructing him the operation of various instruments, sincere discussions and for his heartfelt support. The author is especially grateful to Dr. Tayyebeh Soltani for the collaboration works and for the discussions.

The author expresses his best regard and thanks to Ms. Yuri Bonnitcha, secretary in the Hisao Yoshida Laboratory for her help in the official affairs during the whole period of the author's stay in the laboratory and for her kind support in the settling down in the beginning of his arrival in Japan together with Mr. Daichi Takami. The author also thanks his senior lab-members especially Dr. Akanksha Tyagi and Dr. Xing Zhu for their advices and suggestions. The author is also grateful to his colleagues Mr. Naniwa Shimpei, Mr. Daichi Takami, Mr. Wirya Sarwana, Ryusuke Takioka, Kexin Zou for their friendship and discussions and to all the members of Hisao Yoshida Laboratory for providing a healthy and friendly environment. Then the author would like to thank his Indian friends, Dr. Ashif Equbal, Soumya Sethi, Hardik Tankaria, Siddharth Gavhale and Alisha Yadav for their help in daily life in Kyoto.

Finally, the author sincerely thanks his parents, Mr. Ramnaresh Singh and Mrs. Manorama Chauhan, and his brother, Rashmikant Singh Chauhan for their understanding, support, and encouragement throughout his student life.

Surya Pratap Singh,

Kyoto, Japan.

3rd February 2022

1 General Introduction

1.1 Importance of Methane Conversion

Methane is a compound of carbon with the chemical formula CH_4. It is the simplest hydrocarbon molecule and is a gas under normal conditions. It is present abundantly on the Earth. Methane is the major component of the natural gas and biogas comprising of nearly 85% of the former and 60% of the latter, respectively by volume.[1,2] Methane is also found under the seafloor as methane clathrates (or methane hydrates) containing single methane molecules trapped in the frozen water lattice.[3] Thus, methane is considered as one of the alternatives for carbon and hydrogen to replace the finite resources like petroleum. According to latest IPCC report, methane as a greenhouse gas caused 0.5°C warming since preindustrial times, second only to CO_2.[4] Therefore, the conversion of methane is of utmost importance.

1.2 Methane Conversion Reactions

Traditionally, methane is mainly used as a fuel in the automobile industry and in homes and as a hydrogen source in chemical industry. However, methane is an important carbon source and therefore, the processes for its conversion into value added carbon chemicals need to be devised and developed. There are many catalytic methane conversion reactions with some representative reactions being the steam reforming of methane (SRM) (Table 1, entry 1), the dry reforming of methane (DRM) (Table 1, entry 2), the oxidative coupling of methane (OCM) (Table 1, entry 3), and the non-oxidative coupling of methane (NOCM) (Table 1, entry 4).

Table 1 Representative Methane Conversion Reactions

Entry	Reaction	Chemical Equation	$\Delta_r G^{\ominus}_{298K}$*
(1)	Steam reforming of methane	$CH_4 + H_2O \rightarrow CO + 3H_2$	142
(2)	Dry reforming of methane	$CH_4 + CO_2 \rightarrow 2CO + 2H_2$	204
(3)	Oxidative coupling of methane	$4CH_4 + O_2 \rightarrow 2C_2H_6 + 2H_2O$	-320
		$2CH_4 + O_2 \rightarrow C_2H_4 + 2H_2O$	-288
(4)	Non-oxidative coupling of methane	$2CH_4 \rightarrow C_2H_6 + H_2$	68.6

*The unit of $\Delta_r G^{\ominus}$ is kJ mol^{-1}.

Most of these reactions are thermodynamically not feasible at 298 K indicated by the positive value of Gibbs free energy change (Table 1, entries 1, 2, and 4) due to the very stable C–H bond in the methane molecule (bond-dissociation energy = 434 – 440 kJ mol^{-1})[1] except

of methane oxidation reactions (Table 1, entry 3). Currently, only the SRM is used on the industrial scale in a two-step process involving first converting methane to the syngas (synthetic gas) via the SRM and then transforming syngas into various useful chemicals.[5] Nearly 45 billion kg of methanol and higher alkanes are synthesized from the syngas produced by the steam reforming of natural gas per year.[6] However, it is very difficult to prevent overoxidation to produce CO_2 in the methane reforming reactions such as the SRM as well as the OCM which limits the application of these reactions for the selective formation of desired products.[7] On the other hand, the NOCM is a promising reaction to convert methane directly to ethane and hydrogen through C-H bond activation without the aid of any oxidants (Table 1, entry 4).[8] The products of the NOCM, ethane and hydrogen, are more useful than CO obtained in other methane conversion reactions like the DRM. Since no oxygen is involved in this reaction, the overoxidation to form CO_2 can be avoided unlike SRM and OCM. These characteristics make the NOCM an attractive process for the methane conversion.

1.3 Non-Oxidative Coupling of Methane (NOCM)

The non-oxidative coupling of methane (NOCM) yield ethane and hydrogen from methane (Table 1, entry 4) and both products are useful. Ethane can be used as a starting material to synthesize ethylene while hydrogen can be used as a clean fuel in fuel cells besides being used for the hydrogenation and reduction in chemical industry.

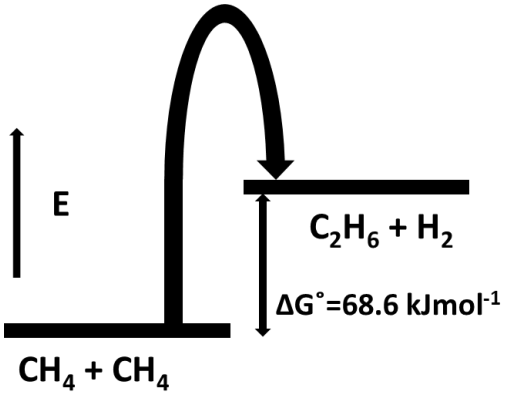

Figure 1 Energy level diagram of the NOCM.

However, as shown in Figure 1, it is an endergonic uphill reaction and is not feasible from a thermodynamic point of view because the value of Gibbs free energy is positive for the NOCM ($\Delta_r G^{\Theta}_{298K}$ = 68.6 kJ mol^{-1}) requiring a high energy input. The non-oxidative methane coupling has been studied at high temperatures.[9–12] Varma *et. al.* obtained a very high selectivity of 90% for the NOCM over the ZSM-5 supported Pt-Bi bimetallic catalysts but the reaction temperature was high like 873-973 K.[12] Achievement of a high methane conversion

requires higher temperatures in the thermal NOCM which makes it an energy-consuming process.[13] Besides, the side reaction of the methane decomposition to form coke is unavoidable at such higher temperatures and the deposition of coke on the surface deactivates the catalyst and limits its lifetime.[7] Thus, using thermal energy with a catalyst is not an effective way for the NOCM.

Photocatalysis is a green approach since it can promote the thermodynamic uphill reactions even around room temperature. A photocatalyst utilize the solar (photo) energy to compensate for the increase of the chemical potential of the products and thus, the reaction can be promoted without significant increase in the temperature. Recently, photocatalysis has been used widely in many reaction systems such as the photocatalytic reduction of carbon dioxide[14] and photocatalytic water splitting.[15] Our research group reported a silica-alumina photocatalyst to be active for the NOCM for the first time in the world in 1998.[16]

1.4 Photocatalytic NOCM

Photocatalytic NOCM utilizes the photo energy in presence of a photocatalyst and so the drawbacks of thermal NOCM like high temperature, high energy intake, coke formation and the deactivation of the catalyst can be avoided. A list of representative works on the photocatalytic NOCM is given in Table 2. After the first report of photocatalytic NOCM over the silica-alumina, numerous studies focused developing new photocatalysts for the NOCM in our group.[17–29] Other research groups also followed these studies and reported some photocatalysts.[30–34]

Table 2 Representative works on the photocatalytic NOCM

Entry	Year	Photocatalyst	Reaction Conditions	Yield of C_2H_6 *	Reference
1	1998	SiO_2	250 W Xe lamp for 18	0.08 %	16
		SiO_2-Al_2O_3	h, 1.0 g sample, 100	3.55 %	
		Al_2O_3	μmol CH_4, closed	3.12 %	
			quartz reactor		
2	2002	SiO_2-TiO_2	250 W Xe lamp for 3 h,	0.09 %	17
		SiO_2-Al_2O_3-TiO_2	1.0 g sample, 200 μmol	2.07 %	
		Al_2O_3-TiO_2	CH_4, closed quartz	0.43 %	
			reactor		
3	2002	H-form	250 W Xe lamp for 3 h,	0.111 %	18
		modernite	1.0 g sample, 200 μmol		

			CH_4, closed quartz reactor		
4	2003	ZrO_2/SiO_2	250 W Xe lamp for 3 h, 0.5 g sample, 200 μmol CH_4, closed quartz reactor	0.109 %	22
5	2005	Ce/SiO_2 Ce/Al_2O_3	300 W Xe lamp for 3 h, 0.2 g sample, 200 μmol CH_4, closed quartz reactor	0.12 μmol 0.15 μmol	26
6	2005	MgO/SiO_2	300 W Xe lamp for 3 h, 0.2 g sample, 200 μmol CH_4, closed quartz reactor	0.028 %	27
7	2006	$Ce/Ti/SiO_2$	300 W Xe lamp for 3 h, 0.2 g sample, 200 μmol CH_4, closed quartz reactor	0.117 %	28
8	2006	MCM-41 FSM-16	300 W Xe lamp for 3 h, 0.2 g sample, 200 μmol CH_4, closed quartz reactor	0.042 % 0.054 %	29
9	2006	TS	300 W Xe lamp for 3 h, 0.2 g sample, 200 μmol CH_4, closed quartz reactor	0.20 %	19
10	2008	Ga/SiO_2 Ga_2O_3	300 W Xe lamp for 3 h, 0.2 g sample, 200 μmol CH_4, closed quartz reactor	0.067 % 0. 16 %	21
11	2011	Zn^+-ZSM-5	150 W high-pressure Hg lamp for 8 h, 1.0 g	23.4 μmol	30

			sample, 200 μmol CH_4, closed quartz reactor		
12	2018	Au/ZnO	300 W Xe lamp for 4 h, 1 mg sample, 0.5 mL CH_4, Schlenk flask reactor	~ 45 μmol g^{-1}	31
13	2019	Pt/HGTS	300 W Xe lamp for 4 h, 0.2 g sample, 44.6 μmol CH_4, closed quartz reactor	0.102 μmol	32
14	2020	Au/TiO_2	300 W Xe lamp with AM 1.5G filter, 5 mg sample, 10% CH_4 in Ar, flow reactor	81.7 μmol $g_{catalyst}^{-1}$ h^{-1}	33
15	2021	Nb-TS	300 W Xe lamp for 4 h, 0.1 g sample, 1 mL CH_4, closed quartz reactor	~ 1.75 μmol g^{-1} h^{-1}	34

*The yield of ethane production was reported with the optimized photocatalyst. It is not appropriate to compare the yield of ethane with various photocatalysts since the NOCM reaction tests were performed at different reaction conditions and the yields are also reported in different units. Moreover, the photocatalytic production rate of ethane was not proportional to the weight of the photocatalyst.

Most of these photocatalysts are based on the insulator supports such as SiO_2, Al_2O_3 and molecular sieves. Broadly, the photocatalysts for the NOCM can be divided into two categories: quantum photocatalysts and semiconductor photocatalysts.

1.4.1 Quantum Photocatalysts

The photocatalysts based on the insulator support material such as SiO_2 and where a metal atom/ion is dispersed in the matrix of these insulator supports such as SiO_2–Al_2O_3 and ZrO_2/SiO_2; etc., are called quantum photocatalysts. These insulators are quite stable in the non-oxidative reaction conditions of the NOCM and thus, the stability in the reductive (or non-oxidative) reaction conditions of the NOCM is a prerequisite for a photocatalyst to be active for this reaction. The active sites for the NOCM over the quantum photocatalyst are not very

clear. On the pure SiO_2, photoabsorption sites are generated through the dehydroxylation of the surface hydroxyl groups when the silica is evacuated at high temperature before the reaction test.[29] A non-bridging oxygen hole centre (NBOHC, ≡Si–O•) and an E′ centre (≡Si•) were clarified to be the photoactive sites for the NOCM[35] as shown below in eq. 1.

$$\equiv Si–OH + \equiv Si–OH \rightarrow \equiv Si–O^{\bullet} + \equiv Si^{\bullet} + H_2O \quad (1)$$

Other mesoporous silica materials like FSM-16, and MCM-41 showed higher activity than amorphous SiO_2 sample and the similar kind of photoactive surface sites were proposed.[29] The formation and the photoexcitation of these surface sites is shown in Figure 2. Although the mechanism is not clarified, it is considered that the methane molecules are adsorbed on the surface and the photoenergy is transferred to the adsorbed methane molecules through these active sites. Another possibility involving the complex formation of the adsorbed methane and active sites is discussed and this complex is excited by the photoenergy. Subsequently methyl and hydrogen radicals are formed, react with another methane molecule and couple to yield ethane and hydrogen. However, the structure of the surface complex and the intermediate is not clarified.

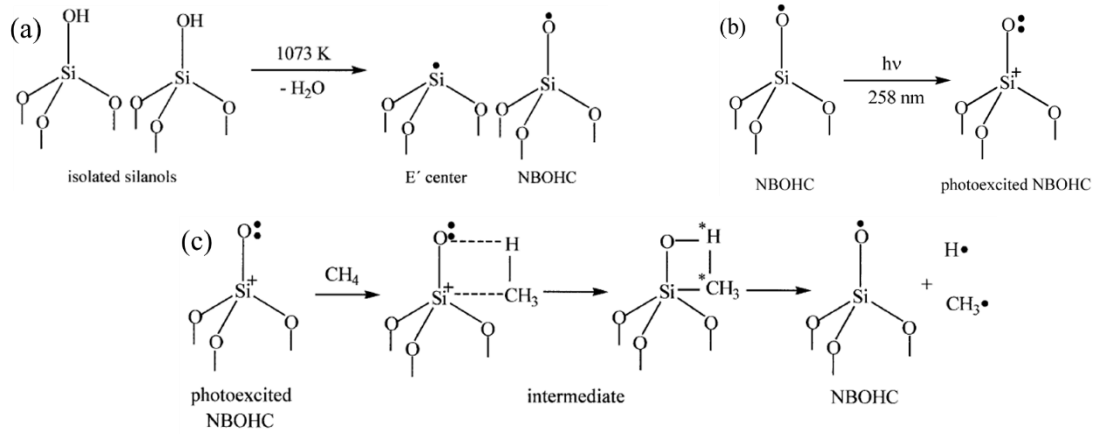

Figure 2 (a) Generation and (b) photoexcitation of the active sites on pure silica materials, and (c) tentatively proposed first step in NOCM.

When a small amount of metal cations such as Mg, Zr, Al; etc. were incorporated, the activity of the amorphous silica was increased.[22,23,27] When the sample was treated at high temperature (1073 K), a fine photoluminescence spectrum was obtained (Figure 3a), and it can be assigned to the vibrational levels of the excited localized site of highly dispersed metal oxide on silica (Si-O-M linkage). The properties of the emission sites and the photocatalytic activities were related to each other (Figure 3b), and the photoexcitation was proposed to occur in the Si–O moiety next to metal cation as shown below in Figure 3c. This structure of the active site would be common in the silica-based quantum photocatalysts.

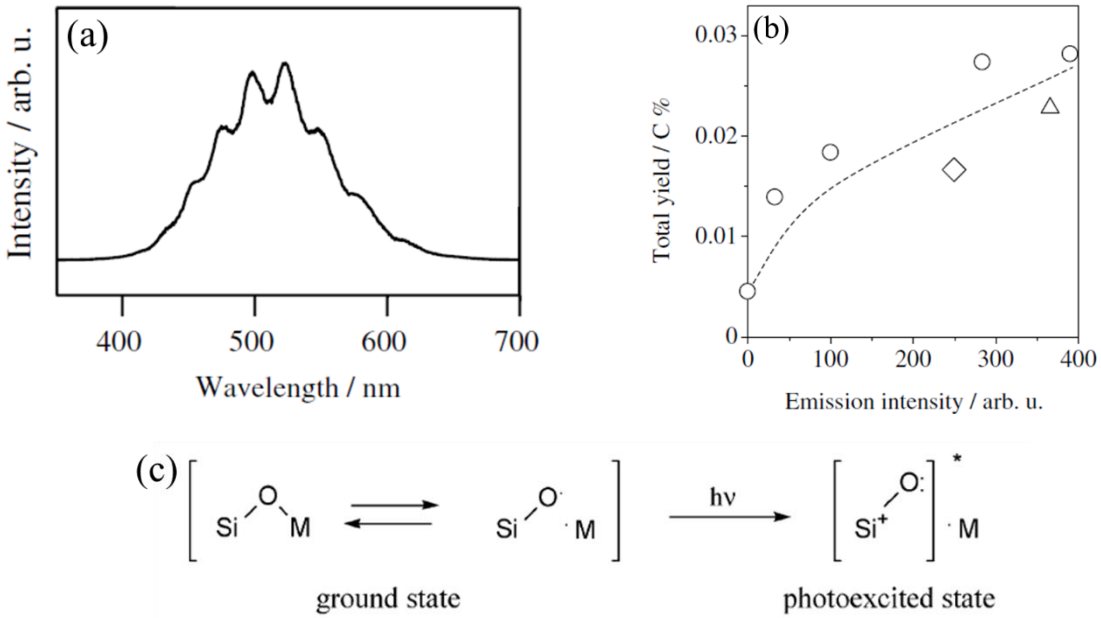

Figure 3 (a) Fine photoluminescence spectrum typical to highly dispersed metal oxides on silica such as Al_2O_3-SiO_2, ZrO_2/TiO_2, and MgO/SiO_2; etc measured at 77 K. The excitation wavelength was 300 nm. (b) The relationship between the intensity of the fine structural phosphorescence emission spectra of silica-based quantum photocatalysts and total yield in the photoinduced direct methane coupling on them. Silica based quantum photocatalysts were silica-alumina (triangle), silica-supported zirconia (diamond), and silica-supported magnesia (circle), and (c) plausible model of photoactive sites on a silica-based quantum photocatalyst; where, M = metal atom/ion.

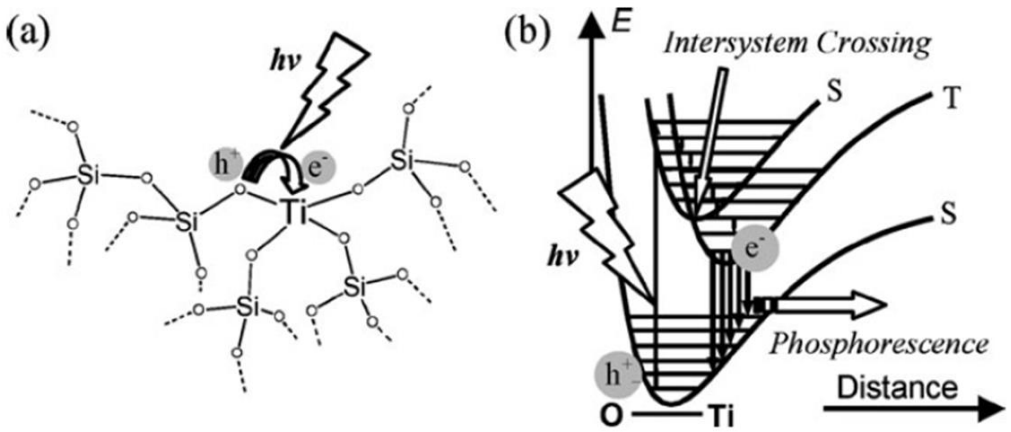

Figure 4 Highly dispersed titanium species in silica matrix, (a) a model of the photoactive tetrahedral titanium sites on silica, and (b) a schematic model for the photoexcitation localized at Ti–O species and phosphorescence emission from the site

The silica-titania (TS) photocatalyst prepared by either impregnation method or sol-gel method with the low loading of Ti also exhibited the activity for the NOCM.[36] The highly dispersed tetrahedral titanium oxide species Ti(T_d) were the active species where the loading amount of Ti was less than 1 mol%. When the loading amount of Ti was increased, the octahedral TiO_2 like nanoparticles were formed and, only hydrocarbons and no hydrogen were

produced in the reaction test. These results suggest that the highly dispersed Ti sites are the active sites in the silica-titania photocatalyst (Figure 4). No hydrogen production over the photocatalysts with medium or high loading amount of Ti should be due to the possible reduction of TiO_2 nanoparticles. Further, a ternary oxide, SiO_2–Al_2O_3–TiO_2 prepared by the sol-gel method showed the higher activity than silica-alumina (SiO_2–TiO_2).[17,25] The coexistence of dispersed tetrahedral AlO_4 and dispersed tetrahedral TiO_2 in silica matrix is responsible for the higher activity. A possible structure of synergistic species would be described as $(SiO)_3Ti$–O–$Al(OSi)_3$ containing the Ti–O–Al moiety where the LMCT (ligand-to-metal charge transfer) from the lattice oxygen, O^{2-} to Ti^{4+} can take place at the Ti^{4+}– O^{2-}–Al^{3+} moiety.

Similarly, the silica supported ceria samples with low loading amount of cerium showed the activity and the highly dispersed Ce(III) oxide species were suggested to be the active sites for the NOCM.[20,26] The samples with high loading amount of Ce showed lower production since these samples would have CeO_2 like nanoparticles which are not active for the NOCM owing to the reduction of Ce(IV) species by the produced hydrogen. Unlike other silica-supported highly dispersed photocatalysts, the silica-supported ceria did not require high pretreatment temperature for higher activity. Thus, the photoactive sites would also be different from the Si–O moiety formed upon dehydroxylation at high pretrreatment temperature. In the highly dispersed Ce(III) species on SiO_2, the absorption and the photoexcitation would occur through a *f-d* transition of Ce(III) ions or electron charge transfer from oxygen to Ce(III) (LMCT, ligand-to-metal charge transfer). Further, highly dispersed cerium oxide on silica was modified with highly dispersed titanium oxide ($Ce/Ti/SiO_2$) and the activity became higher and it was close to the sum of that over the Ce/SiO_2 and the Ti/SiO_2 samples.[28,37] Both highly dispersed Ce(III) and Ti(IV) tetrahedral species coexisting on the $Ce/Ti/SiO_2$ sample showed the higher activity.

Gallium oxide existing as highly dispersed tetrahedral species on silica also showed selective NOCM.[21]

H-zeolites (H-form modernite and ZSM-5) were also found to be active for the NOCM and the highly dispersed framework Al-O units interacting with no metal ions such as AlO–$(SiO)_3$–Al were proposed to be the active sites.[18] Later, a Zn^+-modified ZSM-5 was developed as an efficient photocatalyst for the NOCM where the electron transfer from the zeolite framework to the zinc centre would happen on UV-light irradiation and this 4s electron of the Zn^+ transfers to the antibonding C-H orbital of the methane for its activation.[30]

The conversion of methane is limited on the silica-based highly dispersed photocatalysts since the photoactive sites are localized (or quantized) on certain limited species. Moreover, the mechanism of NOCM over the quantum photocatalysts is somewhat ambiguous and these limitations hinder the development of such photocatalysts. *In-situ* techniques of XAFS, vibration spectroscopy, and EPR spectroscopy should be used to gain further insight into the mechanism.

1.4.2 Semiconductor Photocatalyst

Another kind of photocatalyst for the NOCM is based on semiconductor photocatalysts. A typical mechanism of the photoexcitation in the semiconductor photocatalyst is shown in Figure 5.

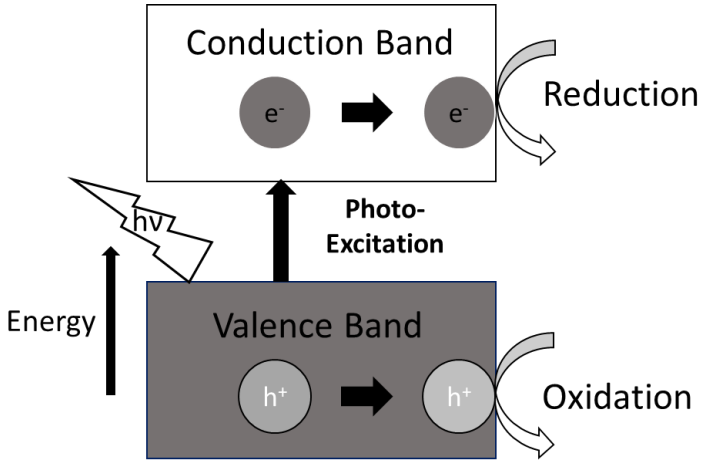

Figure 5 Mechanism of photoexcitation in a semiconductor photocatalyst

We reported the Ga_2O_3 to be the first semiconductor photocatalyst active for the NOCM.[21] Gallium oxide is a wide band gap semiconductor photocatalyst (band gap ≈ 4.6 eV). The valence band primarily consists of O 2p orbitals, and the conduction band primarily consists of Ga 2s orbitals in the gallium oxide semiconductor photocatalyst. Thus, the gallium oxide can be excited by the UV light with the wavelengths shorter than 290 nm.

Au/ZnO porous nanosheets were reported to be active for the NOCM where both the ZnO semiconductor photocatalyst and the Au plasmonic nanoparticles acted synergistically to absorb the UV-light (320-400 nm) and the visible light (400-800 nm), respectively to enhance the ethane yield.[31] Besides absorbing the photons upon UV-light irradiation, ZnO nanosheets also provided intrinsic electric field (IEF) to polarize and dissociate the C-H bond in methane and also to separate the photogenerated electron-hole pairs. However, the photocatalyst was deactivated quickly after one cycle due to the accumulation of excessive holes in the bulk of

ZnO. Another such photocatalyst is Au/TiO_2, which showed very high production rates of ethane such as 81.7 μmol $g_{catalyst}^{-1}$ h^{-1}, but unfortunately this photocatalyst was also not stable under the reductive reaction conditions of the NOCM.[33]

Further, doping of Ga and Nb in the TiO_2-SiO_2 framework is employed to develop the activity for the NOCM in the Pt-loaded Ga-doped TiO_2-SiO_2 sample and the Nb-doped TiO_2-SiO_2 samples, respectively, where the TiO_2 acted as a semiconductor photocatalyst under light irradiation.[32,34]

Some feats like the long-term stability of the photocatalyst under the reductive reaction conditions of the NOCM, i.e.; the presence of methane, ethane and hydrogen upon photoirradiation, selective production of ethane and hydrogen, and high activity in the photocatalytic NOCM are yet to be achieved. Unlike titanium dioxide and zinc oxide, gallium oxide is a stable semiconductor photocatalyst and the purpose of this study is to k]increase the activity of the gallium oxide by its surface modification by some strategies like loading with the cocatalysts for the selective production of ethane and hydrogen from methane in the photocatalytic NOCM. The mechanism and the long-term stability of these photocatalysts for the NOCM is also to be tested. Since ethane is obtained selectively as a main product in the NOCM, we further plan to test the activity of the same photocatalyst employed in the NOCM for the non-oxidative direct ethane conversion to produce butane or ethene since both ethene and butane are important chemical feedstocks.

References

(1) Yuliati, L.; Yoshida, H. Photocatalytic Conversion of Methane. *Chem. Soc. Rev.* **2008**, *37* (8), 1592–1602.

(2) Wang, S. Shale Gas Exploitation: Status, Problems and Prospect. *Nat. Gas Ind. B* **2018**, *5* (1), 60–74.

(3) Chong, Z. R.; Yang, S. H. B.; Babu, P.; Linga, P.; Li, X. Sen. Review of Natural Gas Hydrates as an Energy Resource: Prospects and Challenges. *Appl. Energy* **2016**, *162*, 1633–1652.

(4) Control Methane to Slow Global Warming — Fast. *Nature* **2021**, *596* (7873), 461.

(5) Caballero, A.; Pérez, P. J. Methane as Raw Material in Synthetic Chemistry: The Final Frontier. *Chem. Soc. Rev.* **2013**, *42* (23), 8809–8820.

(6) Sousa-Aguiar, E. F.; Noronha, F. B.; Faro, A. The Main Catalytic Challenges in GTL (Gas-to-Liquids) Processes. *Catal. Sci. Technol.* **2011**, *1* (5), 698–713.

(7) Li, Z.; Yi, Z.; Li, Z.; Zou, Z. Photocatalytic and Thermocatalytic Conversion of Methane. *Sol. RRL* **2021**, *5* (6), 1–17.

(8) Choudhary, T. V.; Aksoylu, E.; Goodman, D. W. Nonoxidative Activation of Methane. *Catal. Rev. - Sci. Eng.* **2003**, *45* (1), 151–203.

(9) Moya, S. F.; Martins, R. L.; Ota, A.; Kunkes, E. L.; Behrens, M.; Schmal, M. Nanostructured Supported Palladium Catalysts - Non-Oxidative Methane Coupling. *Appl. Catal. A Gen.* **2012**, *411–412*, 105–113.

(10) Kim, S. K.; Kim, H. W.; Han, S. J.; Lee, S. W.; Shin, J.; Kim, Y. T. Mechanistic and Microkinetic Study of Non-Oxidative Methane Coupling on a Single-Atom Iron Catalyst. *Commun. Chem.* **2020**, *3* (1), 1–8.

(11) Guczi, L.; Sarma, K. V.; Borkó, L. Non-Oxidative Methane Coupling over Co-Pt/NaY Bimetallic Catalysts. *Catal. Letters* **1996**, *39* (1–2), 43–47.

(12) Xiao, Y.; Varma, A. Highly Selective Nonoxidative Coupling of Methane over Pt-Bi Bimetallic Catalysts. *ACS Catal.* **2018**, *8* (4), 2735–2740.

(13) Guo, X.; Fang, G.; Li, G.; Ma, H.; Fan, H.; Yu, L.; Ma, C.; Wu, X.; Deng, D.; Wei, M.; Tan, D.; Si, R.; Zhang, S.; Li, J.; Sun, L.; Tang, Z.; Pan, X.; Bao, X. Direct, Nonoxidative Conversion of Methane to Ethylene, Aromatics, and Hydrogen. *Science (80-.).* **2014**, *344* (6184), 616–619.

(14) Ishii, T.; Anzai, A.; Yamamoto, A.; Yoshida, H. Calcium Zirconate Photocatalyst and Silver Cocatalyst for Reduction of Carbon Dioxide with Water. *Appl. Catal. B Environ.*

2020, *277*, 119192.

(15) Takata, T.; Jiang, J.; Sakata, Y.; Nakabayashi, M.; Shibata, N.; Nandal, V.; Seki, K.; Hisatomi, T.; Domen, K. Photocatalytic Water Splitting with a Quantum Efficiency of Almost Unity. *Nature* **2020**, *581* (7809), 411–414.

(16) Kato, Y.; Yoshida, H.; Hattori, T. Photoinduced Non-Oxidative Coupling of Methane over Silica-Alumina and Alumina around Room Temperature. *Chem. Commun.* **1998**, No. 21, 2389–2390.

(17) Kato, Y.; Matsushita, N.; Yoshida, H.; Hattori, T. Highly Active Silica-Alumina-Titania Catalyst for Photoinduced Non-Oxidative Methane Coupling. *Catal. Commun.* **2002**, *3* (3), 99–103.

(18) Kato, Y.; Yoshida, H.; Satsuma, A.; Hattori, T. Photoinduced Non-Oxidative Coupling of Methane over H-Zeolites around Room Temperature. *Microporous Mesoporous Mater.* **2002**, *51* (3), 223–231.

(19) Yuliati, L.; Itoh, H.; Yoshida, H. Preparation of Isolated Highly Dispersed Titanium Oxides on Silica by Sol-Gel Method for Photocatalytic Non-Oxidative Direct Methane Coupling. *Stud. Surf. Sci. Catal.* **2006**, *162*, 961–968.

(20) Yuliati, L.; Hamajima, T.; Hattori, T.; Yoshida, H. Nonoxidative Coupling of Methane over Supported Ceria Photocatalysts. *J. Phys. Chem. C* **2008**, *112* (18), 7223–7232.

(21) Yuliati, L.; Hattori, T.; Itoh, H.; Yoshida, H. Photocatalytic Nonoxidative Coupling of Methane on Gallium Oxide and Silica-Supported Gallium Oxide. *J. Catal.* **2008**, *257* (2), 396–402.

(22) Yoshida, H.; Chaskar, M. G.; Kato, Y.; Hattori, T. Active Sites on Silica-Supported Zirconium Oxide for Photoinduced Direct Methane Conversion and Photoluminescence. *J. Photochem. Photobiol. A Chem.* **2003**, *160* (1–2), 47–53.

(23) Yoshida, H.; Matsushita, N.; Kato, Y.; Hattori, T. Active Sites in Sol-Gel Prepared Silica-Alumina for Photoinduced Non-Oxidative Methane Coupling. *Phys. Chem. Chem. Phys.* **2002**, *4* (11), 2459–2465.

(24) Yoshida, H.; Chaskar, M. G.; Kato, Y.; Hattori, T. Fine Structural Photoluminescence Spectra of Silica-Supported Zirconium Oxide and Its Photoactivity in Direct Methane Conversion. *Chem. Commun.* **2002**, *2* (18), 2014–2015.

(25) Yoshida, H.; Matsushita, N.; Kato, Y.; Hattori, T. Synergistic Active Sites on SiO_2−Al_2O_3−TiO_2 Photocatalysts for Direct Methane Coupling. *J. Phys. Chem. B* **2003**, *107* (33), 8355–8362.

(26) Yuliati, L.; Hamajima, T.; Hattori, T.; Yoshida, H. Highly Dispersed Ce(III) Species on

Silica and Alumina as New Photocatalysts for Non-Oxidative Direct Methane Coupling. *Chem. Commun.* **2005**, No. 38, 4824–4826.

(27) Yuliati, L.; Hattori, T.; Yoshida, H. Highly Dispersed Magnesium Oxide Species on Silica as Photoactive Sites for Photoinduced Direct Methane Coupling and Photoluminescence. *Phys. Chem. Chem. Phys.* **2005**, *7* (1), 195–201.

(28) Yuliati, L.; Itoh, H.; Yoshida, H. Modification of Highly Dispersed Cerium Oxides on Silica with Highly Dispersed Titanium Oxides as a New Photocatalyst Design for Nonoxidative Direct Methane Coupling. *Chem. Lett.* **2006**, *35* (8), 932–933.

(29) Yuliati, L.; Tsubota, M.; Satsuma, A.; Itoh, H.; Yoshida, H. Photoactive Sites on Pure Silica Materials for Nonoxidative Direct Methane Coupling. *J. Catal.* **2006**, *238* (1), 214–220.

(30) Li, L.; Li, G. D.; Yan, C.; Mu, X. Y.; Pan, X. L.; Zou, X. X.; Wang, K. X.; Chen, J. S. Efficient Sunlight-Driven Dehydrogenative Coupling of Methane to Ethane over a Zn+-Modified Zeolite. *Angew. Chemie - Int. Ed.* **2011**, *50* (36), 8299–8303.

(31) Meng, L.; Chen, Z.; Ma, Z.; He, S.; Hou, Y.; Li, H. H.; Yuan, R.; Huang, X. H.; Wang, X.; Wang, X.; Long, J. Gold Plasmon-Induced Photocatalytic Dehydrogenative Coupling of Methane to Ethane on Polar Oxide Surfaces. *Energy Environ. Sci.* **2018**, *11* (2), 294–298.

(32) Wu, S.; Tan, X.; Lei, J.; Chen, H.; Wang, L.; Zhang, J. Ga-Doped and Pt-Loaded Porous TiO_2-SiO_2 for Photocatalytic Nonoxidative Coupling of Methane. *J. Am. Chem. Soc.* **2019**, *141* (16), 6592–6600.

(33) Lang, J.; Ma, Y.; Wu, X.; Jiang, Y.; Hu, Y. H. Highly Efficient Light-Driven Methane Coupling under Ambient Conditions Based on an Integrated Design of a Photocatalytic System. *Green Chem.* **2020**, *22* (14), 4669–4675.

(34) Chen, Z.; Wu, S.; Ma, J.; Mine, S.; Toyao, T.; Matsuoka, M.; Wang, L.; Zhang, J. Non-oxidative Coupling of Methane: N-type Doping of Niobium Single Atoms in TiO_2–SiO_2 Induces Electron Localization. *Angew. Chem. Int. Ed.* **2021**, *60*, 11901–11909.

(35) Yoshida, H. Active Sites of Silica-Based Quantum Photocatalysts for Non-Oxidative Reactions. *Catal. Surv. from Asia* **2005**, *9* (1), 1–9.

(36) Yuliati, L.; Itoh, H.; Yoshida, H. Photocatalytic Direct Conversion of Methane on Silica-Titania Catalysts. *Stud. Surf. Sci. Catal.* **2007**, *172*, 457–460.

(37) Yoshida, H.; Yuliati, L.; Itoh, H. Highly Dispersed Cerium and Titanium Oxides on Silica Prepared by Impregnation Method for Photocatalytic Non-Oxidative Direct Methane Coupling; *Stud. Surf. Sci. Catal.* **2006**, *162*, 1025–1032.

2 Non-oxidative coupling of methane over Pd-loaded gallium oxide photocatalysts in a flow-reactor

Abstract

Photocatalytic methane conversion is attractive for utilization of renewable biogas and solar energy to directly produce useful compounds. In the present study, gallium oxide (Ga_2O_3) photocatalyst was examined for non-oxidative coupling of methane (NOCM) around room temperature in a flow reactor. It was found that ethane and hydrogen were continuously yielded at constant rate from methane upon photoirradiation around room temperature and atmospheric pressure, confirming that NOCM can be promoted photocatalytically over Ga_2O_3 in a flow reactor. In addition, Pd cocatalyst was found to improve the activity of the Ga_2O_3 photocatalyst for NOCM and achieve more than three times higher production rate of ethane such as 0.22 μmol h^{-1} in a flow of 10% methane at 30 mL min^{-1} with 0.8 g of photocatalyst. The methane conversion achieved to 0.006% within a short contact time of 0.8 s, which is higher than the thermodynamically equilibrium conversion value.

2.1 Introduction

Non-oxidative coupling of methane (NOCM) is an attractive reaction for the production of ethane and hydrogen from methane directly without aid of any oxidant (eq. 1).[1]

$$2\ CH_4 \rightarrow C_2H_6 + H_2,\ \ \Delta_r G^{\Theta}_{298K}=68.6\ \text{kJ mol}^{-1} \qquad (1)$$

This is, however, a thermodynamically unfavorable endergonic reaction and the equilibrium constant and equilibrium conversion of this reaction at 298 K are very low such as 9.5×10^{-13} and 0.0002 %, respectively, meaning that this reaction does not take place at 298 K in practice [2]. Although the equilibrium conversion becomes higher at higher temperatures, such as 1.1% and 7.2% at 800 K and 1273 K, respectively, the methane decomposition (MD) to carbon and hydrogen (eq. 2) is not negligible at temperatures higher than 800 K because it is thermodynamically more favorable than NOCM [2].

$$CH_4 \rightarrow C + 2H_2, \qquad \Delta_r G^{\Theta}_{298K}=50.7\ \text{kJ mol}^{-1} \qquad (2)$$

Photocatalytic NOCM is an alternative approach to activate the C–H bond in methane by using photoenergy in presence of a photocatalyst and thus, to carry out the reaction at nearly room temperature.[2] Bare Ga_2O_3 has been found to function as a photocatalyst for the NOCM. But a closed reactor was used in those studies which is not good for industrial scale use.[3,4] Ga_2O_3 is also reported to be active for other photocatalytic reactions such as water splitting,[5–7] organic compound photodegradation[8,9], photocatalytic carbon dioxide reduction with hydrogen[10] or water,[11–15] and photocatalytic reforming of methane with carbon dioxide.[4] In the present study, we examined the NOCM over the Ga_2O_3 in a flow reactor. A flow reactor is easy to scale-up. Also, the use of a flow reactor enables measurements of exact and real time reaction rates when coupled with online gas chromatographs (GC). The residence time (or contact time) of the reactants and products can be varied when we use a flow reactor and thus can avoid formation of undesired products which are thermodynamically more stable. But flow reactors are not so sensitive as the closed reactor for very small production rates and so we examined whether or not the products can be detected using the flow reactor. The activity over the bare gallium oxide sample was low and in order to increase its activity, we employed the surface modification approach with cocatalysts. We deposited some cocatalysts on the Ga_2O_3 particles by impregnation method and examined their activity and found that a Pd-loaded Ga_2O_3 photocatalyst showed selective NOCM with an increase in the ethane production rates more than 3 times in comparison to bare gallium oxide.

2.2 Experimental Section

2.2.1 Materials and Methods

The employed Ga_2O_3 sample was commercially obtained (Ga_2O_3, 99.90%, Kojundo Chemical Laboratory). The following chemicals were used as precursors of additives, $Pt(NH_3)_4(NO_3)_2$ (99.0%, Nacalai Tesque), $RhCl_3$ (98%, Wako Pure Chemical), $PdCl_2$ (99%, Kishida Chemical), $AgNO_3$ (99.8%, Kishida Chemical), $Ni(NO_3)_2{\cdot}6H_2O$ (99.9%, Wako Pure Chemical), $Fe(NO_3)_3{\cdot}9H_2O$ (99%, Nacalai Tesque), $In(NO_3)_3{\cdot}3H_2O$ (98% Kishida Chemical), $Zn(NO_3)_2{\cdot}6H_2O$ (99%, Nacalai Tesque), and $Sm(NO_3)_3{\cdot}6H_2O$ (99.5%, Wako Pure Chemical). Each additive metal or metal oxide was loaded on the Ga_2O_3 sample by an impregnation method and the procedure is as follows. The Ga_2O_3 powder sample (2.0 g) was stirred in an aqueous solution of the precursor (100 mL) at room temperature for 30 min, followed by heating at 353 K to evaporate water to dryness. The obtained powder was dried at 373 K overnight and calcined in an alumina crucible by using an electric muffle furnace at 673 K for 2 h. The metal- or metal oxide-loaded samples are referred to as M(*x*)/Ga_2O_3 sample, where *x* in wt. % shows loading amount of the additive (M) calculated as a metal state even if it was oxidized, for example, Pd(0.5)/Ga_2O_3.

2.2.2 Characterization

The obtained samples were characterized by several techniques. The crystal structure was determined by powder X-ray diffraction with a Shimadzu LabX XRD-6000 X-ray diffractometer using Cu K_α radiation (40 kV, 30 mA). Scanning electron microscope (SEM) images were recorded on a JEOL model JSM-890 scanning microscope. Diffuse reflectance UV-visible spectra were recorded by a JASCO V-570 UV/VIS/NIR spectrophotometer equipped with an integrating sphere covered with a $BaSO_4$ reference. The BET specific surface area of the Ga_2O_3 sample was measured by a Quantachrome Monosorb rapid surface area analyzer.

2.2.3 Experimental Set-up

The photocatalytic activity test for the NOCM was carried out using a flow reactor shown in Figure 1.[16–19] The catalyst powder was pressed under 40 MPa pressure and ground into granules of 297–707 μm (25–50 mesh). The sample granules (0.8 g) were placed into a quartz cell (2 × 2 × 0.1 cm^3, see the photograph shown in the inset of Figure 1). The sample was pretreated with an argon flow for 30 min (flow rate = 27 mL min^{-1}) to remove the air from the quartz cell. A flow of mixture of 10% of methane in argon (total flow rate = 30 mL min^{-1}) was introduced to the cell for 1 h in dark to achieve stable conditions, where the contact time

was nearly 0.8 s and space velocity (SV) was 4500 h^{-1}. The sample was then photoirradiated from a 300 W ceramic xenon lamp (PE300BUV) to start the photocatalytic NOCM. The irradiation area was 4 cm^2 and the light intensity measured by a UV radiometer (Topcon, UD 250 detector) in the wavelength range of 220–300 nm with the highest sensitivity at 254 nm was *ca.* 20 mW cm^{-2}. The reaction temperature was increased to be around 320 K by photoirradiation which was measured by an infrared thermometer (Testo, 835-T1). The outlet gases were analysed by two on-line gas chromatographs: one equipped with a TCD (Shimadzu, GC-8A, argon carrier, a Molecular Sieves 5A, column temperature 323 K) and another with an FID (Shimadzu, GC-8A, argon carrier, a Gaskuropack 54, column temperature 383 K).

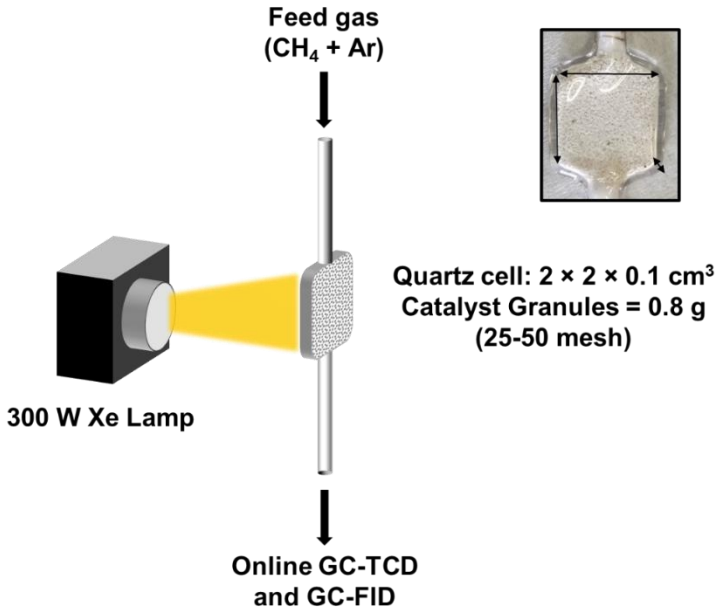

Figure 1 Experimental set-up used in the photocatalytic reaction tests of the NOCM, inset: the photograph of the sample cell filled with the granules of Pt(0.1)/Ga_2O_3. The size of the sample cell was 2 cm × 2 cm × 0.1 cm.

Methane conversion (%) is defined as the ratio of moles of methane consumed in the reaction to the total moles of methane introduced as shown in equation 3.

$$Methane\ conversion\ (\%) = \frac{Moles\ of\ methane\ consumed}{Moles\ of\ methane\ introduced} \times 100 \qquad (3)$$

The amount of consumed methane was estimated from the obtained gaseous products, ethane, and hydrogen according to equations 1 and 2.

2.3 Results and Discussion

2.3.1 Photocatalytic activity tests

The photocatalytic activity tests of the bare Ga_2O_3 sample and various cocatalyst loaded Ga_2O_3 samples were examined in a flow reactor. No products were detected in the dark without photoirradiation, without the photocatalyst and without methane introduction under the present reaction conditions. The results of the photocatalytic reaction tests of the NOCM with various samples are given in Table 1.

Table 1 Results of reaction tests of the NOCM over the bare Ga_2O_3 sample and various cocatalysts loaded Ga_2O_3 samples[a]

Entry	Sample[b]	Production rates[c] / μmol h^{-1}		R [d] (C_2H_6/H_2)
		C_2H_6	H_2	
1	Ga_2O_3	0.073	0.18	0.41
2 [e]	Pt/Ga_2O_3	0.023	1.6	0.014
3 [e]	Rh/Ga_2O_3	nd[f]	0.72	0
4	Pd/Ga_2O_3	0.51	1.2	0.42
5	Ag/Ga_2O_3	0.17	0.23	0.74
6	Ni/Ga_2O_3	nd[f]	0.10	0
7	Fe/Ga_2O_3	nd[f]	0.13	0
8	In/Ga_2O_3	0.045	0.20	0.23
9	Zn/Ga_2O_3	0.088	0.14	0.63
10	Sm/Ga_2O_3	0.049	0.16	0.31

[a]Reaction conditions were as follows. Photocatalyst in a quartz cell = 0.8 g, photoirradiation area = 4 cm^2, sample cell volume = 0.4 cm^3, feed gas = a mixture of 10% CH_4 in Ar with a total flow rate of 30 mL min^{-1}, contact time = 0.8 s, space velocity = 4500 h^{-1}, light intensity = 20 mW cm^{-2}, reaction temperature = *ca.* 320 K. [b]The loading amount of each element was 0.1 wt. %. [c]The production rates were measured after 5.5 h of the start of photoirradiation. [d]Calculated as follows. R (C_2H_6/H_2) = (production rate of ethane)/(production rate of hydrogen). [e]A very small amount of propane was also observed. [f]nd = not detected.

Only ethane, propane and hydrogen were observed as the products and other gases like ethene and propene were not observed. The values of propane production rates were often very low and under the detection limit of GC-FID, so only the values of production rates of ethane and hydrogen are reported here. The ratio of production rates of ethane and hydrogen, R, is

indicated as the index of the reaction selectivity with the ideal value of 1 for the NOCM taking place ideally. With a decrease in the *R* value, the selectivity for the NOCM also decreases caused by the side reactions such as the MD. Bare Ga_2O_3 sample exhibited production of both ethane and hydrogen but the value of *R* was lower than 1 (Table 1, entry 1). The time course of the NOCM over the bare Ga_2O_3 sample is shown in Figure 2. The production rates of ethane and hydrogen were 0.073 and 0.18 μmol h^{-1}, respectively with the value of *R* being 0.41 after 5.5 h of time on stream. The value of *R* lower than 1 might be due to the side reaction of the MD as discussed later because other products such as propane was not observed with the Ga_2O_3 sample. The average methane conversion was 0.002 % with the Ga_2O_3 sample which exceeded the thermodynamic limitation at the present reaction temperature (*ca.* 320 K).[2]

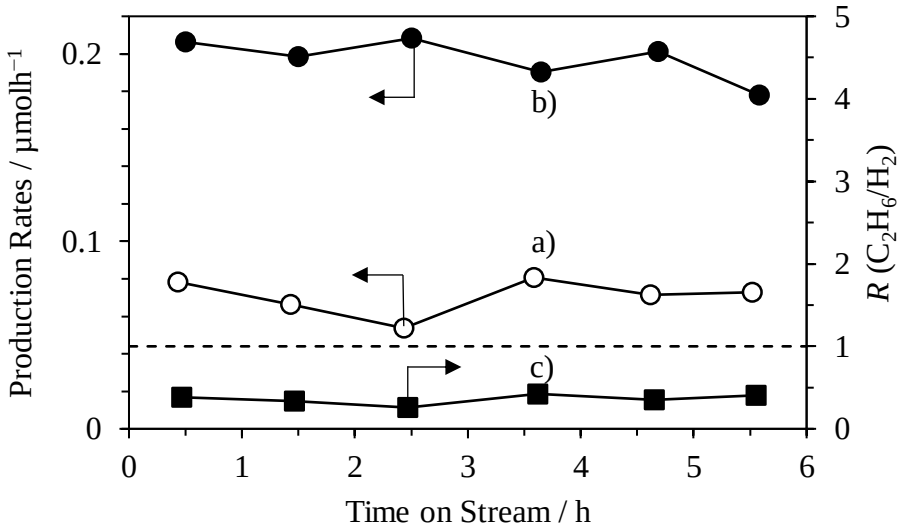

Figure 2 Production rates of (a) ethane, (b) hydrogen, and (c) the ratio of production rates of ethane and hydrogen, *R* over the bare Ga_2O_3 sample. The reaction conditions were same as those described in the footnote *a* of the Table 1.

Most cocatalyst loaded Ga_2O_3 samples exhibited very low and in some cases no production of ethane as shown in Table 1 meaning that the MD reaction took place as a competitive reaction even at 320 K in the present photocatalytic reaction conditions. Among them, only Ag, Zn and Pd loaded Ga_2O_3 samples showed better selectivity for the NOCM (Table 1, entries 5, 9 and 4, respectively) in comparison to the bare Ga_2O_3 sample indicating that only the Ag, Zn and Pd species can enhance the NOCM and not the MD. We focused on the Pd/Ga_2O_3 sample because it showed the highest production of desired product ethane.

Next, we optimized the loading amount of Pd and the results are given in Table 2. A Pd(0.5)/Ga_2O_3 sample exhibited the selective production of ethane and hydrogen from methane

upon photoirradiation with production rate of ethane and hydrogen of 0.22 and 0.23 μmol h^{-1}, respectively and the value of *R* was 0.96 after 5.5 h.

Table 2 The optimization of the loading amount of Pd in Pd(*x*)/Ga_2O_3 samples

Entry	Sample[a]	Production rates[b] / μmol h^{-1}		*R*[c] (C_2H_6/H_2)
		C_2H_6	H_2	
1	Ga_2O_3	0.073	0.18	0.41
2	Pd(0.01)/Ga_2O_3	0.20	0.88	0.23
3	Pd(0.05)/Ga_2O_3	0.35	0.85	0.41
4	Pd(0.1)/Ga_2O_3	0.51	1.2	0.42
5	Pd(0.2)/Ga_2O_3	0.43	1.2	0.36
6	Pd(0.25)/Ga_2O_3	0.41	1.01	0.41
7	Pd(0.5)/Ga_2O_3	0.22	0.23	0.96
8	Pd(0.6)/Ga_2O_3	0.13	0.23	0.56
9	Pd(1.0)/Ga_2O_3	0.036	0.17	0.21

[a]The loading amount of Pd was in wt. %. [b]The production rates were measured after 5.5 h of the start of the photoirradiation. [c]Calculated as follows. *R* (C_2H_6/H_2) = (production rate of ethane)/(production rate of hydrogen). The reaction conditions were same as those described in the footnote *a* of Table 1.

Figure 3A shows the times course of the NOCM with the Pt(0.1)/Ga_2O_3 sample. A very small amount of ethane was produced and the value of *R* was very low in the range of 0.01~0.03 during a time of stream of 5.5 h. This means that the MD reaction took place predominantly with the Pt/Ga_2O_3 sample. The hydrogen production rate decreased with time most probably due to the MD to form coke which deactivates the catalyst. However, we could not observe the possibly formed coke by thermogravimetry or by Raman spectroscopy possibly due to its low amount. On the contrary, selective production of ethane and hydrogen were obtained with the Pd(0.5)/Ga_2O_3 sample after an initial induction period (Figure 3B) with the value of *R* being 0.96 after 5.5 h meaning that the NOCM took place selectively over the Pd(0.5)/Ga_2O_3 sample. The production rate of ethane over the Pd(0.5)/Ga_2O_3 sample was more than three times higher in comparison to the bare Ga_2O_3 sample after 5.5 h of the photoirradiation. The methane conversion was calculated to be 0.008 – 0.006 % during the 5.5 h.

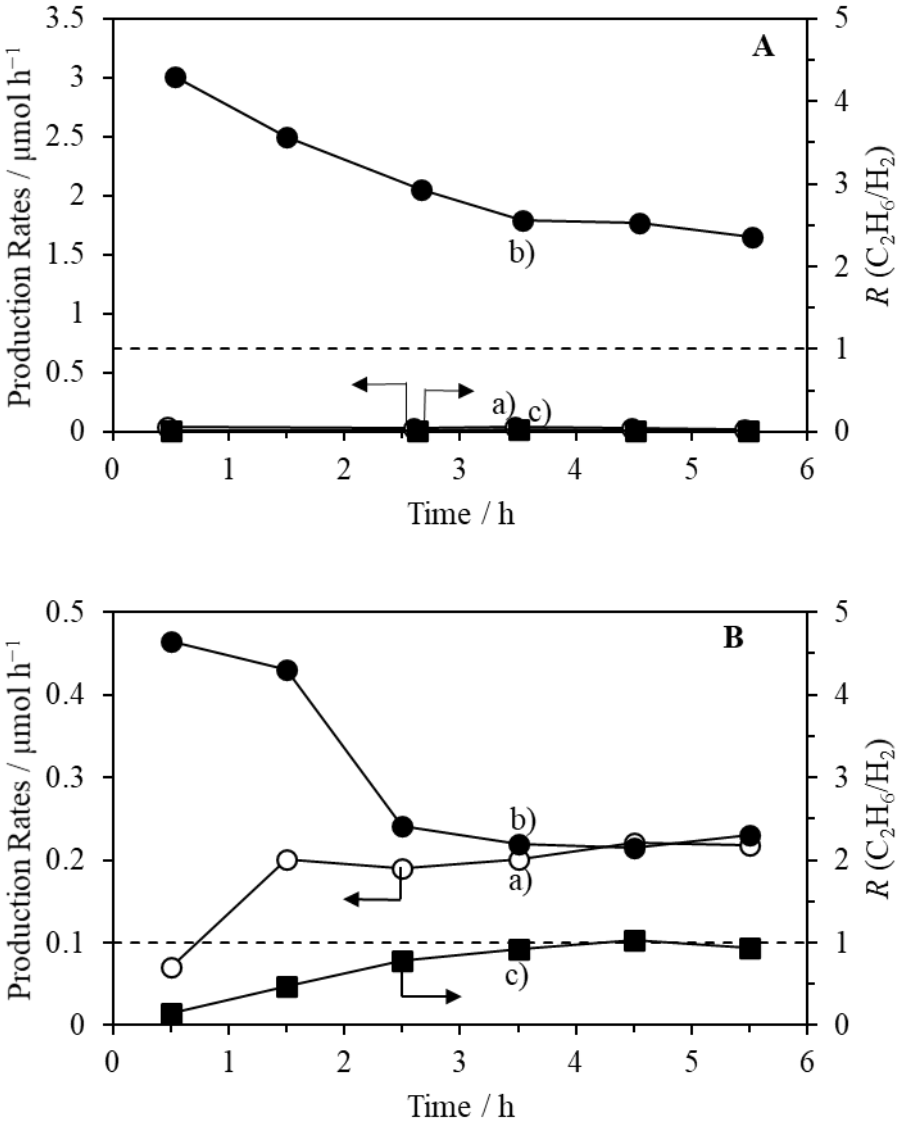

Figure 3 Time course of production rates of (a) ethane, (b) hydrogen, and (c) their ratio, *R* with (A) the Pt(0.1)/Ga_2O_3 sample, and (B) the Pd(0.5)/Ga_2O_3 sample. The reaction conditions were same as those described in the footnote *a* of Table 1.

2.3.2 Characterization

We used the commercial Ga_2O_3 sample for the reaction tests of the NOCM. This bare Ga_2O_3 and Pd-loaded Ga_2O_3 samples were characterized by some techniques. Figure 4 shows the XRD patterns of the samples. The XRD pattern of the bare Ga_2O_3 sample (Figure 4b) were nearly same as that of the β-Ga_2O_3 standard from a database (ICSD#34243)[20] (Figure 4a) except for some additional and some overlapping lines at 24.5, 33.8, 36.2, 41.5, 50.3, and 55.1°. These lines can be assigned to a α-Ga_2O_3 phase (ICSD#27431)[21] and the line at 36.2° is overlapping and assignable also to γ-Ga_2O_3 phase (ICSD#152085).[22] The XRD pattern analysis thus reveals that the used bare Ga_2O_3 sample is a mixed crystal consisting mainly of β-Ga_2O_3

phase including minor amounts of α- and γ-Ga_2O_3 phases. No new line appeared after the loading of the cocatalysts as shown in Figure 4c-e meaning that the cocatalysts particles are highly dispersed on the surface and do not form any new phase in Pd/Ga_2O_3 samples.

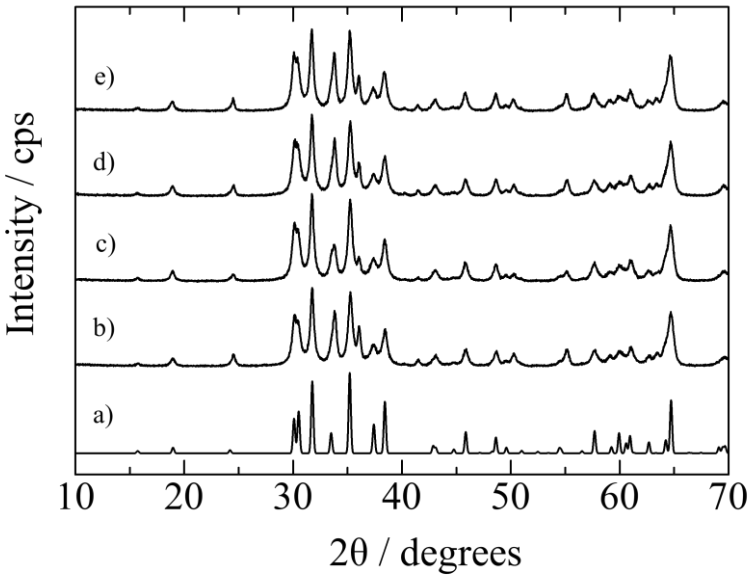

Figure 4 XRD Patterns of (a) β-Ga_2O_3 from a database (ICSD#34243), (b) bare Ga_2O_3 sample, and (c-e) the Pd(x)/Ga_2O_3 samples, where; x = 0.05, 0.1, 0.5, respectively.

The shape of the Ga_2O_3 particle was pillar-like with some cracks and the average length of the particles was 1 μm (Figure 5A) in the used Ga_2O_3 sample as previously reported in the literature.[23] After loading of Pd, some small particles could be observed in the Pd/Ga_2O_3 sample (Figure 5B), but we could not confirm whether or not these small particles derived from the cocatalysts because such particles were also observed in the bare Ga_2O_3 sample to a less extent. There was no significant effect of cocatalyst loading on the morphology and the average particle size of Ga_2O_3 particle.

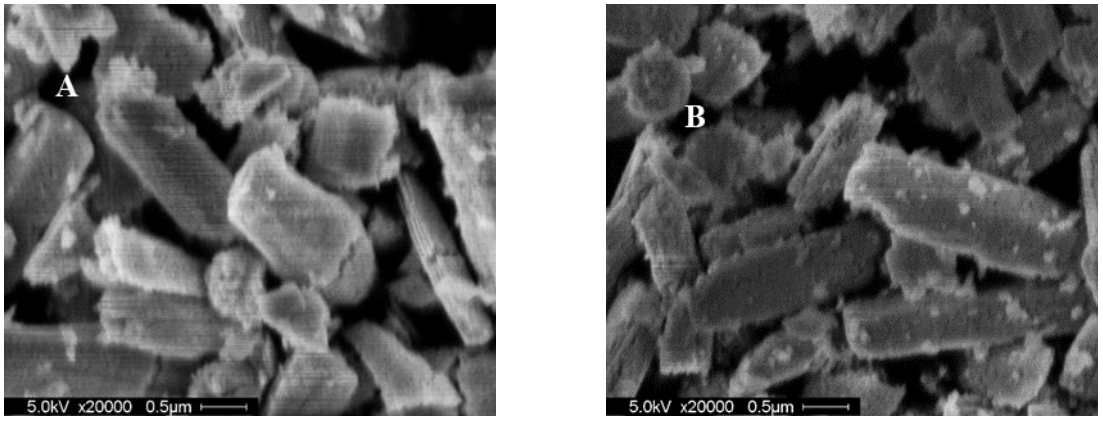

Figure 5 SEM images of (A) the bare Ga_2O_3 sample, and (B) the Pd(0.5)/Ga_2O_3 sample.

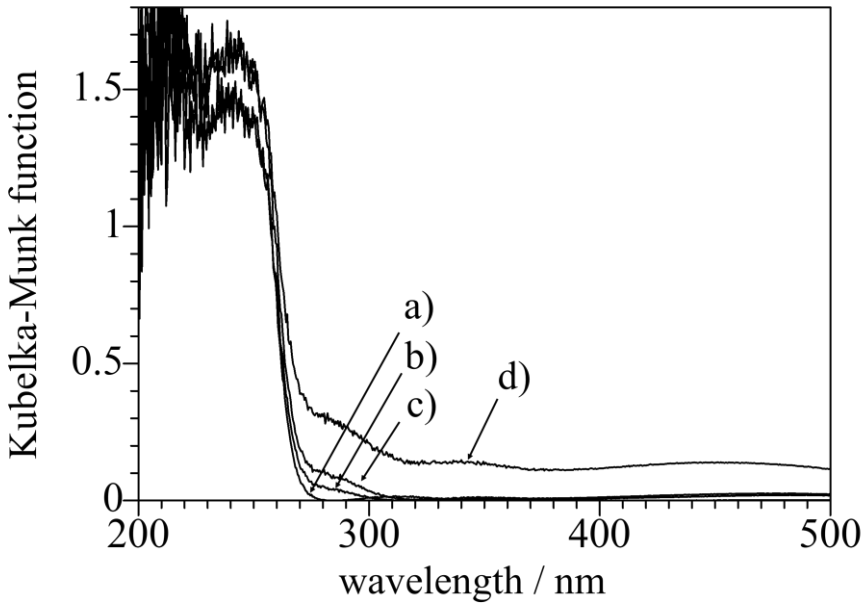

Figure 6 DR UV-vis spectra of the samples, (a) bare Ga_2O_3, (b) Pd(0.05)/Ga_2O_3, (c) Pd(0.1)/Ga_2O_3, and (d) Pd(0.5)/Ga_2O_3.

The photoabsorption properties of the samples were investigated by the DR UV-vis spectroscopy and results are shown in Figure 6. Bare Ga_2O_3 exhibited the strong absorption below the wavelengths of 280 nm (Figure 6a) and the band gap was calculated to be *ca.* 4.6 eV in agreement with the literature. After loading of the Pd cocatalyst, the absorption in the wavelength range of 270-500 nm was also appeared and the intensity of this absorption increased with an increase in the loading amount of Pd cocatalysts (Figure 6b-d) probably due to the PdO species.[24] This indicates that the loading of cocatalyst by the impregnation method followed by the calcination at 673 K provides PdO species without changing the band gap of Ga_2O_3 drastically.[25]

The BET specific surface area of the bare Ga_2O_3 sample was 22.8 m^2g^{-1}.

2.3.3 Reaction Conditions

2.3.3.1 Effect of temperature in the dark

We increased the reaction temperature in the dark and tested whether or not thermal energy provided at high temperature can drive the NOCM with the Pd/Ga_2O_3 sample. No products were observed at 323 and 573 K in the dark (Table 3, entries 1-2). When the temperature was increased to 623 K, only hydrogen and no ethane were observed meaning that the MD took place at 623 K (Table 3, entry 3). The color of the sample became dark grey after the reaction at 623 K as shown in Figure 7 indicating the formation of coke as a result of the

MD reaction. Thus, thermal energy provided at high temperature could not drive NOCM and the MD took place instead.

Table 3 The effect of thermal energy in the dark with the Pd/Ga_2O_3 sample[a]

Entry	Temperature (K)	Production rates[b] / μmol h^{-1}	
		C_2H_6	H_2
1	323	nd[c]	nd[c]
2	573	nd[c]	nd[c]
3	623	nd[c]	0.36

[a]The Pd/Ga_2O_3 sample was prepared by the impregnation method and the loading amount was 0.5 wt. %. The reaction conditions were same as those described in the footnote *a* of Table 1. [b]The production rates were measured after 1.5 h. [c]nd = not detected.

Figure 7 Photograph of the sample cell after the reaction at 623 K with the $Pd(0.5)/Ga_2O_3$ sample

2.3.3.2 Effect of light intensity

The intensity of the incident light was varied from 20 to 230 $mWcm^{-2}$ and its effect on the photocatalytic activities of the Pd/Ga_2O_3 sample for the NOCM was studied. Results are shown in Figure 8. When the intensity was increased from 20 to 40 mW cm^{-2}, the production rates of ethane also increased from 0.35 to 0.42 μmol h^{-1}. When the intensity was further increased, the ethane production rates decreased. Application of very high light intensities such as 145 and 230 mW cm^{-2} showed the production of very large hydrogen production and very small ethane production suggesting that the MD took place predominantly at these higher intensities.

The color of the sample also changed to dark grey after the reaction at 145 and 230 mW cm^{-2} as shown in Figure 9 supporting the occurrence of the MD at these intensities. These results indicate that the moderate light intensity is favorable for the selective NOCM.

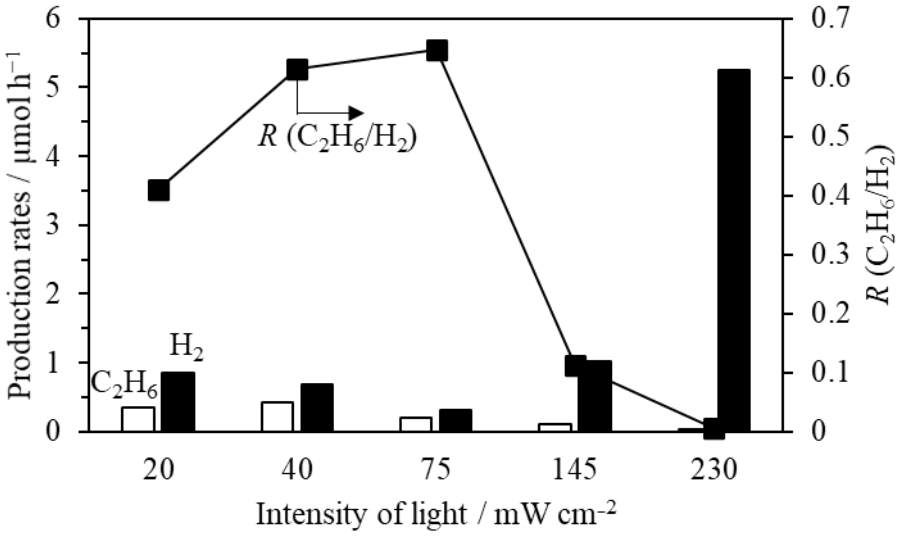

Figure 8 Production rates of ethane (white bars), hydrogen (black bars), and the ratio of these production rates, *R* (black line with markers) in the photocatalytic reaction tests of the NOCM with the Pd(0.05)/Ga_2O_3 sample under different intensities of the incident light. The production rates were measured after 5 h. Other reaction conditions were same as those described in the footnote *a* of Table 1.

Figure 9 Photographs of the sample cell after the reaction with the Pd(0.05)/Ga_2O_3 sample under the light intensity of (a) 40, (b) 145, and (c) 230 mW cm^{-2}. The other reaction conditions were same as those described in the footnote *a* of Table 1.

When the gallium oxide is photo-irradiated, the electron and holes are generated at its conduction band (CB) and valence band (VB), respectively. Methane molecules can react with photogenerated holes to produce methyl radicals and protons (eq 4). Methyl radicals can couple to form ethane (eq. 5) while protons should be reduced by the photogenerated electrons to form hydrogen at the Pd sites (eq 6).

$$CH_4 + h^+ \rightarrow \bullet CH_3 + H^+ \qquad (4)$$

$$2 \bullet CH_3 \rightarrow C_2H_6 \qquad (5)$$

$$2 H^+ + 2 e^- \rightarrow H_2 \qquad (6)$$

The higher light intensity increases the hole oxidation rates which would promote the methyl radical formation and also the deep dehydrogenation of the methyl radicals on the surface before them getting desorbed which is a proposed mechanism for the methane decomposition on the surface according to eq 7.

$$\bullet CH_3 + 3\ h^+ \rightarrow C + 3\ H^+ \qquad (7)$$

The time course of the reaction at the light intensity of 145 mW cm^{-2} with the Pd/Ga_2O_3 sample is shown Figure 10. The value of *R* decreases with time meaning that the selectivity for the NOCM decreases with the time and the MD takes place instead. The higher light intensity increases the rate of both NOCM and the MD, but the formation of coke as a result of the MD would change the surface property of the Pd/Ga_2O_3 sample which would in turn decrease the activity for the NOCM with time. It is also possible that photoenergy and thermal energy synergistically enhance the MD at higher intensities since the temperature measured at the light intensity of 230 $mWcm^{-2}$ was *ca.* 433 K.

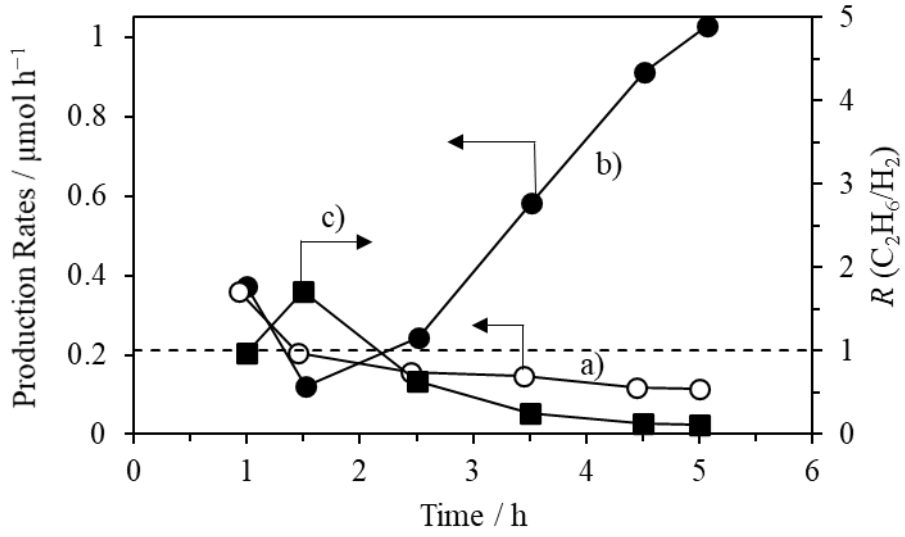

Figure 10 Production rates of (a) ethane, (b) hydrogen, and (c) their ratio, *R* at the light intensity of 145 $mWcm^{-2}$ with the $Pd(0.05)/Ga_2O_3$ sample. The other reaction conditions were same as those described in the footnote *a* of Table 1.

2.3.3.3 Effect of concentration of methane in the feed gas

We used a mixture of methane and the Ar gas as the feed gas in the present study. We varied the concentration of methane in the feed gas with the Pd/Ga_2O_3 sample and examined its effect on the production rates. The results are shown in Figure 11. When the methane concentration in the feed gas was increased from 10% to 80%, the ethne production rates also increased which is expected kinetically. However, the value of *R* decreased at the methane of

80% in the feed gas and with 100% of methane as the feed gas meaning that the rate of the MD became higher at these concentrations. Higher concentration of methane would enhance both the NOCM and the MD, and the latter reaction would produce coke on the surface to change the reaction selectivity as discussed above.

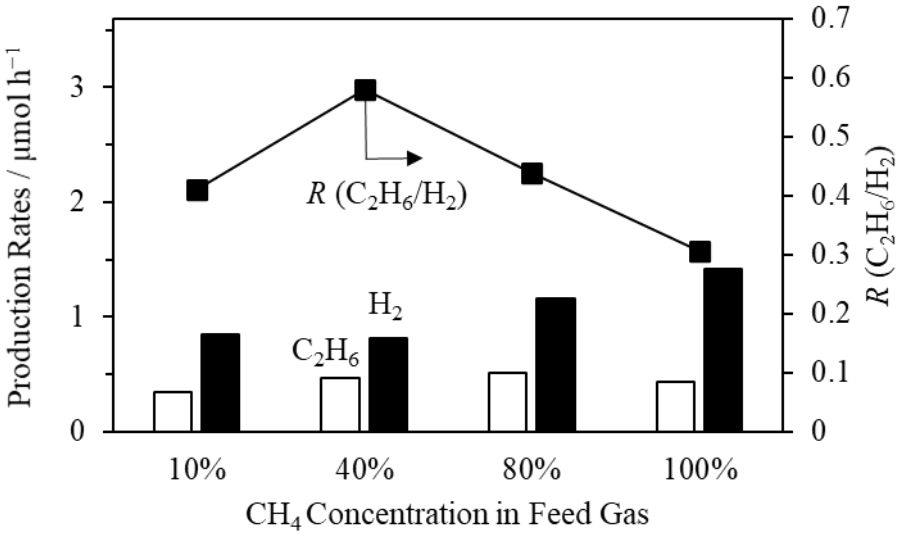

Figure 11 Production rates of ethane (white bars), hydrogen (black bars), and their ratio, *R* (black line with markers) with various methane concentration in the feed gas with the Pd(0.05)/Ga_2O_3 sample. The production rates were measured after 5 h. The other reaction conditions were same as those described in the footnote *a* of Table 1.

2.3.3.4 Effect of the flow rate of the feed gas

The flow rate of the feed gas of the mixture of methane and Ar was changed and its effect on the production rates was examined. The results are shown in Figure 12. With an increase in the total flow rate of the feed gas, the production rates of ethane and the value of *R* increased. This can be explained based on the faster migration of methyl radicals formed by photogenerated holes before their further dehydrogenation to coke at higher flow rate of the feed gas resulting in lower probability of the MD and the increase in the value of *R*. At very low flow rate of feed gas of 10 mL min^{-1}, a small amount of propane was also formed suggesting that the longer contact time at the low flow rate would also facilitate the successive coupling reactions of ethane to produce higher hydrocarbons such as propane.

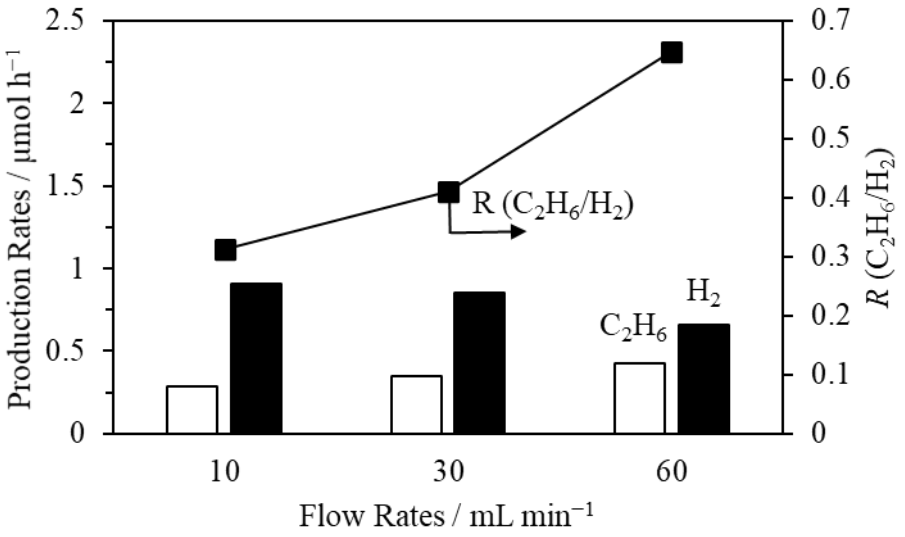

Figure 12 The production rates of ethane (white bars), hydrogen (black bars), and their ratio, *R* (black line with markers) at different flow rates of the feed gas with the Pd(0.05)/Ga_2O_3 sample. The production rates were measured after 5 h. Other reaction conditions were same as those described in the footnote *a* of Table 1.

2.4 Conclusions

It was evidenced that the NOCM can be promoted with the Ga_2O_3 photocatalyst using a flow reactor. Loading of the Pd cocatalyst improved the activity of the Ga_2O_3 photocatalyst further and a Pd(0.5)/Ga_2O_3 sample exhibited selective NOCM with the production rates of ethane and hydrogen of 0.22 and 0.23 μmol h^{-1}, respectively and the value of *R* being 0.96 after 5.5 h of photoirradiation at nearly room temperature (*ca.* 320 K) and atmospheric pressure where the contact time and the space velocity were 0.8 s and 4500 h^{-1}, respectively. The methane conversion was calculated to be 0.006% with the Pd(0.5)/Ga_2O_3 sample clearly exceeding the thermodynamic equilibrium conversion value at the reaction temperature (*ca.* 320 K).

The suitable reaction conditions were investigated and it was found that a moderate light intensity, a moderate concentration of the methane in the feed gas, and a high flow rate of the feed gas are favorable for the selective NOCM. It was also revealed that the MD took place with some cocatalyst loaded Ga_2O_3 samples such as Rh- and Pt-loaded Ga_2O_3 samples to form coke which deactivates the catalyst. The MD also took place with the Pd/Ga_2O_3 sample at high light intensity and high concentration of methane in the feed gas which is a remaining problem to be studied and solved further.

Acknowledgement

This work was financially supported by a Grant-in-Aid for Scientific Research (B), (No. 25289285), and a Grant-in-Aid for Scientific Research on Innovative Areas (No. 25105723) from JSPS, and the Program for Element Strategy Initiative for Catalysts & Batteries (ESICB, JPMXP0112101003), commissioned by the MEXT of Japan. S. P. Singh would like to thank JICA for providing the scholarship under FRIENDSHIP project to pursue his Ph.D. in Japan.

References

(1) Choudhary, T. V.; Aksoylu, E.; Goodman, D. W. Nonoxidative Activation of Methane. *Catal. Rev. - Sci. Eng.* **2003**, *45* (1), 151–203.

(2) Yuliati, L.; Yoshida, H. Photocatalytic Conversion of Methane. *Chem. Soc. Rev.* **2008**, *37* (8), 1592–1602.

(3) Yuliati, L.; Hattori, T.; Itoh, H.; Yoshida, H. Photocatalytic Nonoxidative Coupling of Methane on Gallium Oxide and Silica-Supported Gallium Oxide. *J. Catal.* **2008**, *257* (2), 396–402.

(4) Yuliati, L.; Itoh, H.; Yoshida, H. Photocatalytic Conversion of Methane and Carbon Dioxide over Gallium Oxide. *Chem. Phys. Lett.* **2008**, *452* (1–3), 178–182.

(5) Yanagida, T.; Sakata, Y.; Imamura, H. Photocatalytic Decomposition of H_2O into H_2 and O_2 over Ga_2O_3 Loaded with NiO. *Chem. Lett.* **2004**, *33* (6), 726–727.

(6) Sakata, Y.; Matsuda, Y.; Nakagawa, T.; Yasunaga, R.; Imamura, H.; Teramura, K. Remarkable Improvement of the Photocatalytic Activity of Ga_2O_3 towards the Overall Splitting of H_2O. *ChemSusChem* **2011**, *4* (2), 181–184.

(7) Sakata, Y.; Nakagawa, T.; Nagamatsu, Y.; Matsuda, Y.; Yasunaga, R.; Nakao, E.; Imamura, H. Photocatalytic Properties of Gallium Oxides Prepared by Precipitation Methods toward the Overall Splitting of H_2O. *J. Catal.* **2014**, *310*, 45–50.

(8) Hou, Y.; Wang, X.; Wu, L.; Ding, Z.; Fu, X. Efficient Decomposition of Benzene over a β-Ga_2O_3 Photocatalyst under Ambient Conditions. *Environ. Sci. Technol.* **2006**, *40* (18), 5799–5803.

(9) Shao, T.; Zhang, P.; Jin, L.; Li, Z. Photocatalytic Decomposition of Perfluorooctanoic Acid in Pure Water and Sewage Water by Nanostructured Gallium Oxide. *Appl. Catal. B Environ.* **2013**, *142–143*, 654–661.

(10) Teramura, K.; Tsuneoka, H.; Shishido, T.; Tanaka, T. Effect of H_2 Gas as a Reductant on Photoreduction of CO_2 over a Ga_2O_3 Photocatalyst. *Chem. Phys. Lett.* **2008**, *467* (1–

3), 191–194.

(11) Teramura, K.; Wang, Z.; Hosokawa, S.; Sakata, Y.; Tanaka, T. A Doping Technique That Suppresses Undesirable H2 Evolution Derived from Overall Water Splitting in the Highly Selective Photocatalytic Conversion of CO_2 in and by Water. *Chem. - A Eur. J.* **2014**, *20* (32), 9906–9909.

(12) Yamamoto, M.; Yoshida, T.; Yamamoto, N.; Nomoto, T.; Yamamoto, Y.; Yagi, S.; Yoshida, H. Photocatalytic Reduction of CO_2 with Water Promoted by Ag Clusters in Ag/Ga_2O_3 Photocatalysts. *J. Mater. Chem. A* **2015**, *3* (32), 16810–16816.

(13) Pan, Y. X.; Sun, Z. Q.; Cong, H. P.; Men, Y. L.; Xin, S.; Song, J.; Yu, S. H. Photocatalytic CO_2 Reduction Highly Enhanced by Oxygen Vacancies on Pt-Nanoparticle-Dispersed Gallium Oxide. *Nano Res.* **2016**, *9* (6), 1689–1700.

(14) Wang, Z.; Teramura, K.; Huang, Z.; Hosokawa, S.; Sakata, Y.; Tanaka, T. Tuning the Selectivity toward CO Evolution in the Photocatalytic Conversion of CO_2 with H_2O through the Modification of Ag-Loaded Ga_2O_3 with a $ZnGa_2O_4$ Layer. *Catal. Sci. Technol.* **2016**, *6* (4), 1025–1032.

(15) Kawaguchi, Y.; Akatsuka, M.; Yamamoto, M.; Yoshioka, K.; Ozawa, A.; Kato, Y.; Yoshida, T. Preparation of Gallium Oxide Photocatalysts and Their Silver Loading Effects on the Carbon Dioxide Reduction with Water. *J. Photochem. Photobiol. A Chem.* **2018**, *358*, 459–464.

(16) Yoshida, H.; Kato, S.; Hirao, K.; Nishimoto, J.-I.; Hattori, T. Photocatalytic Steam Reforming of Methane over Platinum-Loaded Semiconductors for Hydrogen Production. *Chem. Lett.* **2007**, *36* (3), 430–431.

(17) Yoshida, H.; Hirao, K.; Nishimoto, J.-I.; Shimura, K.; Kato, S.; Itoh, H.; Hattori, T. Hydrogen Production from Methane and Water on Platinum Loaded Titanium Oxide Photocatalysts. *J. Phys. Chem. C* **2008**, *112* (14), 5542–5551.

(18) Shimura, K.; Kato, S.; Yoshida, T.; Itoh, H.; Hattori, T.; Yoshida, H. Photocatalytic Steam Reforming of Methane over Sodium Tantalate. *J. Phys. Chem. C* **2010**, *114* (8), 3493–3503.

(19) Yamamoto, A.; Mizuba, S.; Saeki, Y.; Yoshida, H. Platinum Loaded Sodium Tantalate Photocatalysts Prepared by a Flux Method for Photocatalytic Steam Reforming of Methane. *Appl. Catal. A Gen.* **2016**, *521*, 125–132.

(20) Geller, S. Crystal Structure of β-Ga_2O_3 Cite. *J. Chem. Phys* **1960**, *33* (4), 676.

(21) Marezuo, M.; Remeika, J. P. Bond Lengths in the α-Ga_2O_3 Structure and the High-Pressure Phase Of. *J. Chem. Phys.* **1967**, *46* (5), 1862–1865.

(22) Zinkevich, M.; Morales, F. M.; Nitsche, H.; Ahrens, M.; Rühle, M.; Aldinger, F. Microstructural and Thermodynamic Study of γ-Ga_2O_3. *Zeitschrift fuer Met.* **2004**, *95* (9), 756–762.

(23) Iguchi, S.; Hasegawa, Y.; Teramura, K.; Kidera, S.; Kikkawa, S.; Hosokawa, S.; Asakura, H.; Tanaka, T. Drastic Improvement in the Photocatalytic Activity of Ga_2O_3 Modified with Mg-Al Layered Double Hydroxide for the Conversion of CO_2 in Water. *Sustain. Energy Fuels* **2017**, *1* (8), 1740–1747.

(24) Barrera, A.; Tzompantzi, F.; Padilla, J. M.; Casillas, J. E.; Jácome-Acatitla, G.; Cano, M. E.; Gómez, R. Reusable PdO/Al_2O_3-Nd_2O_3 Photocatalysts in the UV Photodegradation of Phenol. *Appl. Catal. B Environ.* **2014**, *144*, 362–368.

(25) Shimura, K.; Yoshida, T.; Yoshida, H. Photocatalytic Activation of Water and Methane over Modified Gallium Oxide for Hydrogen Production. *J. Phys. Chem. C* **2010**, *114* (26), 11466–11474.

3 A Pd-Bi dual-cocatalyst-loaded gallium oxide photocatalyst for selective and stable nonoxidative coupling of methane

Abstract

Non-oxidative coupling of methane (NOCM) is an attractive reaction for the conversion of methane to ethane and hydrogen directly. Although conventional catalytic NOCM reaction needs high operating temperatures and thus suffers from the deactivation of the catalyst by coke formation, photocatalytic NOCM reaction can take place at low temperature even around room temperature. In the present study, a gallium oxide photocatalyst with a palladium and bismuth dual cocatalyst (Pd-Bi/Ga_2O_3) was found to exhibit high activity for selective NOCM producing ethane and hydrogen from methane upon photoirradiation at nearly room temperature (*ca.* 320 K) and atmospheric pressure. The optimized Pd(0.18)-Bi(0.05)/Ga_2O_3 photocatalyst showed high production rate of ethane such as 1.10 μmol h^{-1}, where the methane conversion was 0.03% within the contact time of 0.8 s, the reaction selectivity was as high as 97%, and the apparent quantum efficiency was 0.2%. The methane conversion exceeded the thermodynamic limitation. The Pd-Bi/Ga_2O_3 photocatalyst showed excellent stability for 100 h without significant loss of activity and selectivity. The recyclability was also confirmed. The roles of the dual cocatalyst involving the interparticle transfer and a tentative reaction mechanism with the dual cocatalyst were also proposed.

3.1 Introduction

Among various methane conversion routes, non-oxidative coupling of methane (NOCM) is not easy but an attractive and promising reaction since methane can be used as a carbon source and converted directly to ethane and hydrogen (eq. 1) through the C–H bond activation without the aid of any oxidant[1] and both the products are quite useful, i.e., ethane is a starting material to various useful chemicals such as ethylene while hydrogen can be used not only for the hydrogenation and reduction in chemical industry but also as a clean fuel in fuel cells.

$$2\ CH_4 \rightarrow C_2H_6 + H_2, \qquad \Delta_r G^{\Theta}_{298K} = 68.6\ kJ\ mol^{-1} \qquad (1)$$

This is, however, an endergonic uphill reaction and is not thermodynamically feasible owing to practically very low value of thermodynamic equilibrium constant and equilibrium conversion such as 9.5×10^{-13} and 0.0002 %, respectively at 298 K.[2] Although the use of a catalyst reduces the activation energy of this reaction significantly, application of higher temperature leads to deactivation of the catalyst by coke deposition at its surface because the methane decomposition (MD) to carbon and hydrogen (eq. 2) is thermodynamically more favorable than the NOCM at temperatures higher than 800 K.[2]

$$CH_4 \rightarrow C + 2H_2, \qquad \Delta_r G^{\Theta}_{298K} = 50.7\ kJ\ mol^{-1} \qquad (2)$$

Photocatalysis has emerged as a green technology during recent decades because it can promote the thermodynamically unfavorable reactions even around room temperature using the photoenergy to compensate for the increase in the chemical potential of the products. In our previous study, we described the NOCM over the Pd-loaded Ga_2O_3 sample in a flow reactor.[3] But over many samples like Pt/Ga_2O_3 and Rh/Ga_2O_3, the MD took place predominantly instead of the desired NOCM even at the low temperature such as 320 K. Thus, some feats are yet to be achieved such as the high selectivity for the NOCM with the high production rates of ethane and hydrogen from methane upon photoirradiation and the long-term stability of the photocatalyst under the non-oxidative (or reductive) reaction conditions of the NOCM, i.e.; the presence of methane, ethane and the hydrogen upon photoirradiation and under the influence of coke formation as a result of the side reaction of the MD. In the present study, we examined loading various dual cocatalyst on the bare Ga_2O_3 sample and to test their activity in the photocatalytic reaction tests of the NOCM. As a result, it was found that a palladium bismuth dual cocatalyst loaded gallium oxide (Pd-Bi/Ga_2O_3) sample exhibited selective

production of ethane and hydrogen and the optimized Pd(0.18)-Bi(0.05)/Ga_2O_3 photocatalyst showed ethane production rate of 1.10 μmol h^{-1}, which was more than 3 times and 21 times higher than the single-Pd-loaded Ga_2O_3 sample and the bare Ga_2O_3 sample.

3.2 Experimental Section

3.2.1 Materials and Methods

The employed Ga_2O_3 sample was obtained commercially (Ga_2O_3, 99.90%, 14.4 m^2g^{-1}, Kojundo Chemicals, Product No. GA004PB) and was used as received without further purification, which is different sample from that used in the previous study (99.90%, 22.8 m^2g^{-1}, Kojundo Chemicals, Product No. GA001PB). This sample was of mixed crystal consisting mainly of β-Ga_2O_3 phase including minor amount of α-Ga_2O_3 and γ-Ga_2O_3 phases as discussed later in the XRD pattern analysis. For comparison, several samples were employed; anatase TiO_2 (ST-01, anatase, 300 m^2 g^{-1}, Ishihara Sangyo Kaisha Ltd.), a mixture of anatase and rutile TiO_2 (P-25, 49 m^2 g^{-1}, Nippon Aerosil Co. Ltd.), CeO_2 (99.99 %, Kojundo Chemicals), ZnO (99.99 %, Kojundo Chemicals), SiO_2 (CARiACT Q-3, Fuji Silysia Chemical Ltd.), Al_2O_3 (JRC-ALO-7, γ-phase, 170 m^2 g^{-1}, the Catalysis Society of Japan) and Bi_2O_3 (98.0 %, Wako Pure Chemicals), which were also commercially obtained or donated from the Catalysis Society of Japan and were used as received without further purification. Quartz sand (Wako Pure Chemicals) used in the photocatalyst dilution experiments was also commercially obtained.

The following chemicals were used as precursors of additives, a Pd standard solution (5 mg mL^{-1} $Pd(NO_3)_2$ in 6.6 mol L^{-1} HNO_3 aq., Wako Chemicals), $RhCl_3$ (98%, Wako Chemicals), $Pt(NH_3)_4(NO_3)_2$ (99.0%, Nacalai Tesque), $Sm(NO_3)_3 \cdot 6H_2O$ (99.5%, Wako Chemicals), $(NH_4)_2IrCl_6$ (99%, Wako Chemicals), $Ni(NO_3)_2 \cdot 6H_2O$ (99.9%, Wako Chemicals), $Co(NO_3)_2 \cdot 6H_2O$ (97.0%, Nacalai Tesque), CsCl (99.0%, Nacalai Tesque), $Zn(NO_3)_3 \cdot 6H_2O$ (99.0%, Nacalai Tesque), $(NH_4)_2HPO_4$ (99.0%, Nacalai Tesque), $Fe(NO_3)_3 \cdot 9H_2O$ (99.0%, Nacalai Tesque), $HAuCl_4 \cdot 4H_2O$ (99.0%, Nacalai Tesque), $SbCl_3$ (99.9%, Wako Chemicals), $Pb(NO_3)_2$ (99.5%, Kishida Chemicals), $Mn(NO_3)_2 \cdot 6H_2O$ (98.0%, Nacalai Tesque), a Bi standard solution (1 g L^{-1} $Bi(NO_3)_3$ in 0.5 mol L^{-1} HNO_3 aq., Wako Chemicals), $Cu(NO_3)_2 \cdot 3H_2O$ (77–80%, Kanto Chemicals), $AgNO_3$ (99.8%, Kishida Chemicals), and $SnCl_4 \cdot 5H_2O$ (98.0%, Wako Chemicals).

The dual cocatalyst-loaded photocatalyst samples were prepared by a co-impregnation method. The procedure is as follows: The photocatalyst powder sample such as Ga_2O_3 (1.4 g) was stirred in an aqueous solution (total volume: 100 mL) of the precursors of the two cocatalysts at room temperature for 30 min, followed by heating at 353 K to evaporate water to dryness. The obtained powder was dried at 373 K overnight and calcined in an alumina crucible by using an electric muffle furnace at 773 K for 3 h. These samples were referred to as $M_1(x)$-$M_2(y)$/photocatalyst, where x and y show loading amount of the additive elements M_1 and M_2 in mol %, respectively, for example, Pd(0.18)-Bi(0.05)/Ga_2O_3.

As single cocatalyst-loaded photocatalysts, the Pd loaded and Bi loaded gallium oxide samples were prepared by an impregnation method. The procedure was the same as that of the co-impregnation method except that only one precursor was used to prepare the sample. The single metal- or metal oxide-loaded samples were referred to as M(x)/photocatalyst, where x in mol % gives loading amount of the additive element M, for example, Bi(0.18)/Ga_2O_3.

Another sample, Au(0.41)/TiO_2, corresponding to 1 wt. % of Au, was prepared using the mixed phase TiO_2 (P-25) by a photodeposition method as described in the literature.[4]

3.2.2 Characterization

The obtained samples were characterized by several techniques. The crystal structure was determined by powder X-ray diffraction (XRD) with a Shimadzu LabX XRD-6000 X-ray diffractometer using Cu Kα radiation (40 kV, 30 mA). The BET specific surface area (SSA) was measured by N_2 adsorption at 77 K with a Quantachrome Monosorb rapid surface area analyzer. Scanning electron microscope (SEM) images were recorded on a JEOL model JSM-890 scanning microscope. Transmission electron microscope (TEM) images and scanning transmission electron microscope (STEM) images with energy dispersive X-ray (EDX) analysis were recorded by a JEOL JEM-2100F field emission electron microscope at 200 kV in Joint Research Center at Kindai University. Diffuse reflectance UV-visible (DR UV-vis) spectra were recorded by a JASCO V-570 UV/VIS/NIR spectrophotometer equipped with an integrating sphere covered with a $BaSO_4$ reference. Pd K-edge X-ray absorption fine structure (XAFS) of the samples were measured in a fluorescence mode using a 19-

element Ge solid state detector (SSD) at the BL01B1 beamline of synchrotron radiation facility SPring-8, Japan.

3.2.3 Experimental Set-up

The photocatalytic activity test for the NOCM was carried out using a flow reactor shown in Figure 1.[3,5–8]

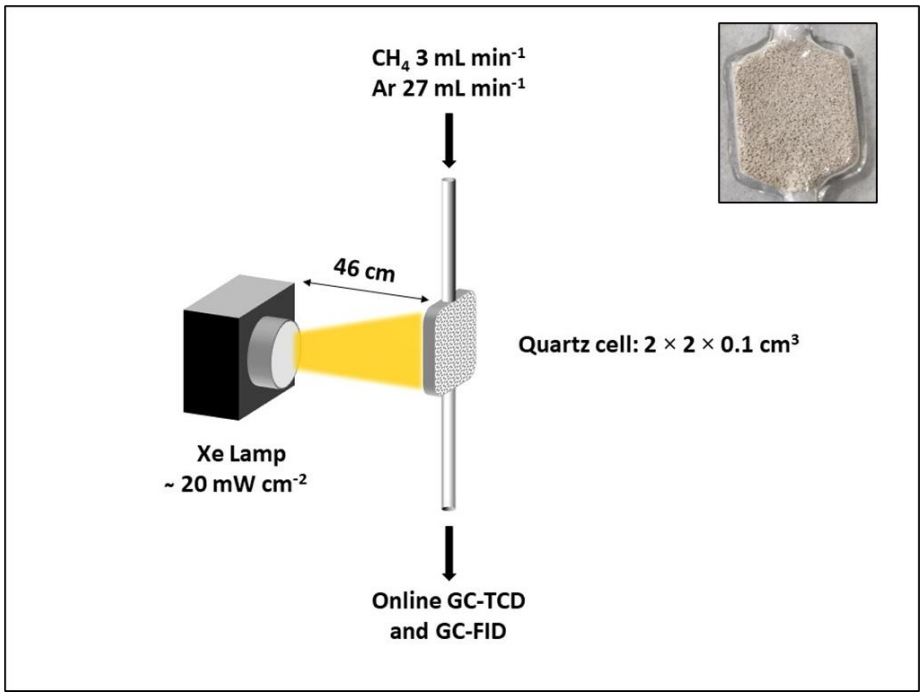

Figure 1 The schematic diagram of the experimental set-up used in the reaction test of the NOCM. Inset: the photograph of the sample cell filled with the granules of the Pd(0.18)-Bi(0.05)/Ga_2O_3 sample. The size of the sample cell was 2 cm × 2 cm × 0.1 cm. The horizontal distance between the lamp and the sample cell was nearly 46 cm.

The catalyst powder was pressed under 40 MPa pressure and ground into granules of 310–710 μm (25–50 mesh). The sample granules were filled into a quartz cell (2 × 2 × 0.1 cm^3, see the photograph in the inset of Figure 1). The weight of the granules used for filling the cell was 0.8, 0.6, 1.5, 1.0, 0.4, and 0.4 g for the bare and dual cocatalyst loaded Ga_2O_3, TiO_2, CeO_2, ZnO, SiO_2, or Al_2O_3 samples, respectively. The sample was pretreated with an argon flow for 30 min (flow rate 27 mL min^{-1}) to exclude the air from the quartz cell. A flow of mixture of 10% methane in argon (total flow rate 30 mL min^{-1}) was introduced to the cell for 1 h in dark to achieve stable conditions, where the contact time was nearly 0.8 s and space velocity (SV) was 4500 h^{-1}. The sample was then photoirradiated from a ceramic xenon lamp (PE300BUV, 300

W) to start the photocatalytic NOCM. The irradiation area was 4 cm^2 and the light intensity measured by a UV radiometer (Topcon, UD 250 detector) in the wavelength range of 220–300 nm with the highest sensitivity at 254 nm was *ca.* 20 mW cm^{-2}. The reaction temperature was increased to *ca.* 320 K by photoirradiation which was measured by an infrared thermometer (Testo, 835-T1). The outlet gases were analyzed by two on-line gas chromatographs: one equipped with a TCD (Shimadzu, GC-8A, argon carrier, a Molecular Sieves 5A, column temperature 323 K) and another with an FID (Shimadzu, GC-8A, argon carrier, a Gaskuropack 54, column temperature 383 K). The detectable gases by the GC-TCD were hydrogen, oxygen, nitrogen, methane, and carbon monoxide while the detectable gases by the GC-FID were methane, ethene, ethane, propene, and propane in the detection range of retention times.

3.2.4 Calculations of methane conversion and the apparent quantum yield (AQE)

The methane conversion (%) was defined as the ratio of moles of methane consumed in the reaction to the total moles of methane introduced as shown in eq. 3. The amount of consumed methane was estimated from the obtained gaseous products, ethane, and hydrogen.

$$Methane\ conversion\ (\%) = \frac{Moles\ of\ methane\ consumed}{Moles\ of\ methane\ introduced} \times 100 \quad (3)$$

The apparent quantum efficiency (AQE) was calculated as the ratio of the number of consumed electrons for photocatalytic product formation to the number of incident photons in the range of 220–300 nm as shown in eq. 4.[9]

$$AQE\ (\%) = \frac{r \times n \times N}{(I \times A)/(hc/\lambda)} \times 100 \quad (4)$$

where r = production rate of H_2 (in mol s^{-1}), n = number of electrons consumed for the production of H_2 (n=2), N = Avogadro constant (in mol^{-1}), I = Intensity of the incident light measured by a UV photometer in the wavelength range of 220–300 nm (in W cm^{-2}), A = Area of the reactor (in cm^2), h = Planck's constant (in J s), c = speed of light (in m s^{-1}), λ = wavelength of incident light (in m). The wavelength range is almost the same as the absorption range (200–300 nm) of the Ga_2O_3 photocatalysts as shown in DR UV-vis spectra later.

3.3 Results and Discussion

3.3.1 Screening of dual cocatalysts

Bare Ga_2O_3 sample, the Pd/Ga_2O_3 sample and various M_1-M_2/Ga_2O_3 samples (where, M_1 = Pd, Pt and M_2 = Rh, Pt, Sm, Ir, Ni, Co, Cs, Zn, P, Fe, Au, Sb, Pb, Mn, Bi, Cu, Ag, and Sn) were examined for the photocatalytic reaction test of the NOCM in a flow reactor. The results over these samples are given in Table 1, entries 1–21. No product was observed in the dark meaning that the photoirradiation is necessary. Similarly, no product was observed in the gaseous phase without photocatalyst upon photoirradiation, indicating that the methane cannot be activated in the gaseous phase under the reaction conditions. In the photocatalytic reaction tests, the detected products were ethane, hydrogen, and propane, while other gases like ethene and propene could not be detected by the GC-FID and GC-TCD. Since the production rate of propane was usually very low and under the detection limit in many cases, only the values for ethane and hydrogen are given here. The ratio of these production rates, $R(C_2H_6/H_2)$ was also indicated as an index of the reaction selectivity for the NOCM (eq. 1) and other reactions such as the MD (eq. 2), i.e., the progress of the NOCM with complete selectivity makes R to be unity while the increase of the MD lowers the R value.

Table 1 Results of photocatalytic reaction tests of the NOCM with the bare Ga_2O_3 sample, the Pd/Ga_2O_3 sample, various dual-cocatalyst-loaded Ga_2O_3 sample, and the Bi/Ga_2O_3 sample[a]

Entry	Sample[b]	Production rates[c] / μmol h^{-1}		R^d (C_2H_6/H_2)
		C_2H_6	H_2	
1	Ga_2O_3	0.051	0.19	0.27
2	Pd/Ga_2O_3	0.31	0.73	0.43
3[e]	Pd-Rh/Ga_2O_3	0.14	0.86	0.16
4	Pd-Pt/Ga_2O_3	0.19	0.69	0.27
5	Pd-Sm/Ga_2O_3	0.31	1.0	0.31
6	Pd-Ir/Ga_2O_3	0.14	0.34	0.41
7	Pd-Ni/Ga_2O_3	0.23	0.55	0.42
8	Pd-Co/Ga_2O_3	0.18	0.42	0.43
9	Pd-Cs/Ga_2O_3	0.34	0.73	0.47

10	Pd-Zn/Ga_2O_3	0.31	0.61	0.51
11	Pd-P/Ga_2O_3	0.24	0.45	0.53
12	Pd-Fe/Ga_2O_3	0.16	0.29	0.55
13	Pd-Au/Ga_2O_3	0.33	0.57	0.58
14	Pd-Sb/Ga_2O_3	0.40	0.67	0.60
15	Pd-Pb/Ga_2O_3	0.63	0.88	0.72
16	Pd-Mn/Ga_2O_3	0.17	0.23	0.74
17[f]	Pd-Bi/Ga_2O_3	0.95	1.1	0.86
18	Pd-Cu/Ga_2O_3	0.18	0.20	0.90
19	Pd-Ag/Ga_2O_3	0.40	0.35	1.1
20	Pd-Sn/Ga_2O_3	0.29	0.24	1.2
21[e]	Pt-Bi/Ga_2O_3	0.038	0.87	0.044
22	Bi/Ga_2O_3	0.062	0.32	0.19

[a]The reaction conditions were as follows: photocatalyst in a quartz cell = 0.8 g; photoirradiation area = 4 cm^2; cell volume = 0.4 cm^3; feed gas = 10% of CH_4 in Ar (total flow rate 30 mL min^{-1}); contact time = 0.8 s; space velocity (SV) = 4500 h^{-1}; light intensity = 20 mW cm^{-2}; reaction temperature = *ca.* 320 K. [b]The loading amount of each additive element was 0.18 mol %. [c]The production rates were measured at 5.5 h after the start of the photoirradiation. [d]Calculated as follows: *R* (C_2H_6/H_2) = (production rate of ethane)/(production rate of hydrogen). [e]A very small amount of propane was also detected with the Pd-Rh/Ga_2O_3 and Pt-Bi/Ga_2O_3 samples. [f]The reaction test was done three times, and the average values are reported here.

The bare Ga_2O_3 promoted the NOCM photocatalytically (Table 1, entry 1), but the value of *R* was not unity but less than unity (*R*=0.27). The *R* value with the current Ga_2O_3 was lower than the previously employed Ga_2O_3 sample.[3] Loading of 0.18 mol % (0.1 wt. %) of Pd species increased the activity and the selectivity of the Ga_2O_3 sample although the selectivity for the NOCM was still low indicated by the value of *R* of 0.43 (Table 1, entry 2), confirming that Pd acted as a cocatalyst to improve the activity of the present bare Ga_2O_3 photocatalyst, which is also consistent with the previous report.[3] Since the Pd species improved the selectivity, it is suggested that the Pd species promoted the NOCM as the active sites and diminished the active sites for the MD.

The results for the Ga_2O_3 photocatalysts with various dual-cocatalysts including Pd species were listed in Table 1, entries 3–20. The selectivity for the NOCM decreased after co-loading of some of the transition elements (Rh, Pt, Ir, and Ni) and the inner

transition element (Sm) with Pd, while some transition elements showed equal (Co) or better selectivity (Zn, Fe, Au, Mn, Cu, and Ag) in comparison to the single Pd-loaded Ga_2O_3 sample. When the p-block elements such as P, Sb, Pb, Bi, and Sn were co-loaded with Pd, the selectivity increased. Co-loading of s-block element (Cs) resulted in slightly higher selectivity.

Among these combinations, the Pd-Bi/Ga_2O_3 photocatalyst showed the best performance with both high activity and better selectivity (Table 1, entry 17). Although Pt-Bi species was reported to enhance thermal NOCM effectively,[10] it was not good for the photocatalytic NOCM (Table 1, entry 21). For comparison, we prepared the Bi(0.18)/Ga_2O_3 sample and found the slightly higher activity and slightly lower selectivity than the bare Ga_2O_3 sample (Table 1, entry 22). Although it is clear that Bi also acted as a cocatalyst to improve the photocatalytic activity of the bare Ga_2O_3, it is fact that the Bi(0.18)/Ga_2O_3 sample gave lower activity and selectivity than the Pd(0.18)-Bi(0.18)/Ga_2O_3 photocatalyst (Table 1, entry 17). This proposed that the combination of Pd and Bi species is unique and promising for the photocatalytic NOCM.

3.3.2 Photocatalytic activity with the Pd-Bi dual cocatalyst

As mentioned above, the Pd-Bi dual cocatalyst improved the photocatalytic performance in both ethane production rate and the selectivity for the NOCM. Then, we optimized the loading amount of Pd and Bi species. The results of optimization of the loading amount of Pd and Bi cocatalysts in various Pd-Bi/Ga_2O_3 samples is shown in Figure 2 and Figure 3, respectively. A good catalyst must exhibit good selectivity for the desired product formation and minimal formation of undesired side products. A Pd(0.18)-Bi(0.05)/Ga_2O_3 sample showed the highest selectivity for the NOCM indicated by the value of R = 0.89 in the present conditions (Figure 3f) among all the tested Pd-Bi dual-cocatalyst-loaded Ga_2O_3 samples with different loading amounts of Pd and Bi species.

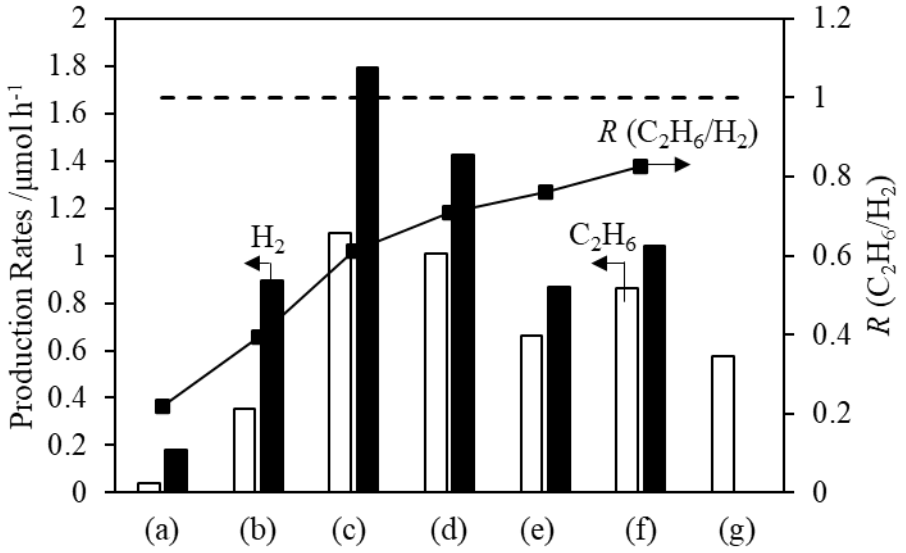

Figure 2 Production rates of ethane (white bars), hydrogen (black bars), and their ratio, *R* (black line with markers) with the samples, (a) bare Ga_2O_3, (b) Pd(0.18)/Ga_2O_3, (c) Pd(0.05)-Bi(0.18)/Ga_2O_3, (d) Pd(0.1)-Bi(0.18)/Ga_2O_3, (e) Pd(0.18)-Bi(0.18)/Ga_2O_3, (f) Pd(0.3)-Bi(0.18)/Ga_2O_3, and (g) Pd(0.4)-Bi(0.18)/Ga_2O_3 in the photocatalytic reaction tests of the NOCM. The black dashed line represents the ideal value of R =1. Reaction conditions were same as those described in the footnote *a* of the Table 1.

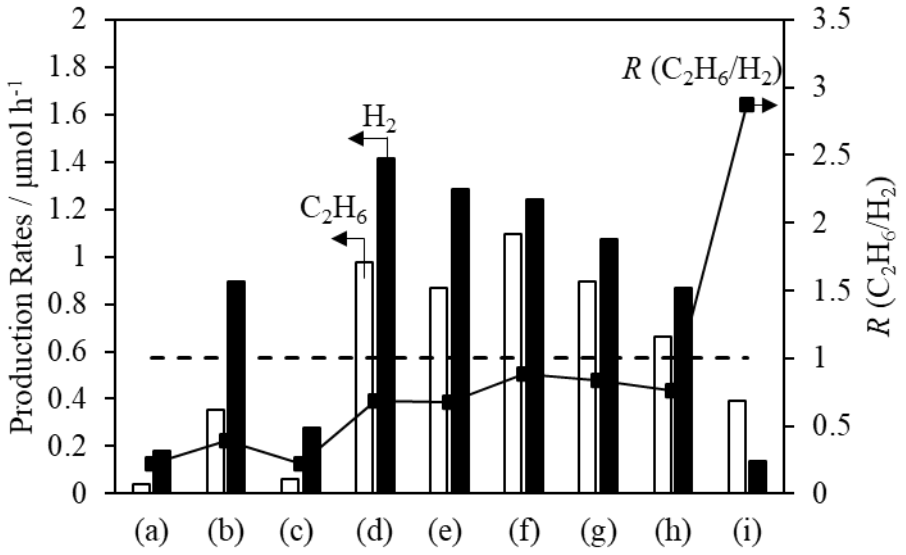

Figure 3 Production rates of ethane (white bars), hydrogen (black bars), and their ratio, *R* (black line with markers) with the samples, (a) bare Ga_2O_3, (b) Pd(0.18)/Ga_2O_3, (c) Bi(0.18)/Ga_2O_3, (d) Pd(0.18)-Bi(0.02)/Ga_2O_3, (e) Pd(0.18)-Bi(0.035)/Ga_2O_3, (f) Pd(0.18)-Bi(0.05)/Ga_2O_3, (g) Pd(0.18)-Bi(0.1)/Ga_2O_3, (h) Pd(0.18)-Bi(0.18)/Ga_2O_3, and (i) Pd(0.18)-Bi(0.4)/Ga_2O_3 in the photocatalytic reaction tests of the NOCM. The

black dashed line represents the ideal value of R =1. Reaction conditions were same as those described in the footnote *a* of the Table 1.

The optimized Pd(0.18)-Bi(0.05)/Ga_2O_3 photocatalyst exhibited a stable and continuous production of ethane and hydrogen in nearly equimolar ratio (R=0.8–1.2) with production rates 1.10 and 1.24 μmol h^{-1}, respectively at 5.5 h later, after an induction period of a few hours (Figure 4). Methane conversion (0.033 %) exceeded thermodynamic equilibrium value.

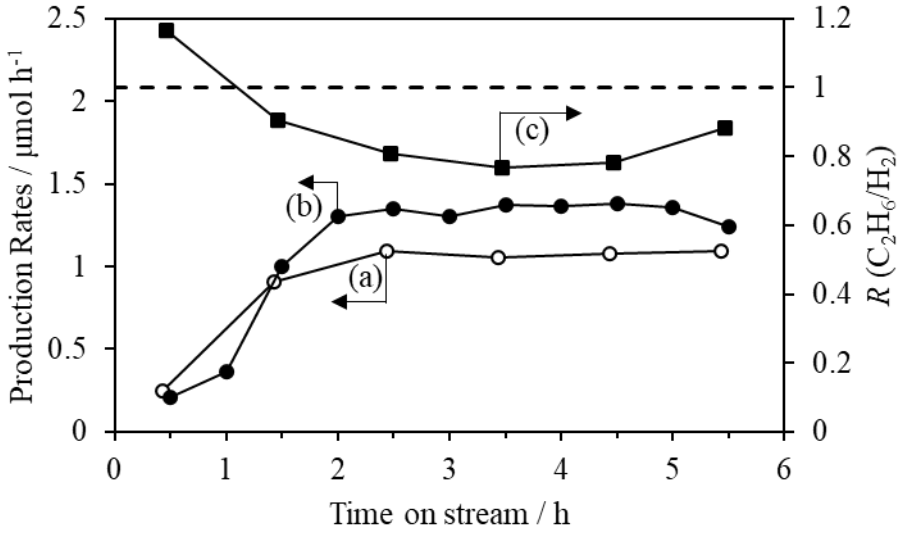

Figure 4 Time course of the production rate of (a) ethane, (b) hydrogen, (c) their ratio, R in the photocatalytic reaction test of the NOCM with the Pd(0.18)-Bi(0.05)/Ga_2O_3 sample. The black dashed line represents the ideal value of R =1. Reaction conditions were same as those described in the footnote *a* of the Table 1.

Further, when various total loading amounts of the Pd-Bi species with unchanged Pd/Bi ratio were examined, either increasing or decreasing the total loading amount resulted in a decrease in the selectivity as shown in Figure 5.

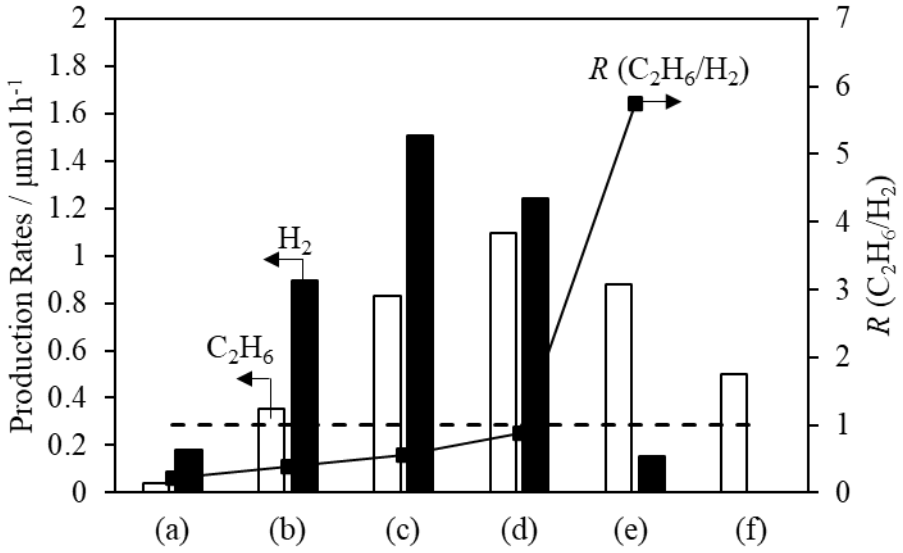

Figure 5 Production rates of ethane (white bars), hydrogen (black bars), and their ratio, *R* (black line with markers) with the samples, (a) bare Ga_2O_3, (b) Pd(0.18)/Ga_2O_3, (c) Pd(0.09)-Bi(0.025)/Ga_2O_3, (d) Pd(0.18)-Bi(0.05)/Ga_2O_3, (e) Pd(0.36)-Bi(0.1)/Ga_2O_3, and (f) Pd(0.54)-Bi(0.15)/Ga_2O_3 in the photocatalytic reaction tests of the NOCM. The black dashed line represents the ideal value of *R* =1. Reaction conditions were same as those described in the footnote *a* of the Table 1.

To examine whether thermal energy can drive the reaction in the dark or not, the reaction temperature was increased without photoirradiation with the Pd(0.18)-Bi(0.05)/Ga_2O_3 sample and the results are shown in Table 2.

Table 2 Effect of increasing the temperature in the dark with the Pd(0.18)-Bi(0.05)/Ga_2O_3 sample

Entry	Temperature / K	Production rates[a] / μmol h^{-1}		R^b (C_2H_6/H_2)
		C_2H_6	H_2	
1	323	nd[c]	nd[c]	–[d]
2	373	nd[c]	nd[c]	–[d]
3	473	nd[c]	nd[c]	–[d]
4	573	nd[c]	0.38	0

[a]The production rates were measured after 1.5 h from the start of the photoirradiation. [b]Calculated as follows: $R(C_2H_6/H_2)$ = (production rate of ethane)/(production rate of hydrogen). [c]nd: not detected. [d]The $R(C_2H_6/H_2)$ value could not be calculated. Other reaction conditions were same as those described in the footnote *a* of Table 1.

No products were detected at 323 K, 373 K and 473 K (Table 2, entries 1–3), while only hydrogen was detected at 573 K (Table 2, entry 4). A color change was observed after the reaction probably due to the MD to form coke (Figure 6). This result indicates that the NOCM did not proceed in the dark and the MD took place at higher temperature.

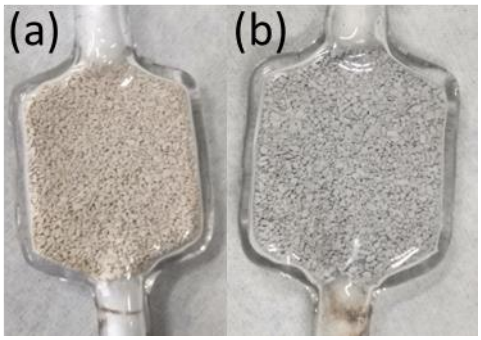

Figure 6 The photographs of the sample cell (a) before and (b) after the reaction test with the Pd(0.18)-Bi(0.05)/Ga_2O_3 sample at 573 K in the dark

The long time reaction tests were carried out with the two samples, Pd(0.18)/Ga_2O_3 and Pd(0.18)-Bi(0.18)/Ga_2O_3. Figure 7A shows the time course of the reaction over the Pd(0.18)/Ga_2O_3 sample. The production rates of both ethane and hydrogen achieved the highest values at nearly 2.5 h and then decreased by 54 % and 58 %, respectively during a time on stream of 117 h while the ratio of the ethane and hydrogen was always lower than unity, $R(C_2H_6/H_2)$=0.30–0.62. Thus, the single Pd cocatalyst loaded gallium oxide caused also the MD to form coke and hydrogen (Eq. 2) as a competitive reaction, which would be the reason for the decrease of the photocatalytic activity, although obvious color change of Pd/Ga_2O_3 due to coke formation was not observed as discussed in a later section and the amount of possibly produced coke could not be determined by thermogravimetry or Raman spectroscopy, probably due to its small amount. On the other hand, the Pd(0.18)-Bi(0.18)/Ga_2O_3 photocatalyst promoted the NOCM reaction selectively and continuously as shown in Figure 7B, where both ethane and hydrogen were yielded from methane stably at least for 100 h in nearly equimolar ratio, $R(C_2H_6/H_2)$=0.78–1.10, after an initial induction

period. The average production rates of ethane and hydrogen were same, i.e.; 1.11 μmol h^{-1} with the selectivity for the NOCM being 100 % indicated by the average value of *R* being 1 and the average methane conversion was 0.032 % after the initial induction period over the Pd-Bi/Ga_2O_3 photocatalyst.

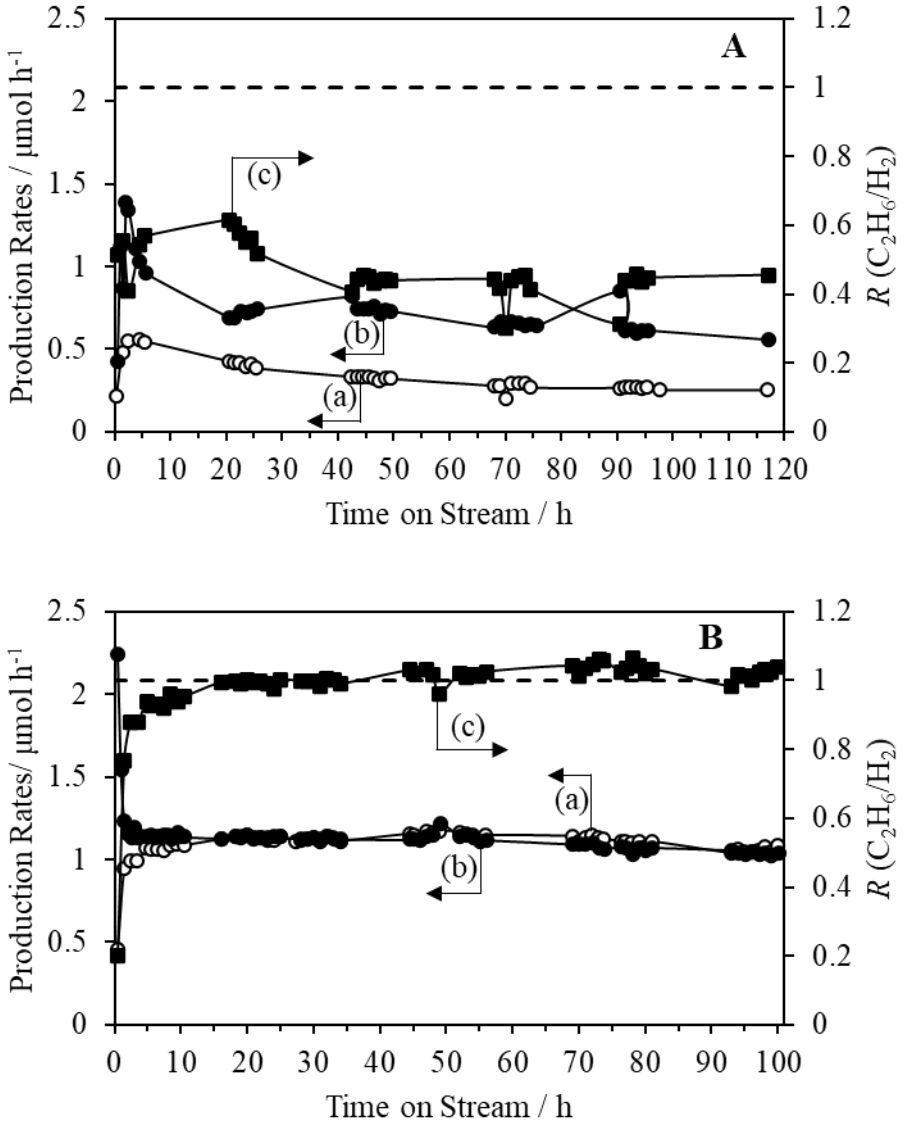

Figure 7 Time course of the production rate of (a) ethane, (b) hydrogen, (c) their ratio, *R* in the photocatalytic reaction test of the NOCM with (A) the Pd(0.18)/Ga_2O_3 sample and (B) the Pd(0.18)-Bi(0.18)/Ga_2O_3 sample. The dots are the actual datapoints obtained in the experiments and the smooth curves are the guides to the eye. The black dashed line represents the ideal value of *R* =1. Reaction conditions were same as those described in the footnote *a* of the Table 1.

The recyclability was also tested and the activity as well as the selectivity was nearly intact after 3 cycles as shown Figure 8.

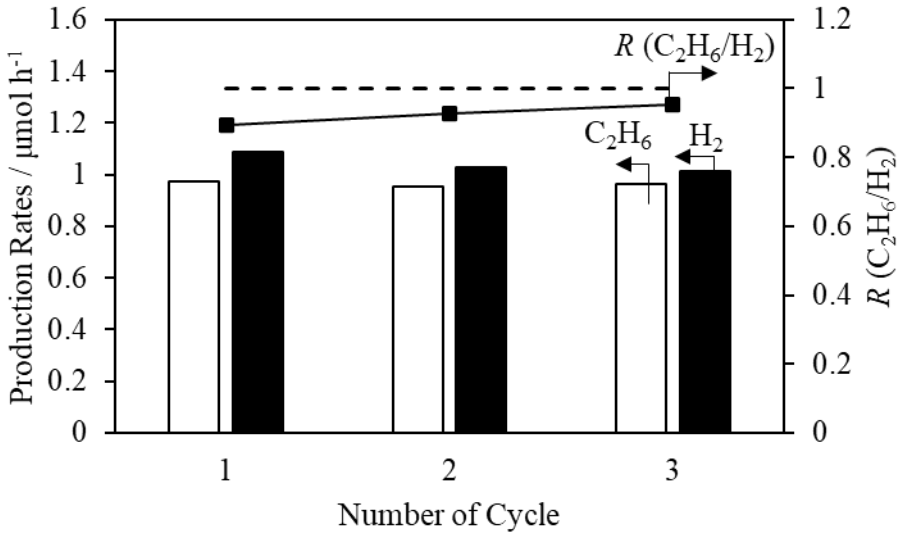

Figure 8 Production rate of ethane (white bars), hydrogen (black bars) and their ratio, *R* (black line with markers) in the recycle tests with the Pd(0.18)-Bi(0.18)/Ga_2O_3 sample. The sample was collected after the one cycle of the NOCM reaction test and then used for the next cycle as it was without any treatment. The black dashed line represents the ideal value to *R* =1. The reaction conditions were the same as those described in the footnote *a* of Table 1.

These results revealed that the Pd-Bi/Ga_2O_3 sample promoted the desired NOCM without the undesired coke formation in the MD, indicating the important role of the Bi species in the formation of C2 products (ethane) and in making the catalyst stable under the reaction conditions. In literatures, Bi cocatalyst was reported to control the strong catalysis of Ni towards C–H bond cleavage in case of Ni-Bi bimetallic catalyst[11] and stabilize the catalyst in case of Pt-Bi bimetallic catalyst[10] in thermal NOCM reactions. The role of the Bi species in the current photocatalysis will be further discussed later.

3.3.3 Comparison with other photocatalysts

In order to investigate the role of Ga_2O_3, we tested other metal oxides photocatalysts and the results are given in Table 3. As mentioned above, the Ga_2O_3 sample showed production of both C_2H_6 and H_2 from methane upon photoirradiation

(Table 3, entry 1). Other photocatalysts such as CeO_2 and ZnO showed ethane production but no production of hydrogen (Table 3, entries 2-3). Although TiO_2 (ST-01) shows production of both C_2H_6 and H_2 from methane (Table 3, entry 4), its color on the irradiated side was changed from white to blue during the reaction as shown in Figure 9. The color of titanium dioxide granules on the upper side of the sample cell was turned to white again immediately after exposure to the air when the reactor cell was removed from the set-up. These results suggest that these metal oxides were possibly reduced by H_2 upon photoirradiation and were not stable in the present conditions. Thus, the stability of the catalyst under the reductive conditions of the present reaction, i.e., in the presence of H_2, CH_4, and C_2H_6 upon photoirradiation, should be a prerequisite for a catalyst to be active for the NOCM. The Al_2O_3 and SiO_2 samples that are stable in such conditions were also active for the NOCM (Table 3, entries 5-6) as reported previously.[12,13]

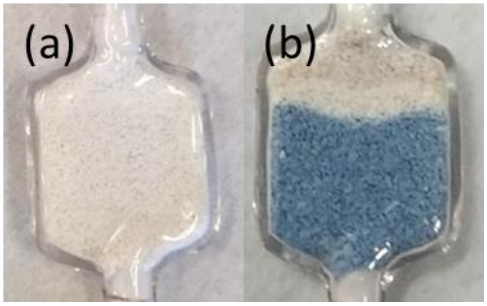

Figure 9 The photographs of the sample cell (a) before and (b) after the reaction test of the NOCM over the bare TiO_2 (ST-01) sample.

We prepared the palladium bismuth dual-cocatalyst loaded metal oxides samples, where the compositions of these cocatalysts were 0.18 mol%. Even when the Pd-Bi dual cocatalysts were loaded on these metal oxides, the photocatalytic activities for the NOCM were not improved except for the Pd-Bi/Ga_2O_3 photocatalyst (Table 3, entries 7–12). Thus, the combination of the Pd-Bi dual cocatalyst and Ga_2O_3 photocatalyst is important for the high activity and selectivity for the NOCM.

Table 3 Results of photocatalytic reaction tests for the NOCM over the bare and Pd-Bi dual cocatalyst loaded various metal oxide samples as well as an Au/TiO_2 sample

Entry	Sample[a]	Production rates[b] / μmol h^{-1}		R^c (C_2H_6/H_2)
		C_2H_6	H_2	
1	Ga_2O_3	0.051	0.19	0.27
2	CeO_2	0.051	nd[d]	–[e]
3	ZnO	0.080	nd[d]	–[e]
4	TiO_2[f]	0.055	0.090	0.61
5	Al_2O_3	0.035	0.50	0.070
6	SiO_2	0.030	0.11	0.27
7	Pd-Bi/Ga_2O_3	0.95	1.1	0.86
8	Pd-Bi/CeO_2	0.051	nd[d]	–[e]
9	Pd-Bi/ZnO	0.12	nd[d]	–[e]
10	Pd-Bi/TiO_2[f]	0.40	nd[d]	–[e]
11	Pd-Bi/Al_2O_3	0.050	nd[d]	–[e]
12	Pd-Bi/SiO_2	nd[d]	nd[d]	–[e]
13[g]	Au/TiO_2[h]	0.30	0.22	1.3

[a]The loading amount of each Pd and Bi was 0.18 mol%. [b]The production rates were measured after 5.5 h of photoirradiation. [c]Calculated as follows: $R(C_2H_6/H_2)$ = (production rate of ethane)/(production rate of hydrogen). [d]n.d.: not detected. [e]The $R(C_2H_6/H_2)$ value could not be calculated. [f]A TiO_2 sample of anatase phase (ST-01) was used in the reaction tests. [f]The reaction test with the Au(0.41 mol%)/TiO_2 sample was done two times and the average values were listed here. [g]A TiO_2 sample of mixture of anatase and rutile phases (P-25) was used in the reaction test. Other reaction conditions were the same as those described in the footnote *a* of Table 1 except the weight of the sample.

Since Au loaded TiO_2 photocatalyst (Au/TiO_2) was recently reported as one of the best photocatalysts for the NOCM,[4] it was prepared following the procedure described in the literature and examined for the NOCM in the present conditions. The Au/TiO_2 sample showed production of both ethane and hydrogen from methane upon photoirradiation as shown in Table 3, entry 13, confirming that the NOCM took place over the Au/TiO_2 sample as reported. However, it is notable that the Pd(0.18)-Bi(0.05)/Ga_2O_3 sample, as the best photocatalyst in the present study, provided clearly higher production rates than the Au/TiO_2 sample under the present reaction conditions.

3.3.4 How to report the photocatalytic activity

To develop an efficient photocatalytic material, the experimental trials are necessary and the powder or granules of the samples are easy-handled in the experimental procedure. In the present flow reactor, the thickness of the cell was 1 mm to accept the granules and thus, only the surface layer on the irradiated side is considered to be photoexcited, which is one of the reasons for the low methane conversion in this type reactor conditions. Actually, when the color of the photocatalyst was changed during the photocatalytic reaction test such as the case of TiO_2 sample, the color change was observed mostly on one side, i.e., the irradiated side. The granules in the back side could contribute very less to the photocatalytic conversion. To efficiently use the space in the sample cell and to know the optimum amount of the photocatalyst in the sample cell, the photocatalyst granules were diluted with quartz sand and tested for the photocatalytic reaction test (Figure 10).

The quartz sand is transparent to UV-light and it was confirmed to be inactive for the NOCM (Figure 10, 0% of photocatalyst). Thus, the dilution of the photocatalyst granules by the quartz sand would allow the light reach inner layers in the sample cell. The granules of the Pd(0.18)-Pb(0.18)/Ga_2O_3 photocatalyst were mixed with the quartz sand in various ratios (0–100% in weight) keeping other parameter such as the irradiation area constant. The production rate increased with the increase of the photocatalyst ratio from 0% to 50% as shown in Figure 10. However, the diluted samples consisting of 50% and 100% of the photocatalyst gave almost the same photocatalytic performance even though the weight of the photocatalyst was double in the latter sample. The *R* values for all the cases were almost the same in the range of 0.7–0.8, meaning the selectivity was not varied with the dilution of the Pd(0.18)-Pb(0.18)/Ga_2O_3 sample. These results indicate that the production rates were not proportional to the weight of the photocatalyst granules while the selectivity was unchanged and the 50% dilution of the photocatalyst granules with quartz sand provides the most efficient use of the light energy with a minimum photocatalyst weight in the present reactor under the reaction conditions. In recent literatures,[4,14–17] the production rate per photocatalyst weight (μmol $g_{catalyst}^{-1}$ h^{-1}) or metal weight (μmol g_{metal}^{-1} h^{-1}) were often reported. However, it should be noted that this notation for the photocatalytic performance would not be adequate for comparison because the reaction rate was not linear to the catalyst weight as shown in Figure 10. If calculated, the Pd(0.18)-Pb(0.18)/Ga_2O_3 sample gave 4.4, 2.7, 1.5, or 0.77 μmol $g_{catalyst}^{-1}$ h^{-1} ethane production

and 5.5, 3.6, 2.1, or 1.0 μmol $g_{catalyst}^{-1}$ h^{-1} hydrogen production in the case of 10, 25, 50, or 100% mixture in this experiment, respectively, even though the same photocatalyst was used under the same reaction conditions.

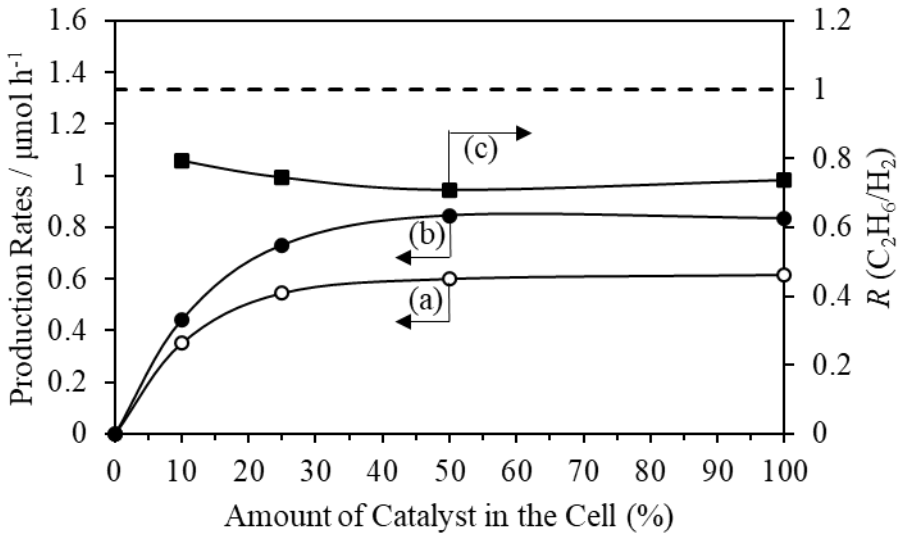

Figure 10 Production rates of (a) ethane, (b) hydrogen, (c) their ratio, *R* in the photocatalytic reaction test of the NOCM as a function of amount of the photocatalyst in the sample cell. The photocatalyst used in these experiment was the Pd(0.18)-Pb(0.18)/Ga_2O_3 sample. The total weight of the photocatalyst and the quartz sand was 0.8 g. As an example, 10% of photocatalyst means that an even mixture of 0.08 g of photocatalyst granules and 0.72 g quartz sand was used for the reaction test. The black dashed line represents the ideal value to *R* =1. The reaction conditions were same as those described in the footnote *a* of Table 1.

The photocatalytic performance should be determined by other factors such as quantum efficiency. The apparent quantum efficiency (AQE) for H_2 was estimated to be 0.2 % at the wavelengths of 200–300 nm with the Pd(0.18)-Bi(0.05)/Ga_2O_3 sample as the best photocatalyst in the present study.

3.3.5 Characterization of the Pd-Bi/Ga_2O_3 photocatalyst

The crystal structure of the samples was determined by powder XRD. The XRD pattern of the present bare Ga_2O_3 sample (Figure 11 b) was almost similar to that of β-Ga_2O_3 crystal from a database (Figure 11 a, ICSD#34243)[18] except for some additional diffraction lines. The lines at 24.5, 33.8, 36.2, 41.5, 50.3, and 55.1° are assignable to α-

Ga_2O_3 phase (ICSD#27431),[19] and the line at 36.2° is assignable also to γ-Ga_2O_3 phase (ICSD#152085).[20] This means that the present commercially obtained Ga_2O_3 sample was a mixed crystal consisting mainly of β-Ga_2O_3 phase including minor portions of α-Ga_2O_3 and γ-Ga_2O_3 phases. No new lines were observed in the XRD patterns after loading of Pd, Bi and Pd-Bi cocatalysts on the gallium oxide possibly due to low loading amount and high dispersion (Figure 11 c–e).

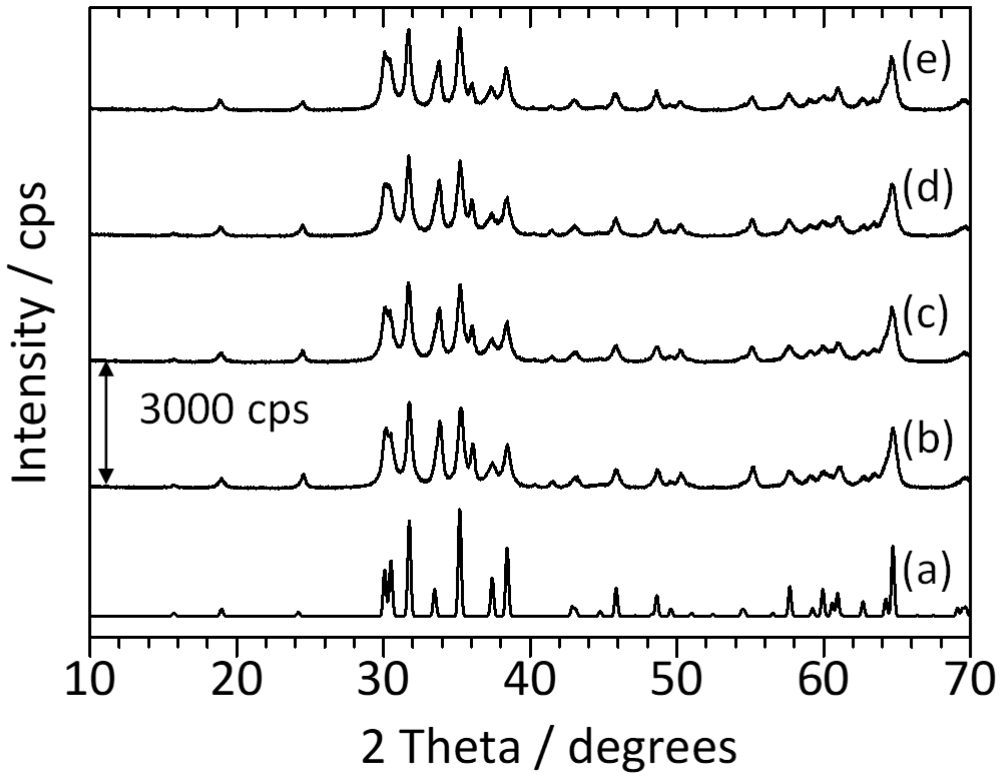

Figure 11 XRD patterns of (a) β-Ga_2O_3 from a database (ICSD#34243), and the samples, (b) bare Ga_2O_3, (c) Pd(0.18)/Ga_2O_3, (d) Bi(0.18)/Ga_2O_3, and (e) Pd(0.18)-Bi(0.05)/Ga_2O_3. The intensity of XRD pattern of β-Ga_2O_3 from the database was multiplying by a factor of 0.35.

The specific surface area of the bare Ga_2O_3 sample, the Bi/Ga_2O_3 sample, the Pd/Ga_2O_3 sample and the Pd-Bi/Ga_2O_3 samples were nearly the same as given in Table 4, meaning that the cocatalyst loading procedure did not decrease but rather slightly increase the SSA of the Ga_2O_3 samples. Secondary particles of the purchased Ga_2O_3 might be dispersed by the impregnation procedure including stirring in the solution, evaporation, and calcination.

Table 4 The specific surface areas (SSA) of the various samples

Entry	Sample	SSA[a] (m^2g^{-1})
1	Ga_2O_3	14.4 (± 0.3)
2	Bi(0.18)/Ga_2O_3	16.9 (± 0.1)
3	Pd(0.18)/Ga_2O_3	17.6 (± 0.2)
4	Pd(0.18)-Bi(0.18)/Ga_2O_3	16.5 (± 0.2)
5	Pd(0.18)-Bi(0.05)/Ga_2O_3	15.7 (± 0.2)

[a]The value in parenthesis is a standard deviation calculated from multiple measurements.

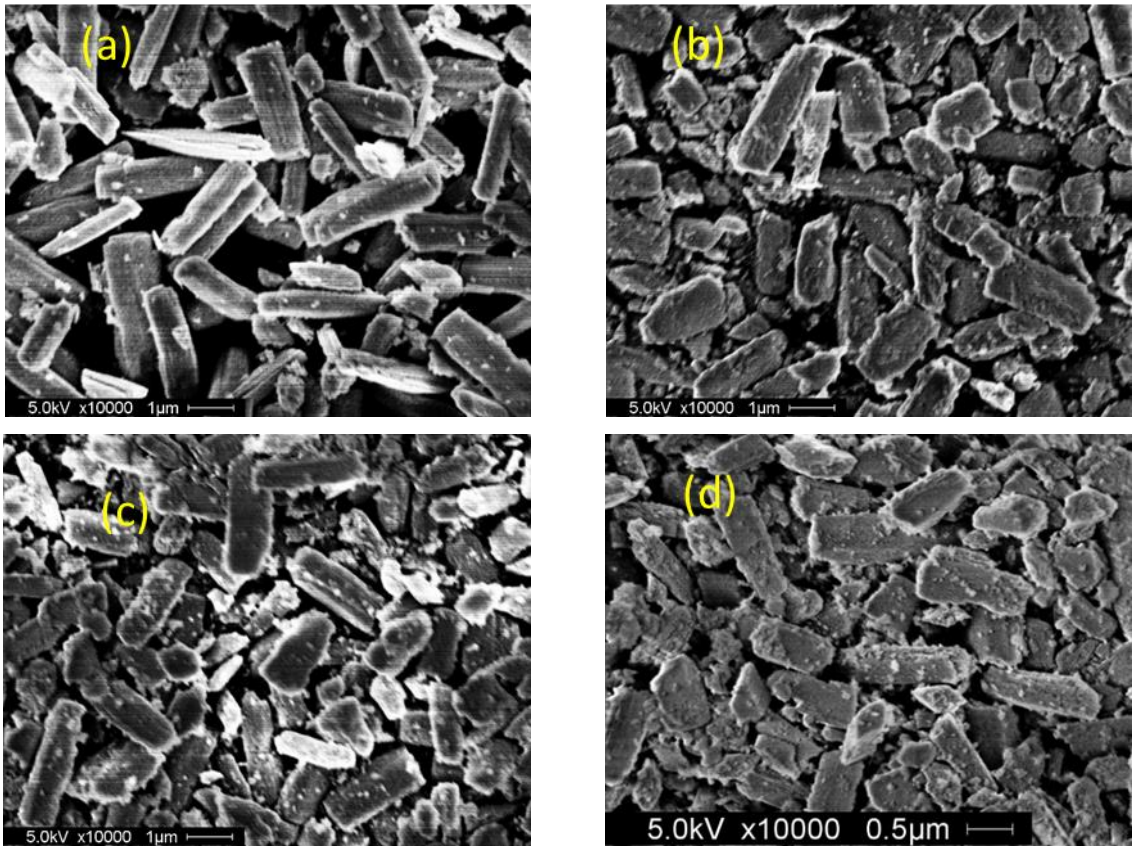

Figure 12 SEM images of the samples, (a) bare Ga_2O_3, (b) Pd(0.18)/Ga_2O_3, (c) Bi(0.18)/Ga_2O_3, and (d) Pd(0.18)-Bi(0.05)/Ga_2O_3.

The SEM images of the samples are shown in Figure 12. Pillar-shaped particles with some cracks having an average length of 1 μm were observed for the bare Ga_2O_3 sample (Figure 12 a) as reported in the literature.[3,21] The average particle size and the morphology of the gallium oxide particles did not change much after cocatalysts loading while small and broken particles increased because of the procedure to prepare these

samples mentioned above, which should be related to the increase of the SSA. We could observe some nanoparticles on the surface of Pd/Ga_2O_3, Bi/Ga_2O_3 and $Pd\text{-}Bi/Ga_2O_3$ samples (Figure 12 b-d, respectively), but we could not confirm whether these nanoparticles derived from cocatalysts or not because similar nanoparticles were also found on the surface of bare Ga_2O_3 sample to some extent (Figure 12 a).

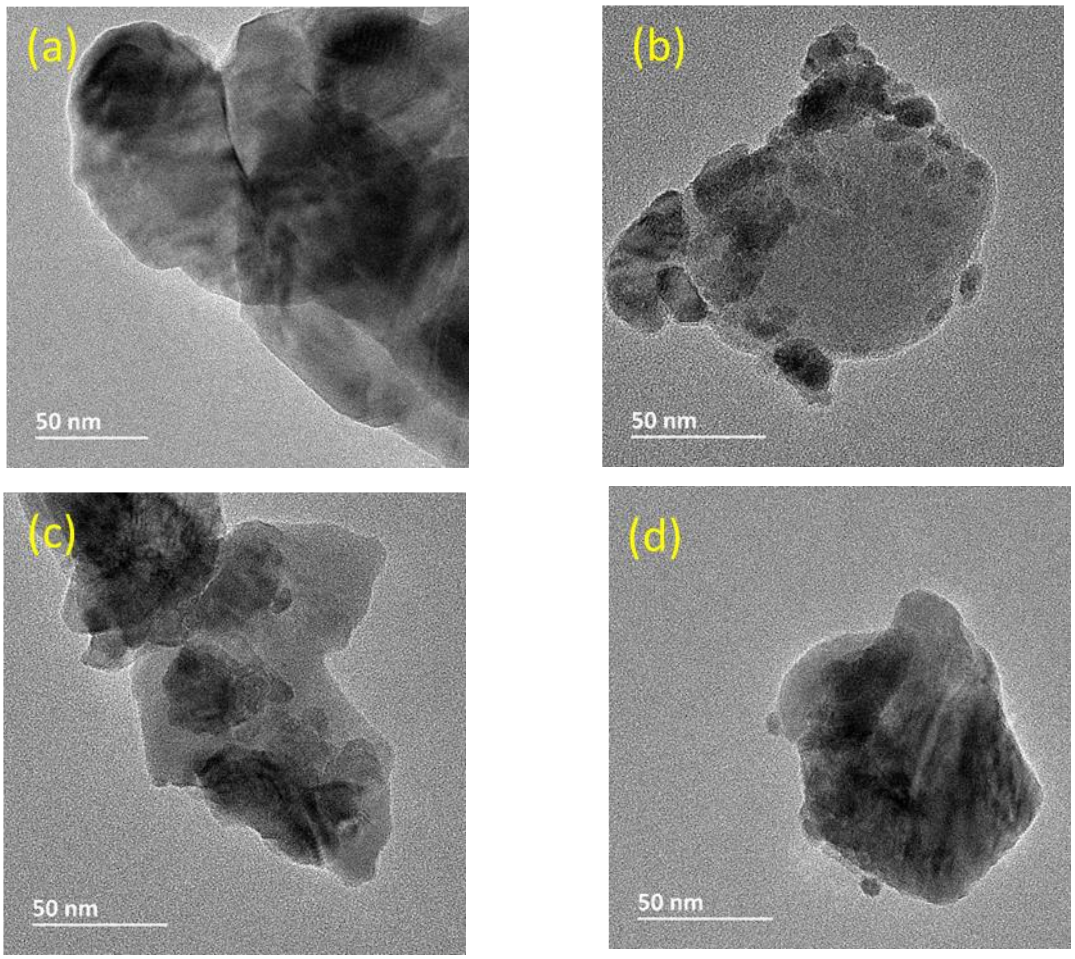

Figure 13 TEM images of the samples, (a) bare Ga_2O_3, (b) $Pd(0.18)/Ga_2O_3$, (c) $Bi(0.18)/Ga_2O_3$, and (d) $Pd(0.18)\text{-}Bi(0.05)/Ga_2O_3$.

The TEM images of the bare Ga_2O_3 sample, the Pd/Ga_2O_3 sample, the Bi/Ga_2O_3 sample, and the $Pd\text{-}Bi/Ga_2O_3$ sample are shown in Figure 13. Some nanoparticles could be observed by TEM on all the cocatalyst loaded samples. The average particle size of the cocatalyst nanoparticles on the surface of the $Pd(0.18)\text{-}Bi(0.05)/Ga_2O_3$ sample was nearly 5 nm. However, it was difficult to clarify the elements of these particles by energy dispersive X-ray spectroscopy (EDX) due to the extremely low loading amount of the cocatalysts. To solve this limitation, we prepared a $Pd(3.6)\text{-}Bi(1)/Ga_2O_3$ sample of the higher loading amounts with the unchanged molar ratio of Pd and Bi by the co-

impregnation method and performed the TEM measurements and elemental mappings (Figure 14) although this sample was less active for the NOCM (0.27 and 0.0 μmol h^{-1} for C_2H_6 and H_2 formations, respectively).

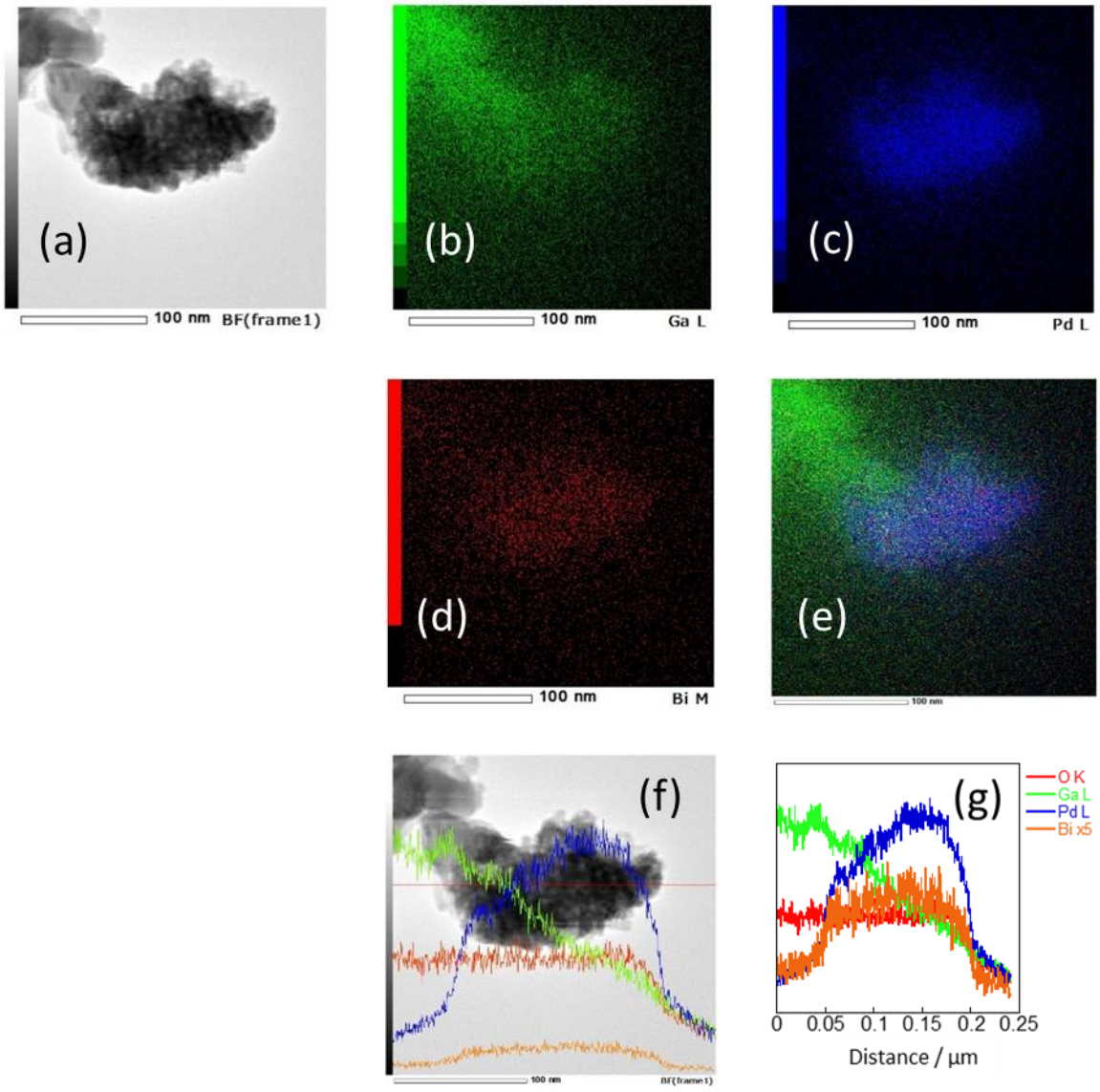

Figure 14 TEM image (a), elemental mappings (b-e), and line-scan analysis (f-g) of a single particle of the Pd(3.6)-Bi(1)/Ga_2O_3 sample.

The particle size of the gallium oxide remained almost the same even in the higher loading amount sample. As can be seen by the EDX mappings in Figure 14b-e, the Pd and Bi species were dispersed on Ga_2O_3 in the Pd(3.6)-Bi(1)/Ga_2O_3 sample. Moreover, the Pd species and the Bi species seems to be located in the vicinity of each other in the Pd(3.6)-Bi(1)/Ga_2O_3 sample. The line scan analysis showed that the Pd and Bi species are located at the same place in the Pd(3.6)-Bi(1)/Ga_2O_3 sample (Figure 14f–g). The additional XRD analysis of this Pd(3.6)-Bi(1)/Ga_2O_3 sample did not show any

lines related to the presence of Pd-Bi mixed species, although we cannot deny their possible formation on the Ga_2O_3 particle in the Pd-Bi/Ga_2O_3 photocatalysts in the present study.

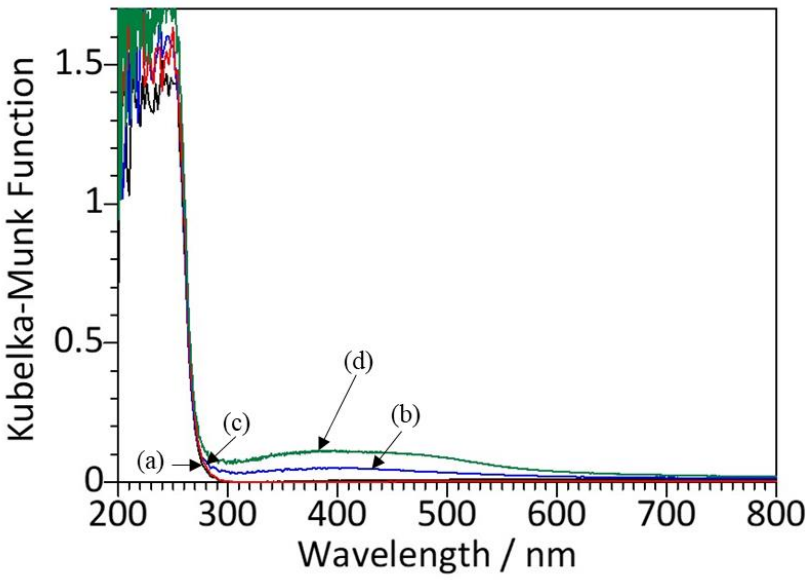

Figure 15 DR UV-vis spectra of the samples, (a) bare Ga_2O_3, (b) Pd(0.18)/Ga_2O_3, (c) Bi(0.18)/Ga_2O_3, and (d) Pd(0.18)-Bi(0.05)/Ga_2O_3.

The photoabsorption properties of the samples were investigated by UV-vis spectroscopy. As shown in Figure 15, the bare Ga_2O_3 sample exhibited a large absorption in the range of wavelengths shorter than 300 nm (Figure 15a), from which the bandgap was estimated to be around 4.6 eV that agrees with literature.[22] The spectrum did not change after loading of Bi cocatalyst (Figure 15c). The absorption in the wavelength range of 280–700 nm increased after loading of Pd cocatalyst (Figure 15b) probably due to the absorption by the PdO species.[23] This suggests that the impregnation method followed by the calcination at 773 K provides the metal oxide species on the Ga_2O_3 surface without changing the band structure of Ga_2O_3 drastically.[24] Absorption in the similar range increased after loading of Pd-Bi dual-cocatalysts (Figure 15d), suggesting that the optical property of the Pd species in the Pd-Bi/Ga_2O_3 sample was not varied, although the intensity was slightly enhanced, by the presence of the Bi species during the preparation procedure or the resulting surface of the sample.

Pd K-edge XAFS spectra were recorded in a fluorescence mode and the results are shown in Figure 16. The similar shapes of the XAFS spectra of PdO (Figure 16b) and that of the Pd-Bi/Ga_2O_3 sample before the reaction (Figure 16c) reveals that

palladium exists as Pd(II) species in the Pd-Bi/Ga_2O_3 photocatalyst. The XAFS spectra of the Pd-Bi/Ga_2O_3 sample changed after the reaction (Figure 16d) and it resembled partly to both ,the spectra of Pd foil (Figure 16 a) and PdO (Figure 16 b). This indicates that the Pd(II) species was reduced to Pd(0) under the photocatalytic reaction conditions and thus the Pd-Bi/Ga_2O_3 photocatalyst contained both Pd(0) and Pd(II) species after the reaction.

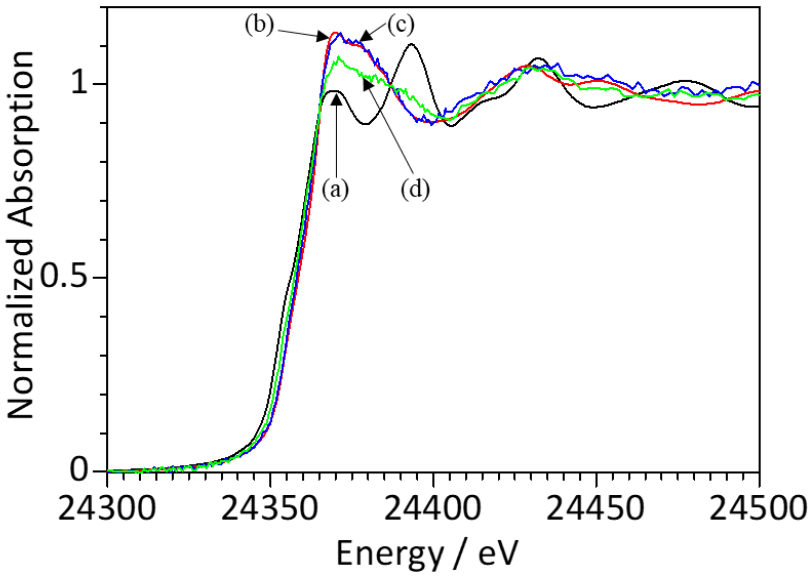

Figure 16 Pd K-edge XAFS of (a) Pd foil, (b) PdO, the Pd(0.18)-Bi(0.05)/Ga_2O_3 sample (c) before the reaction test, and (d) after the reaction test.

As mentioned previously, since mostly the photocatalyst granules located on the irradiated side in the employed flow reactor are photoexcited, the PdO species on Ga_2O_3 particle were reduced to metallic Pd mostly on the irradiated Pd-Bi/Ga_2O_3 granules and less reduction occurred on the Pd-Bi/Ga_2O_3 granules located on the non-irradiated back side as shown in Figure 17. This should be the reason for the presence of both Pd(II) and Pd(0) species on the Pd-Bi/Ga_2O_3 sample after the reaction. This result is also supported by an induction period at the beginning of the reaction over the Pd-Bi/Ga_2O_3 photocatalyst (Figure 4). Thus, it is suggested that the palladium species loaded on the Ga_2O_3 sample by the impregnation and subsequent calcination leads to the formation of PdO species on the Ga_2O_3 surface, which in turn is reduced to form metallic Pd species by hydrogen or hydrocarbons under photoirradiation during the photocatalytic reaction test.

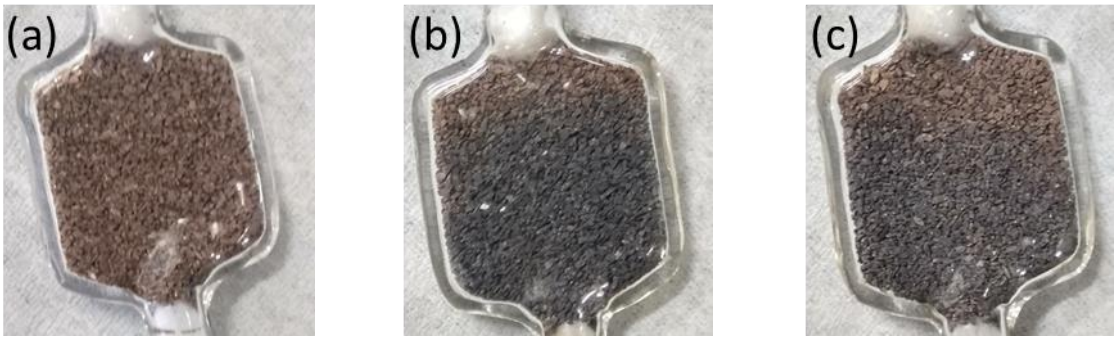

Figure 17 Photographs of the sample cell filled with granules of the Pd(3.6)-Bi(1)/Ga_2O_3 sample for the photocatalytic NOCM reaction test; (a) before the reaction test, (b) the irradiated side after the reaction test, (c) the back side after the reaction test.

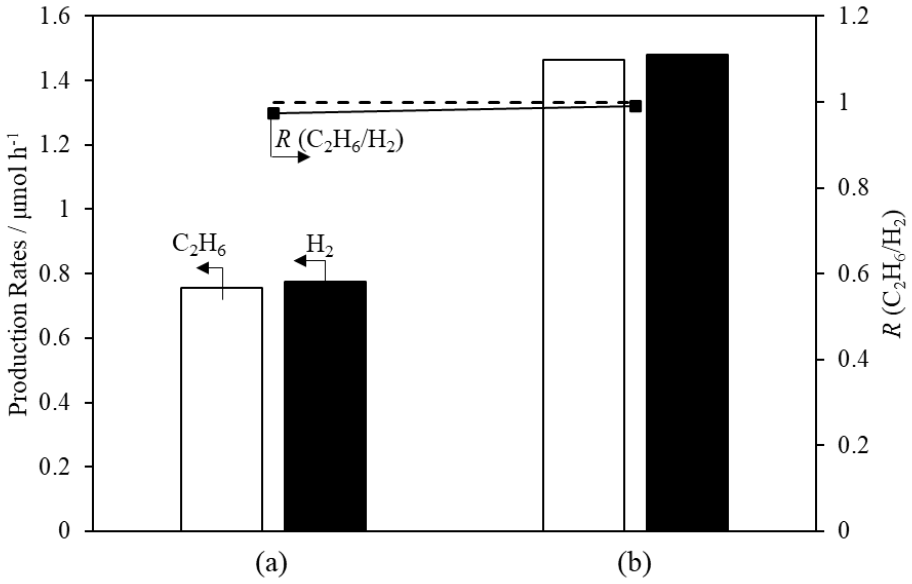

Figure 18 Production rates of ethane (white bars), hydrogen (black bars), and their ratio, *R* (black line with markers) with the samples, (a) Pd(0.18)-Bi(0.18)/Ga_2O_3 and (b) *r*-Pd(0.18)-Bi(0.18)/Ga_2O_3. The black dashed line represents the ideal value to *R* =1. The reaction conditions were same as those described in the footnote *a* of Table 1

As an additional experiment, we pretreated the Pd-Bi/Ga_2O_3 sample under a flow of H_2 at 673 K for 0.5 h to reduce the PdO species completely to metallic Pd and represented it as the *r*-Pd-Bi/Ga_2O_3 sample. We then did the reaction test with this *r*-Pd-Bi/Ga_2O_3 sample and the results are shown in Figure 18. As expected, the activity over the reduced sample increased by nearly two times in comparison to the sample without pretreatment while the selectivity remained unchanged. This result further supports that metallic Pd is the active state of palladium in the Pd-Bi/Ga_2O_3 sample.

Due to the extremely low loading amount of Bi and majorly due to the absorption of the fluorescence of Bi by Ga, we could not determine its electronic state in the Pd-Bi/Ga_2O_3 sample by XAFS analysis in the present conditions of the fluorescence mode. We assume that Bi species are in oxide state (BiO_x) since we prepared the Pd-Bi/Ga_2O_3 sample by co-impregnation method followed by calcination.

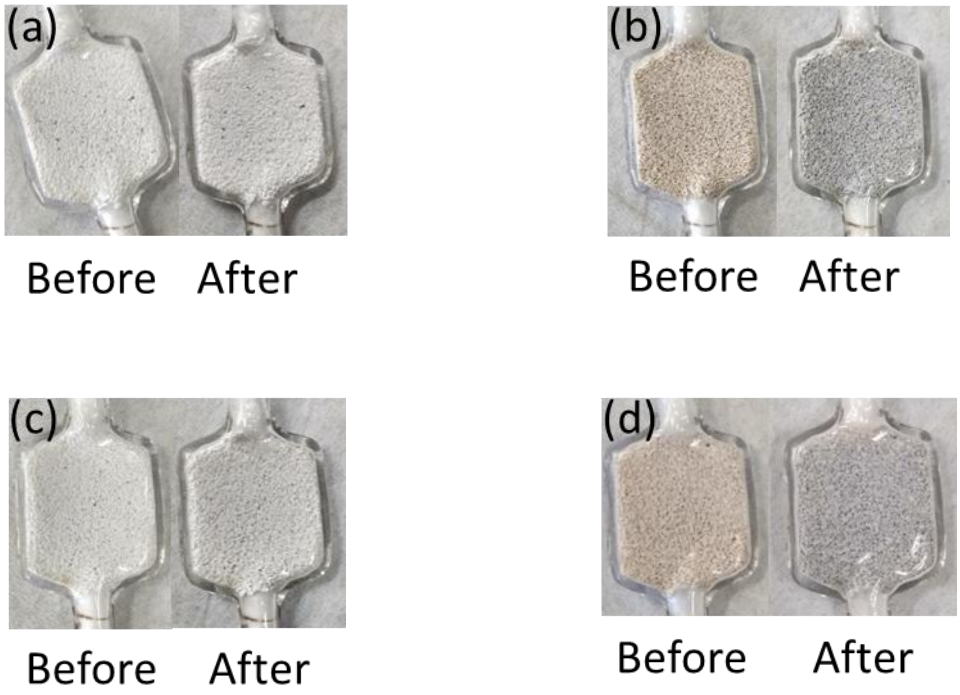

Figure 19 Photographs of the sample cell before and after the reaction test over the samples (a) bare Ga_2O_3, (b) Pd(0.18)/Ga_2O_3, (c) Bi(0.18)/Ga_2O_3, and (d) Pd(0.18)-Bi(0.05)/Ga_2O_3

Figure 19 shows the photographs of the sample cell before and after the reaction over various samples. The color of the catalyst does not change significantly after the reaction over the bare Ga_2O_3 sample (Figure 19a) and the Bi/Ga_2O_3 sample (Figure 19c) while a color change was observed after the reaction over both the Pd/Ga_2O_3 sample (Figure 19b) and the Pd-Bi/Ga_2O_3 sample (Figure 19d). This color change was most probably due to the reduction of PdO species to Pd, which was supported by the XAFS results. Further, the photocatalytic activity of these sample gradually increased in their induction periods (Figure 4, Figure 7A-B). Based on these results, we concluded that metallic Pd is the active species in the Pd-Bi/Ga_2O_3 photocatalysts for the NOCM of the steady state. Although the color change due to the reduction of the Pd species was also observed with the Pd/Ga_2O_3 sample, there was no clear difference between color change

due to this reduction (Figure 19b) and due to coke formation (Figure 6), suggesting the coke formation that would take place on the Pd/Ga_2O_3 sample could not be clearly confirmed by the color change.

3.3.6 Role of dual cocatalyst species

3.3.6.1 Reaction test with UV cut-off filter

As mentioned above, the Pd-Bi/Ga_2O_3 sample exhibited the absorption band in the wavelength range of 280–700 nm (Figure 15d, green line) with higher intensity than that for the Pd/Ga_2O_3 sample. In order to know whether this photoexcitation directly contributes to the photocatalytic activity of the sample, we did a reaction test with a UV cut-off filter passing only the light of wavelengths larger than 330 nm and the results are given in Table 5. In contrast to the higher activity without using the optical filter (Table 5, entry 1), very small amount of ethane and no hydrogen were observed when the filter was used (Table 5, entry 2). These results indicate that the absorption in the wavelength range of larger than 330 nm does not directly contribute significantly to the higher activity of the Pd-Bi/Ga_2O_3 sample.

Table 5 The results of reaction test of the NOCM over the Pd(0.18)-Bi(0.18)/Ga_2O_3 sample without and with the filter

Entry	Conditions	Production rates[a] / μmol h^{-1}		R^b (C_2H_6/H_2)
		C_2H_6	H_2	
1	no filter	0.95	1.1	0.86
2	filter ($\lambda_{transmission} \geq 330$ nm)	0.04	nd[c]	–[d]

[a]Production rates were measured after 5.5 h. [b]Calculated as follows: $R(C_2H_6/H_2)$ = (production rate of ethane)/(production rate of hydrogen). [c]nd: not detected. [d]The $R(C_2H_6/H_2)$ value could not be calculated. Reaction conditions were the same as those described in the footnote *a* of Table 1.

3.3.6.2 Reaction test with Bi_2O_3 and Pd/Bi_2O_3

On the other hand, the Bi_2O_3 sample (Figure 20a, black line) and the Pd/Bi_2O_3 sample (Figure 20b, blue line) also exhibited the absorption band in the wavelength range larger than 250 nm. However, no products were observed in the photocatalytic reaction tests over either of these samples meaning that the photoexcitation of these

species do not directly contribute to the activity of the Pd-Bi/Ga_2O_3 samples for the NOCM.

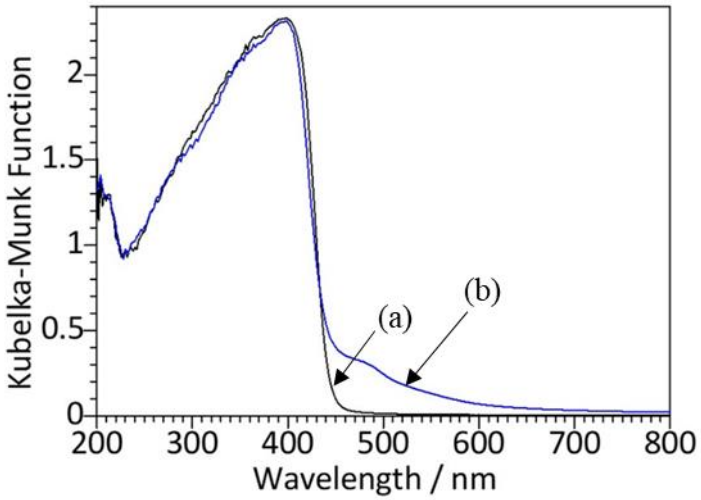

Figure 20 DR UV-vis spectra of (a) the Bi_2O_3 (black line) and (b) the Pd(0.18)/Bi_2O_3 (blue line) samples.

3.3.6.3 Reaction test with the physical mixtures

We prepared the four types of physical mixtures. First, we diluted the Pd(0.18)/Ga_2O_3 sample with Ga_2O_3 to study the effect of dilution. An equal weight of Ga_2O_3 powder is mixed with the powder of Pd(0.18)/Ga_2O_3 sample in a mortar for 10 min and then this physical mixture was pressed to make granules, which was represented as the DM sample (diluted mixture of Pd(0.18)/Ga_2O_3 with Ga_2O_3) for simplicity. The integration manner of the two components in the DM sample is shown in Figure 21a. Second, we filled equal weights of granules of the Pd(0.18)/Ga_2O_3 sample and the Bi(0.18)/Ga_2O_3 sample separated by quartz sand in the sample cell in the tandem sequence and represented it as the Pd+Q+Bi sample (granules of Pd/Ga_2O_3 and Bi/Ga_2O_3 separated by the quartz sand). The integration manner in the Pd+Q+Bi sample is shown in Figure 21b where the contact between the particles of Ga_2O_3 of the two components of Pd/Ga_2O_3 & Bi/Ga_2O_3 is inhibited. Third, we prepared an even mixture of equal weights of the granules of the Pd(0.18)/Ga_2O_3 and Bi(0.18)/Ga_2O_3 samples by shaking them in a bottle and then apparently homogeneous mixture of granules was inserted in the sample cell to be used for the reaction test as shown in Figure 21c. For simplicity, we represent it as the LCM sample (loosely contacted mixture) where there was a loose contact between the particles of Ga_2O_3 of the two components of Pd/Ga_2O_3

and Bi/Ga_2O_3. The Pd and Bi species were located on the different granules in the LCM sample. Finally, equal weights of the powders of the two photocatalysts Pd(0.18)/Ga_2O_3 and Bi(0.18)/Ga_2O_3 were physically mixed in a mortar for 10 min and this physical mixture was pressed to make granules. These granules were then filled in the sample cell as shown in Figure 21d. This is represented as the TCM sample (tightly contacted mixture) where there was a tight contact between the two components of the Pd/Ga_2O_3 and Bi/Ga_2O_3. The Pd and Bi species were located on the same granule but on the different particles of Ga_2O_3 in the TCM sample.

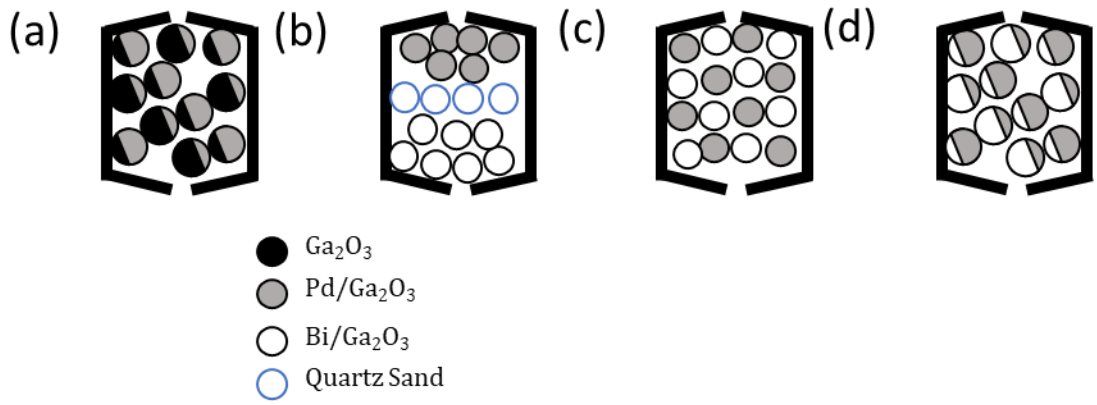

Figure 21 The integration manner of the two components of Pd/Ga_2O_3 and Bi/Ga_2O_3 in the samples, (a) DM, (b)Pd+Q+Bi, (c) LCM, and (d) TCM. The circles represent granules of the photocatalyst samples and particles of the quartz sand.

We tested these mixtures to investigate the role of dual cocatalyst species in the Pd-Bi/Ga_2O_3 photocatalyst for NOCM and the results are shown in Figure 22. The production rates as well as the selectivity over the DM sample (Figure 22d) were nearly the same as those over the undiluted Pd(0.18)/Ga_2O_3 sample (Figure 22c), indicating that the performance of the DM sample still remained similar although the content of Pd is reduced to 0.09 mol % in the sample cell after dilution and the bare Ga_2O_3 was less active. Moreover, the activity of the DM sample (Figure 22d) was higher than the average of those over the Ga_2O_3 sample (Figure 22a) and the Pd(0.18)/Ga_2O_3 sample (Figure 22c). We also confirmed in separate experiments that there is no effect of grinding the photocatalyst powder before making the granules on the activity and the selectivity. These results suggest that an interparticle electron transfer might take place between the particles of Ga_2O_3 in the DM sample; The number of the Ga_2O_3 particles and thus the photoexcited electrons generated in the Ga_2O_3 particles in the DM sample

should be the same as that in the Pd/Ga_2O_3 sample. However, if the electron transfers between these Ga_2O_3 particles are not allowed, the photocatalytic performance of the DM sample should be similar to the average of the Ga_2O_3 sample (Figure 22a) and the Pd(0.18)/Ga_2O_3 sample (Figure 22c). In the DM sample, the photoexcited electrons should migrate to the Pd/Ga_2O_3 particle and contribute to the reduction reaction. Thus, the present results evidenced the electron transfer between the Ga_2O_3 particles. An interparticle electron transfer has also been reported in the literature.[25,26]

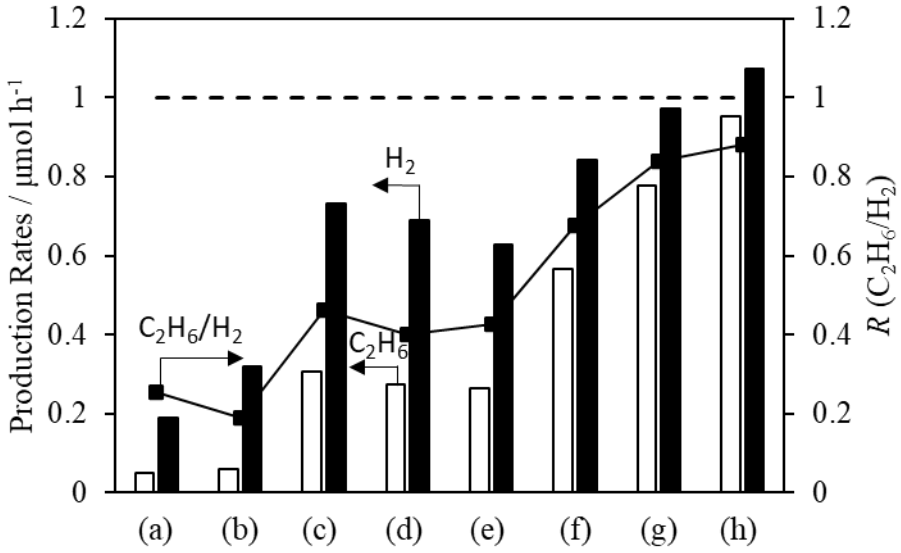

Figure 22 Production rates of ethane (white bars), hydrogen (black bars), and their ratio, *R* (black line with markers) with the samples, (a) bare Ga_2O_3, (b) Bi(0.18)/Ga_2O_3, (c) Pd(0.18)/Ga_2O_3, (d) DM, (e) Pd+Q+Bi, (f) LCM, (g) TCM, and (h) Pd(0.18)-Bi(0.18)/Ga_2O_3. The reaction tests were done three times in each case and the average values are shown here. The black dashed line represents the ideal value to *R* =1. The reaction conditions were same as those described in the footnote *a* of Table 1.

We also did some adiitional experiments to confirm the effect of irradiation area on the production rates over the Pd(0.18)/Ga_2O_3 and Bi(0.18)/Ga_2O_3 samples and the results are shown in Figure 23. When the irradiation area was reduced to half by filling a half of the sample cell with quartz sand (Q) for either the Pd(0.18)/Ga_2O_3 sample (Figure 23b, Pd+Q) or the Bi(0.18)/Ga_2O_3 sample (Figure 23d, Q+Bi), the production rates of ethane and hydrogen became nearly half compared to the fully filling cases shown in Figure 23a and 23e, respectively. Thus, it was confirmed that the production rates are proportional to the irradiation area.

The production rates of ethane and hydrogen with the Pd+Q+Bi sample (Figure 23c and also Figure 22e) were nearly equal to the sum of those over the Pd(0.18)/Ga_2O_3 sample of a half area (Figure 23b, Pd+Q) and the Bi(0.18)/Ga_2O_3 sample of a half area (Figure 23d, Q+Bi), which is quite reasonable.

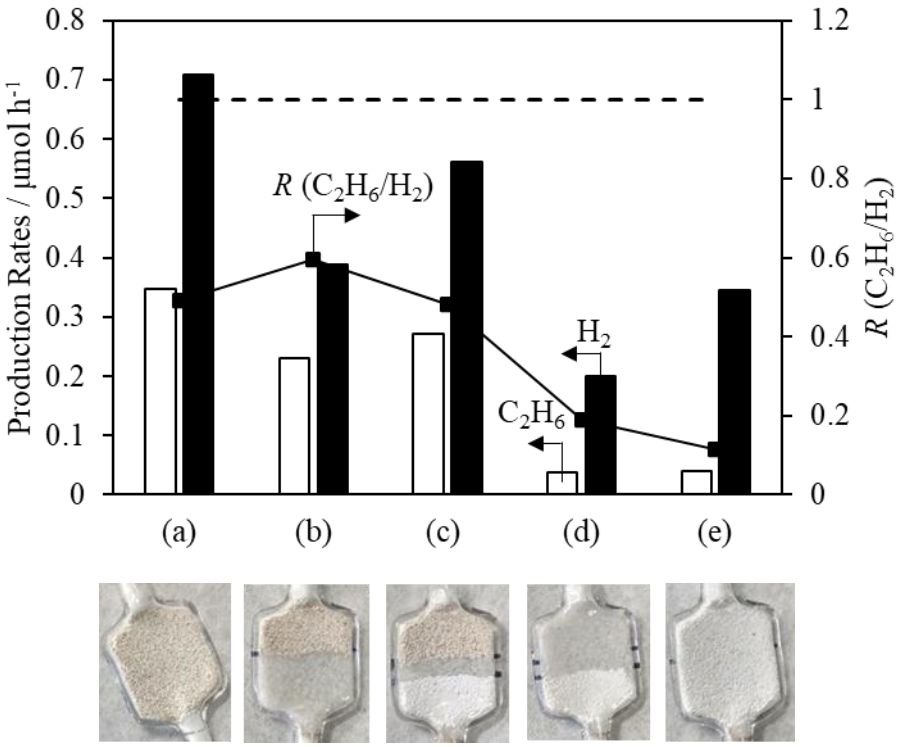

Figure 23 The production rates of ethane (red bars), hydrogen (blue bars), and their ratio, *R* (black line with markers) with the samples, (a) Pd(0.18)/Ga_2O_3, (b) Pd+Q , (c) Pd+Q+Bi, (d) Q+Bi, and (e) Bi(0.18)/Ga_2O_3 and the photographs of their respective sample cells. Q = Quartz sand. The black dashed line represents the ideal value to *R* =1. The reaction conditions were same as those described in the footnote *a* of Table 1.

The LCM sample, which consisted of the Pd(0.18)/Ga_2O_3 and Bi(0.18)/Ga_2O_3 granules with the content of Pd and Bi being 0.09 mol % each was used for the reaction test. The activity as well as the selectivity increased over the LCM sample (Figure 22f) in comparison to those over the Pd+Q+Bi sample (Figure 22e), meaning that the loose contact of the Pd/Ga_2O_3 and Bi/Ga_2O_3 granules is more favorable for the NOCM compared to the state separated by the quartz layer. In this LCM sample, the Pd and Bi species are located on different Ga_2O_3 granules. Both ethane and hydrogen were produced continuously from methane upon photoirradiation at least for 30 h over the LCM sample as shown in Figure 24. The contact of the granules would facilitate an

interparticle transfer in the LCM sample, which might be the transfer of not only the electron but also radical intermediate species.

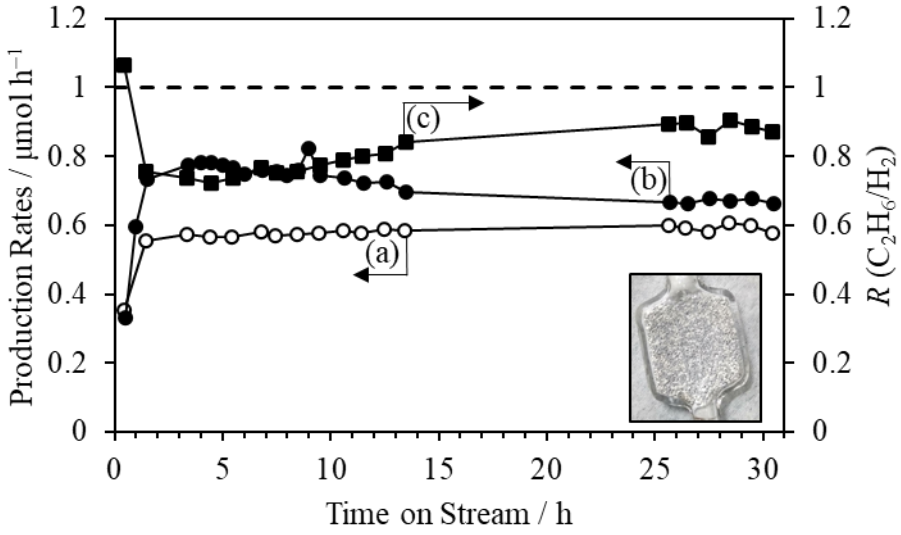

Figure 24 Time course of (a) ethane, (b) hydrogen, and (c) their ratio, *R* in the photocatalytic reaction test of the NOCM over the LCM sample. Reaction conditions were same as those described in the footnote *a* of Table 1. Inset: Photograph of the sample cell filled with the LCM sample after the reaction test. The separate granules can be seen easily and can be distinguished by their different colors.

Lastly, the TCM sample was used for the reaction test. A tight contact can be formed by the powder mixing, followed by the subsequent pressing the powder to form the granule[27] in the LCM sample where the content of Pd and Bi was 0.09 mol % each in the sample cell. The Pd and Bi species were present in the same granules but on the different Ga_2O_3 particles in the granules. As we can see, the activity as well as the selectivity was further improved over the TCM sample (Figure 22g) in comparison to the LCM sample (Figure 22f). This means that the tight contact is better than the loose contact and it improved the interparticle transfer which should be responsible for the enhanced activity and selectivity over the TCM sample. These results suggest that the better performance over the mixture system than those over Pd(0.18)/Ga_2O_3 or Bi(0.18)/Ga_2O_3 might be because of an interparticle radical transfer (i.e; transfer of a methyl radical from one particle of Ga_2O_3 to another). Further, although the transfer of methyl radical can take place in two ways, either gaseous phase transfer or the surface transfer, the collision probability for the radical coupling would be high on the surface.

The activity as well as the selectivity over the co-impregnated sample Pd(0.18)-Bi(0.18)/Ga_2O_3 (Figure 22h) was only slightly higher than the TCM sample (Figure 22g), i.e., the difference was not so large. Although we could not rule out the possibility of formation of Pd-Bi mixed species (such as intermetallic or alloy nanoparticles) on Ga_2O_3 particle in the Pd-Bi/Ga_2O_3 sample prepared by the co-impregnation method, these results suggest that the independently deposited Pd and Bi particles can give high activity and selectivity towards photocatalytic NOCM and the contribution from the such possible species (directly interacted Pd-Bi species, intermetallic compound, or alloy species) might be small. The distance between the independently deposited Pd and Bi nanoparticles would also be closer on the Pd(0.18)-Bi(0.18)/Ga_2O_3 sample than that on the TCM sample, which would be an advantage of the Pd(0.18)-Bi(0.18)/Ga_2O_3 sample.

According to our results, the Pd(0.18)/Ga_2O_3 photocatalyst showed a non-equimolar production of ethane and hydrogen. Since no other products (such as ethene and propane) could be detected by the GC, we assume that the decomposition to form coke (eq. 2) took place as a side reaction over the Pd(0.18)/Ga_2O_3 photocatalyst. On some Pd-Bi/Ga_2O_3 photocatalysts, the two products, ethane and hydrogen, were produced in the equimolar ratio. It suggests that the addition of bismuth helps in suppresing or inhibiting coke formation and promoting NOCM selectively. Coke formation might occur from the deep dehydrogenation of methyl radicals by the photogenerated holes (eq. 5). It is important for the high NOCM selectivity to enhance the coupling of the methyl radical before the further oxidations by the holes. Now, we consider that Bi species on the Ga_2O_3 surface are coupling sites of methyl radicals to form ethane and to reduce their decomposition giving coke formation. Thus, Bi species can promote the NOCM on the Pd-Bi/Ga_2O_3 photocatalysts.

$$^{\bullet}CH_3 + 3h^+ \rightarrow C + 3H^+ \quad (5)$$

Additional clear trend can be noticed in Figure 22 that the *R* value, as an indication of the reaction selectivity not to the MD but NOCM, increased with the increase of the production rates of ethane and hydrogen. We plotted the value of *R* against the production rates in Figure 25. With an increase in the activity of the photocatalyst, the value of *R* is also increased suggesting that the selectivity for the NOCM is also increased in a similar manner. The relationship suggests that the active photocatalyst can produce a large number of methyl radicals and provide high surface concentration of the methyl radicals, which gives high coupling rate of the methyl

radicals. Thus, the high photocatalytic activity is also important factor to increase the NOCM selectivity.

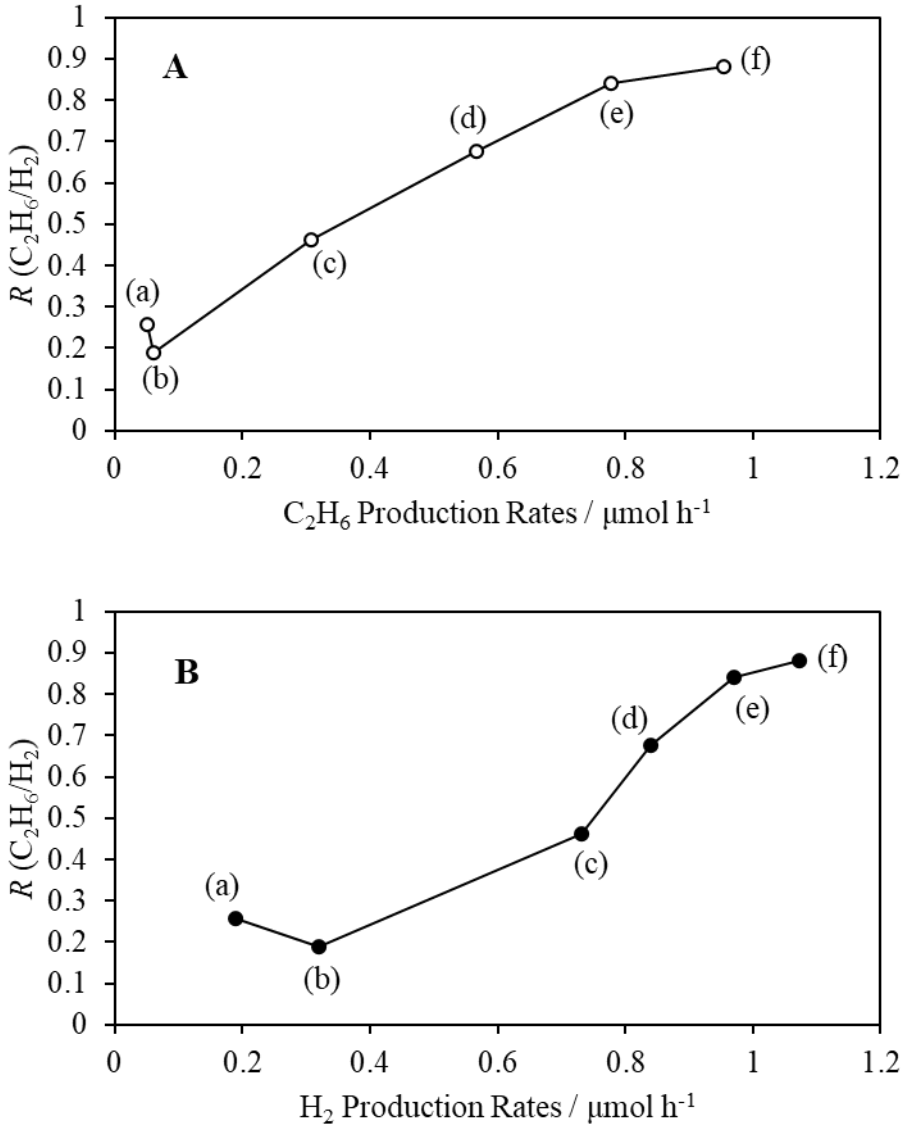

Figure 25 The relationship between (A) the *R* value and the ethane production rates and (B) the *R* value and the hydrogen production rates over the samples. The data were obtained with the samples, (a) Ga_2O_3, (b) Bi(0.18)/Ga_2O_3, (c) Pd(0.18)/Ga_2O_3, (d) LCM, (e) TCM, and (f) Pd(0.18)-Bi(0.18)/Ga_2O_3.

3.3.7 Tentative mechanism of NOCM with the Pd-Bi/Ga_2O_3 photocatalyst

Roles of the Pd and Bi species and a proposed mechanism of complete NOCM over the Pd-Bi/Ga_2O_3 photocatalyst is shown in Scheme 1.

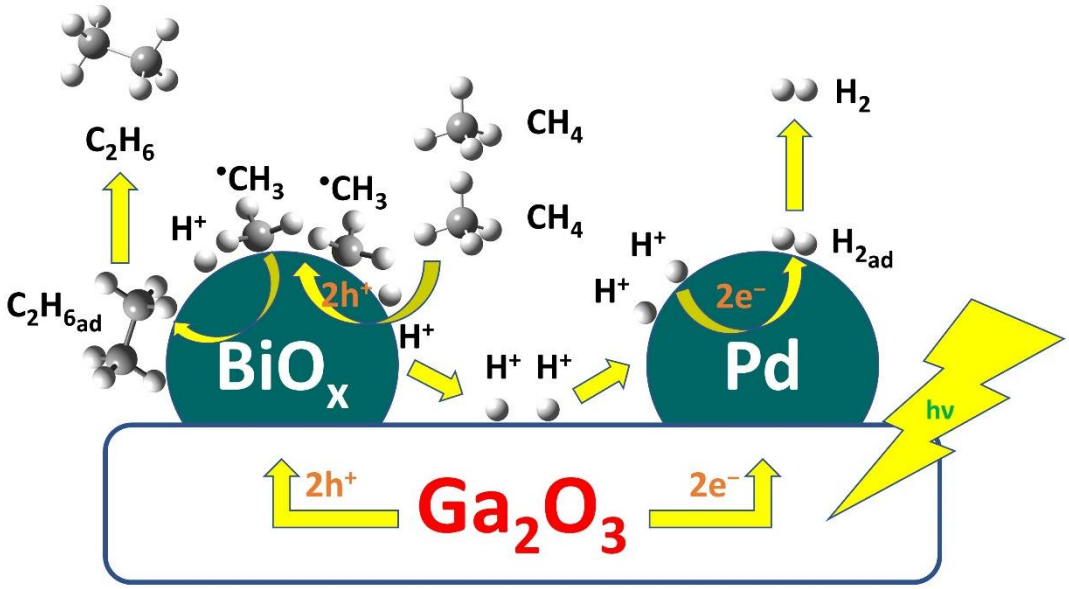

Scheme 1 Roles of the Pd and Bi species and a proposed mechanism of the NOCM over the Pd-Bi/Ga_2O_3 photocatalyst. C_2H_{6ad} = adsorbed ethane, H_{2ad} = adsorbed hydrogen.

The Ga_2O_3 particles function as the semiconductor photocatalyst, which can absorb the photons upon UV light irradiation generating electrons and holes at its conduction band (CB) and valence band (VB), respectively. The photogenerated electrons are subsequently transferred to the Pd nanoparticle from the CB of the Ga_2O_3 particle. Then the adsorbed CH_4 molecules are oxidized to generate methyl radicals and proton (Eq. 6) by the photogenerated holes at the VB of the Ga_2O_3 particle. The coupling of the methyl radicals can be promoted by the Bi species on the Ga_2O_3 particle surface to form ethane (Eq. 7). It is also possible to consider that the Bi species can receive holes to oxidize methane and the methyl radical coupling can take place on the surface of the Bi species. The two protons produced at the oxidation sites would be transferred to the Pd species and reduced by the photogenerated electrons on the Pd nanoparticles to form hydrogen (Eq. 8). Thus, the closed location of the Pd and Bi species on the Ga_2O_3 particles would be advantageous for the efficient migration of the protons.

$$2\ CH_4 + 2\ h^+ \rightarrow 2\ {}^{\bullet}CH_3 + 2\ H^+ \quad (6)$$

$$2\ {}^{\bullet}CH_3 \rightarrow C_2H_6 \quad (7)$$

$$2\ H^+ + 2\ e^- \rightarrow H_2 \quad (8)$$

Although the selectivity for the NOCM is enhanced upon loading of the Pd and Bi dual-cocatalysts in the Pd-Bi/Ga_2O_3 sample, a low ethane selectivity was shown with the Bi/Ga_2O_3 sample alone. Due to the low activity of the Bi/Ga_2O_3 sample, a low

concentration of methyl radicals would be generated from methane by the photogenerated holes (eq. 6) and the probability of effective collision of the methyl radicals to form ethane (eq. 7) would also be less in this state. Thus, the holes might cause further dehydrogenation of these methyl radicals to coke (eq. 5) decreasing the ethane selectivity in the Bi/Ga_2O_3 sample. On the other hand, a higher activity and thus, a higher selectivity for the NOCM is reflected in the $Pd\text{-}Bi/Ga_2O_3$ sample.

3.4 Conclusions

A dual cocatalyst modified semiconductor photocatalyst approach was explored for non-oxidative coupling of methane (NOCM) reaction, and a palladium bismuth dual-cocatalyst-loaded gallium oxide ($Pd\text{-}Bi/Ga_2O_3$) photocatalyst exhibited selective NOCM with excellent stability (100 h) and recyclability. The optimized $Pd(0.18)\text{-}Bi(0.05)/Ga_2O_3$ photocatalyst showed the best performance for the NOCM with higher production rates of ethane and hydrogen such as 1.10 and 1.24 μmol h^{-1}, respectively at 5.5 h later in the present conditions. The apparent quantum efficiency (AQE) measured in the wavelength range of 220-300 nm was 0.2 % with the $Pd(0.18)\text{-}Bi(0.05)/Ga_2O_3$ photocatalyst. A pretreatment in the flow of hydrogen further increased the activity of the $Pd\text{-}Bi/Ga_2O_3$ sample by two times with unchanged high selectivity for the NOCM.

The location of Bi species in the vicinity of Pd species was beneficial for improving the activity and selectivity of the $Pd\text{-}Bi/Ga_2O_3$ sample for the NOCM by suppressing the decomposition of methane to coke. A possibility of an interparticle transfer involving a charge transfer and a methyl radical transfer is also discussed. This study presents a new strategy by using a dual cocatalyst for the design of active photocatalysts in the application of selective NOCM. A mixture of separately prepared multiple photocatalysts with various single cocatalyst is also efficient for the use, meaning that this mixing strategy can avoid a possible disadvantage of the co-loading multiple cocatalyst on the same photocatalyst particles.

Further, it was also clearly demonstrated that the photocatalytic production rates are not proportional to the weight of the catalyst while the production rates depend on the irradiation area in the employed flow reactor.

Although we successfully improved the photocatalytic performance of the Ga_2O_3 photocatalyst with the dual cocatalyst for the NOCM in the present study, the

photocatalytic performance is still not enough for the practical use. Further investigations and developments are required.

Acknowledgement

The XAFS measurements were performed at the BL01B1 of SPring-8 with the approval of the Japan Synchrotron Radiation Research Institute (JASRI) (Proposal no. 2020A1316). This work was financially supported by ISHIZUE 2020 of the Kyoto University Research Development Program, a Grant-in-Aid for Scientific Research (B) (21H01975), a Grant-in-Aid for Challenging Research (Exploratory, 20K21108) and a Grant-in-Aid for Young Scientists (19K15359) from the Japan Society for the Promotion of Science (JSPS), and the Program for Element Strategy Initiative for Catalysts & Batteries (ESICB, JPMXP0112101003), commissioned by the MEXT of Japan. S.P.S. thanks the JICA for providing a scholarship under the FRIENDSHIP project to pursue his Ph.D. in Japan.

References

(1) Choudhary, T. V.; Aksoylu, E.; Goodman, D. W. Nonoxidative Activation of Methane. *Catal. Rev. - Sci. Eng.* **2003**, *45* (1), 151–203.

(2) Yuliati, L.; Yoshida, H. Photocatalytic Conversion of Methane. *Chem. Soc. Rev.* **2008**, *37* (8), 1592–1602.

(3) Singh, S. P.; Anzai, A.; Kawaharasaki, S.; Yamamoto, A.; Yoshida, H. Non-Oxidative Coupling of Methane over Pd-Loaded Gallium Oxide Photocatalysts in a Flow Reactor. *Catal. Today* **2021**, *375* (April 2020), 264–272.

(4) Lang, J.; Ma, Y.; Wu, X.; Jiang, Y.; Hu, Y. H. Highly Efficient Light-Driven Methane Coupling under Ambient Conditions Based on an Integrated Design of a Photocatalytic System. *Green Chem.* **2020**, *22* (14), 4669–4675.

(5) Yoshida, H.; Kato, S.; Hirao, K.; Nishimoto, J. I.; Hattori, T. Photocatalytic Steam Reforming of Methane over Platinum-Loaded Semiconductors for Hydrogen Production. *Chem. Lett.* **2007**, *36* (3), 430–431.

(6) Yoshida, H.; Hirao, K.; Nishimoto, J.-I.; Shimura, K.; Kato, S.; Itoh, H.; Hattori, T. Hydrogen Production from Methane and Water on Platinum Loaded Titanium Oxide Photocatalysts. *J. Phys. Chem. C* **2008**, *112* (14), 5542–5551.

(7) Shimura, K.; Kato, S.; Yoshida, T.; Itoh, H.; Hattori, T.; Yoshida, H.

Photocatalytic Steam Reforming of Methane over Sodium Tantalate. *J. Phys. Chem. C* **2010**, *114* (8), 3493–3503.

(8) Yamamoto, A.; Mizuba, S.; Saeki, Y.; Yoshida, H. Platinum Loaded Sodium Tantalate Photocatalysts Prepared by a Flux Method for Photocatalytic Steam Reforming of Methane. *Appl. Catal. A Gen.* **2016**, *521*, 125–132.

(9) Ishimaru, M.; Amano, F.; Akamoto, C.; Yamazoe, S. Methane Coupling and Hydrogen Evolution Induced by Palladium-Loaded Gallium Oxide Photocatalysts in the Presence of Water Vapor. *J. Catal.* **2021**, *397*, 192–200.

(10) Xiao, Y.; Varma, A. Highly Selective Nonoxidative Coupling of Methane over Pt-Bi Bimetallic Catalysts. *ACS Catal.* **2018**, *8* (4), 2735–2740.

(11) Dipu, A. L.; Ohbuchi, S.; Nishikawa, Y.; Iguchi, S.; Ogihara, H.; Yamanaka, I. Direct Nonoxidative Conversion of Methane to Higher Hydrocarbons over Silica-Supported Nickel Phosphide Catalyst. *ACS Catal.* **2020**, *10* (1), 375–379.

(12) Yoshida, H.; Kato, Y.; Hattori, T. Photoinduced Non-Oxidative Methane Coupling over Silica-Alumina. *Stud. Surf. Sci. Catal.* **2000**, *130 A*, 659–664.

(13) Yoshida, H.; Matsushita, N.; Kato, Y.; Hattori, T. Active Sites in Sol-Gel Prepared Silica-Alumina for Photoinduced Non-Oxidative Methane Coupling. *Phys. Chem. Chem. Phys.* **2002**, *4* (11), 2459–2465.

(14) Li, L.; Li, G. D.; Yan, C.; Mu, X. Y.; Pan, X. L.; Zou, X. X.; Wang, K. X.; Chen, J. S. Efficient Sunlight-Driven Dehydrogenative Coupling of Methane to Ethane over a Zn+-Modified Zeolite. *Angew. Chemie - Int. Ed.* **2011**, *50* (36), 8299–8303.

(15) Meng, L.; Chen, Z.; Ma, Z.; He, S.; Hou, Y.; Li, H. H.; Yuan, R.; Huang, X. H.; Wang, X.; Wang, X.; Long, J. Gold Plasmon-Induced Photocatalytic Dehydrogenative Coupling of Methane to Ethane on Polar Oxide Surfaces. *Energy Environ. Sci.* **2018**, *11* (2), 294–298.

(16) Wu, S.; Tan, X.; Lei, J.; Chen, H.; Wang, L.; Zhang, J. Ga-Doped and Pt-Loaded Porous TiO_2-SiO_2 for Photocatalytic Nonoxidative Coupling of Methane. *J. Am. Chem. Soc.* **2019**, *141* (16), 6592–6600.

(17) Chen, Z.; Wu, S.; Ma, J.; Mine, S.; Toyao, T.; Matsuoka, M.; Wang, L.; Zhang, J. N-type Doping Induced Electron Localization for Non-oxidative Coupling of Methane. *Angew. Chemie Int. Ed.* **2021**, 60, 11901-11909.

(18) Geller, S. Crystal Structure of β-Ga_2O_3 Cite. *J. Chem. Phys* **1960**, *33* (4), 676.

(19) Marezuo, M.; Remeika, J. P. Bond Lengths in the α-Ga_2O_3 Structure and the High-Pressure Phase Of. *J. Chem. Phys.* **1967**, *46* (5), 1862–1865.

(20) Zinkevich, M.; Morales, F. M.; Nitsche, H.; Ahrens, M.; Rühle, M.; Aldinger, F. Microstructural and Thermodynamic Study of γ-Ga_2O_3. *Zeitschrift fuer Met.* **2004**, *95* (9), 756–762.

(21) Iguchi, S.; Hasegawa, Y.; Teramura, K.; Kidera, S.; Kikkawa, S.; Hosokawa, S.; Asakura, H.; Tanaka, T. Drastic Improvement in the Photocatalytic Activity of Ga_2O_3 Modified with Mg-Al Layered Double Hydroxide for the Conversion of CO_2 in Water. *Sustain. Energy Fuels* **2017**, *1* (8), 1740–1747.

(22) Hou, Y.; Wu, L.; Wang, X.; Ding, Z.; Li, Z.; Fu, X. Photocatalytic Performance of α-, β-, and γ-Ga_2O_3 for the Destruction of Volatile Aromatic Pollutants in Air. *J. Catal.* **2007**, *250* (1), 12–18.

(23) Barrera, A.; Tzompantzi, F.; Padilla, J. M.; Casillas, J. E.; Jácome-Acatitla, G.; Cano, M. E.; Gómez, R. Reusable PdO/Al_2O_3-Nd_2O_3 Photocatalysts in the UV Photodegradation of Phenol. *Appl. Catal. B Environ.* **2014**, *144*, 362–368.

(24) Shimura, K.; Yoshida, T.; Yoshida, H. Photocatalytic Activation of Water and Methane over Modified Gallium Oxide for Hydrogen Production. *J. Phys. Chem. C* **2010**, *114* (26), 11466–11474.

(25) Sasaki, Y.; Nemoto, H.; Saito, K.; Kudo, A. Solar Water Splitting Using Powdered Photocatalysts Driven by Z-Schematic Interparticle Electron Transfer without an Electron Mediator. *J. Phys. Chem. C* **2009**, *113* (40), 17536–17542.

(26) Yoshino, S.; Sato, K.; Yamaguchi, Y.; Iwase, A.; Kudo, A. Z-Schematic CO_2 Reduction to CO through Interparticle Electron Transfer between $SrTiO_3$:Rh of a Reducing Photocatalyst and $BiVO_4$ of a Water Oxidation Photocatalyst under Visible Light. *ACS Appl. Energy Mater.* **2020**, *3* (10), 10001–10007.

(27) Cheng, K.; Gu, B.; Liu, X.; Kang, J.; Zhang, Q.; Wang, Y. Direct and Highly Selective Conversion of Synthesis Gas into Lower Olefins: Design of a Bifunctional Catalyst Combining Methanol Synthesis and Carbon-Carbon Coupling. *Angew. Chemie* **2016**, *128* (15), 4803–4806.

4 Nonoxidative coupling of ethane with gold loaded photocatalysts

Abstract

Direct and continuous conversion of ethane to yield *n*-butane and hydrogen at near room temperature (*ca.* 320 K) was examined with gold loaded gallium oxide and titanium dioxide photocatalysts without the aid of any oxidant in a flow reactor. A Ga_2O_3 photocatalyst produced *n*-butane and ethene as well as hydrogen in almost stoichiometric ratio from ethane. Loading Au on the Ga_2O_3 sample gave 12 times higher production rate of *n*-butane such as 0.65 μmol h^{-1} with a high selectivity of 89 %. Although a bare TiO_2 sample showed very low yield due to poor reduction resistance, the addition of Au cocatalyst drastically improved the photocatalytic performance of the TiO_2 sample and an Au(0.2)/TiO_2 sample produced *n*-butane and ethene continuously at least for 5.5 h, where the production rate of *n*-butane, the *n*-butane selectivity, and the apparent quantum efficiency (AQE) for *n*-butane formation were 0.92 μmol h^{-1}, 92%, and 0.02 %, respectively. The reaction mechanism of *n*-butane formation as a main reaction was proposed to be photocatalytic non-oxidative coupling of ethane (NOCE), which is similar to the photocatalytic nonoxidative coupling of methane (NOCM).

4.1 Introduction

Ethane is one of the main components of natural gas second only to methane.[1] Utilization of natural gas as a carbon source is of utmost importance and thus it is required to develop the conversion processes of not only methane but also ethane to the value-added chemicals. However, most of the processes to convert ethane are thermodynamically not feasible at room temperature due to the positive Gibbs energy change except for combustion or partial oxidation with oxygen.[2] Traditionally, ethane conversion has been studied in both the homogenous and the heterogeneous catalytic systems. Homogeneous conversion and functionalization of ethane involve harsh reaction conditions such as strong electrophiles, super acids, strong oxidants and require noble metals such as iridium, rhodium and ruthenium complexes.[3,4] On the other hand, heterogenous catalysis including oxidative coupling, aromatization, and CO_2 reforming of ethane requires high operating temperatures and thus suffers from high energy input and high cost.[5,6]

Alternatively, photocatalysis is a green technology to convert ethane via C–H bond activation to various chemicals under milder conditions.[2] A decomposition of ethane photosensitized by Hg ($^3P_1$) atoms at higher temperatures (673–773 K) to yield ethene and hydrogen as the major products can be considered the first report.[7] After that, various photocatalytic and photoinduced processes including homogeneous,[8] heterogeneous,[9–15] and supercritical ethane conversion[16] have been developed. Among them, the heterogenous photocatalytic pathway has been widely studied for ethane conversion with various oxidants such as O_2, CO_2, and NO to yield a variety of products ranging from CO,[9] CO_2,[10] C_2H_4,[11] formaldehyde,[12] acetaldehyde[12] to ethanol,[13] and so on.[14,15] However, much less effort has been devoted for the direct conversion of ethane into higher hydrocarbons like butane without aid of any oxidant.

In our studies of the photocatalytic non-oxidative coupling of methane (NOCM) for more than two decades,[17] ethane and hydrogen were obtained selectively as the main products with various photocatalysts such as the quantum photocatalysts[18] like Al_2O_3,[19,20] SiO_2–Al_2O_3,[19,20] SiO_2–Al_2O_3–TiO_2,[21,22] and Ce/SiO_2,[23] and also the semiconductor photocatalysts like Ga_2O_3,[24] Pd/Ga_2O_3 (also see Chapter 2),[25] and Pd–Bi/Ga_2O_3 (also see Chapter 3).[26] Particularly, the Pd–Bi/Ga_2O_3 photocatalyst showed the excellent stability with continuous production of ethane and hydrogen selectively for 100 h with high formation rates.[26] Recently, GaN and ZnO solid solution thin films showed good activity for the NOCM with high selectivity.[27] An Au/TiO_2 photocatalyst with light-diffuse-reflection-surfaces also promoted

the NOCM selectively.[28] Thus, in the present study we tested whether or not the photocatalysts for the NOCM can efficiently convert ethane under non-oxidative conditions in a flow reactor. Among the examined several samples, the Au loaded Ga_2O_3 and TiO_2 photocatalysts showed the high activity to form *n*-butane in the non-oxidative direct ethane conversion under photoirradiation in the mild conditions, nearly room temperature and atmospheric pressure.

4.2 Experimental

4.2.1 Materials and Sample Preparation

The following chemicals employed in the present study were either obtained commercially or donated by the Catalysis Society of Japan: Ga_2O_3 (99.90%, Kojundo Chemicals, the same reagent used in the previous work),[26] a mixture of rutile and anatase TiO_2 (P-25, 49 $m^2\ g^{-1}$, Nippon Aerosil Co. Ltd.), and Al_2O_3 (JRC-ALO-7, γ-phase, 170 $m^2\ g^{-1}$, the Catalysis Society of Japan).

A Pd standard solution (5 mg mL^{-1} $Pd(NO_3)_2$ in 6.6 mol L^{-1} HNO_3(aq), Wako Chemicals) and a Bi standard solution (1 g L^{-1} $Bi(NO_3)_3$ in 0.5 mol L^{-1} HNO_3(aq), Wako Chemicals) were used as the precursors of Pd and Bi elements, respectively in the preparation of the Pd/Ga_2O_3 sample and the $Pd–Bi/Ga_2O_3$ sample by an impregnation and a co-impregnation method, respectively. The procedures of the preparation of Pd/Ga_2O_3 sample and the $Pd–Bi/Ga_2O_3$ sample were the same as described in our previous study (also see Chapter 3).[26] The loading amount of Pd and Pd–Bi cocatalyst was 0.18 mol% for each element, which is also the typical value in the previous study (also see Chapter 3).[26]

$HAuCl_4{\cdot}4H_2O$ was used as a precursor of the Au element. The Au loaded photocatalyst samples were prepared by a photodeposition method. A typical procedure for the preparation of an Au/TiO_2 sample is as follows. 1.2 g of TiO_2 (white powder) was dispersed in 48 mL of deionized water and this suspension was photoirradiated for 0.5 h. Then 12 mL of methanol and the required amount of the precursor of Au were added to this suspension and it was stirred for 1 h in dark. The suspension was then photoirradiated from a ceramic xenon lamp (PE300BUV, 300 W) for 0.5 h. The powder was then filtered, washed with water and ethanol, and dried in an electric oven at 373 K overnight. A purple-colored powder of Au/TiO_2 sample was obtained. A similar procedure was followed to prepare other Au loaded samples by the phtodeposition method. The prepared samples were referred to as Au(*x*)/catalyst, where *x* in mol% gives the loading amount of Au.

4.2.2 Characterization

The obtained samples were characterized by several techniques. The crystal structure was determined by powder X-ray diffraction (XRD) with a Shimadzu LabX XRD-6000 X-ray diffractometer using Cu Kα radiation (40 kV, 30 mA). A Hitachi SU8220 model scanning electron microscope (SEM) in conjunction with a Horiba EX-370 energy dispersive X-ray (EDX) analyser was used to record the SEM images and EDX elemental mappings. Transmission electron microscope (TEM) and scanning transmission electron microscope (STEM) images were recorded in a high-angle annular dark field (HAADF) mode with a JEOL model JEM-2000FC field emission electron microscope. Diffuse reflectance UV-visible (DR UV-vis) spectra were recorded by a JASCO V-570 UV/VIS/NIR spectrophotometer equipped with an integrating sphere covered with a $BaSO_4$ reference. The loading of Au was determined by the X-ray fluorescence (XRF) analysis using a Shimadzu EDX-8000 energy dispersive X-ray fluorescence spectrometer. A calibration curve was made for XRF analysis with the Au/TiO_2 samples prepared by an impregnation method followed by calcination (673 K, 2 h) and it was used to determine the actual loading amount of Au in the Au/TiO_2 samples prepared by the photodeposition method in the present study. Au L_{III}-edge X-ray absorption fine structures (XAFS) of the Au/TiO_2 samples were measured in a fluorescence mode using a 19-element Ge solid state detector (SSD) at the BL12C beamline of synchrotron radiation facility Photon Factory, IMSS, KEK, Japan. The spectral output of the Xe-lamp (PE300BUV, 300W) was measured by a USB fiber optic spectrometer (USB2000 model, Ocean Optics).

4.2.3 Experimental set-up

The photocatalytic activity tests for the direct ethane conversion were carried out using a flow reactor similar to our previous works[25,26] as shown in Figure 1. The catalyst powder was pressed under 40 MPa pressure and ground into granules of 310–710 μm (25–50 mesh). The sample granules were filled into a quartz cell ($2 \times 2 \times 0.1$ cm^3, see the photograph in the inset of Figure 1). The weights of the granules used for filling the cell were 0.8, 0.6, and 0.4 g for the bare and cocatalysts loaded Ga_2O_3, TiO_2, and Al_2O_3 samples, respectively. The sample was pretreated with an argon flow for 30 min (flow rate 27 mL min^{-1}) to exclude the air from the quartz cell. A flow of mixture of 10% ethane in argon (total flow rate 30 mL min^{-1}) was introduced to the cell for 1 h in dark to achieve stable conditions, where the contact time was nearly 0.8 s and space velocity (SV) was 4500 h^{-1}. The sample was then photoirradiated from a ceramic xenon lamp (PE300BUV, 300 W, Figure 2) to start the reaction. The irradiation area was 4 cm^2 and the light intensity measured by a UV radiometer (Topcon, UD 250 detector) in

the wavelength range of 220–300 nm with the highest sensitivity at 254 nm was *ca.* 20 mW cm^{-2}. During the photocatalytic reaction test, the temperature of the surface of the sample cell measured by an infrared thermometer (Testo, 835-T1) was increased to *ca.* 320 K by photoirradiation. The outlet gases were analyzed by two on-line gas chromatographs: one equipped with a TCD (Shimadzu, GC-8A, argon carrier, a Molecular Sieves 5A, column temperature 333 K) and another with an FID (Shimadzu, GC-8A, argon carrier, a Gaskuropack 54, column temperature 363 K). The detectable gases by the GC-TCD were hydrogen, oxygen, nitrogen, methane, ethene, ethane and carbon monoxide while the detectable gases by the GC-FID were methane, ethene, ethane, propene, propane, *i*-butane, and *n*-butane in the detection range of retention times.

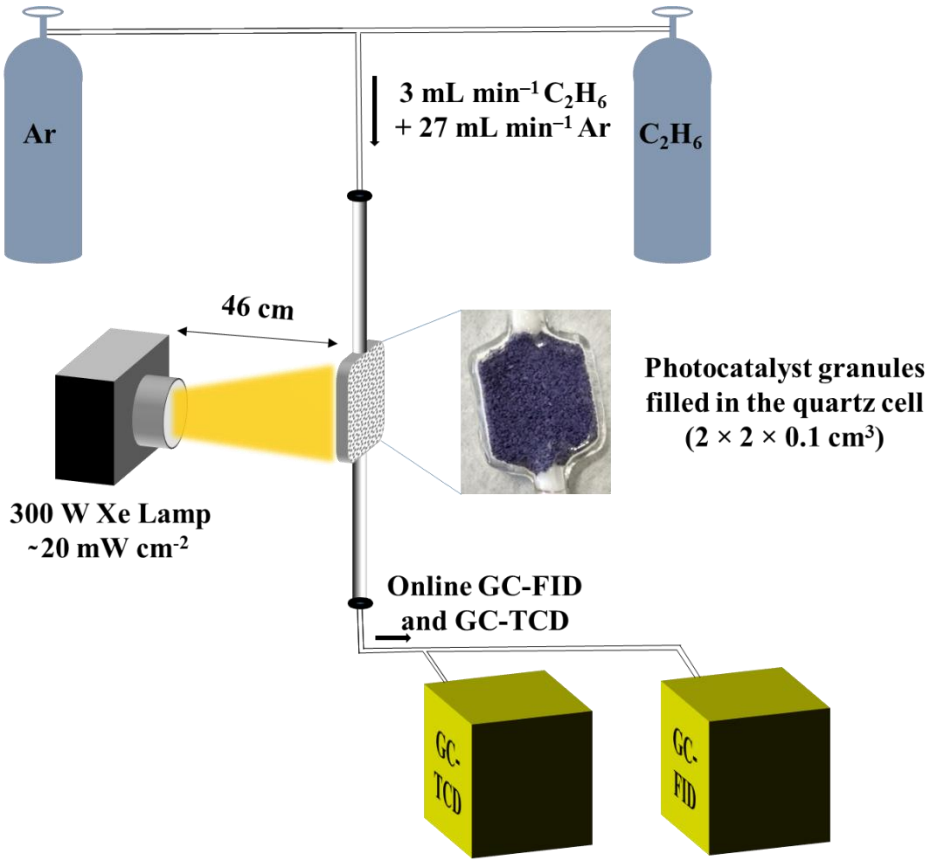

Figure 1 The schematic diagram of the experimental set-up used in the reaction test of photocatalytic ethane conversion, which is similar to our previous work. Inset: the photograph of the sample cell filled with the granules of the Au(0.4)/TiO_2 sample. The size of the sample cell was 2 cm × 2 cm × 0.1 cm.

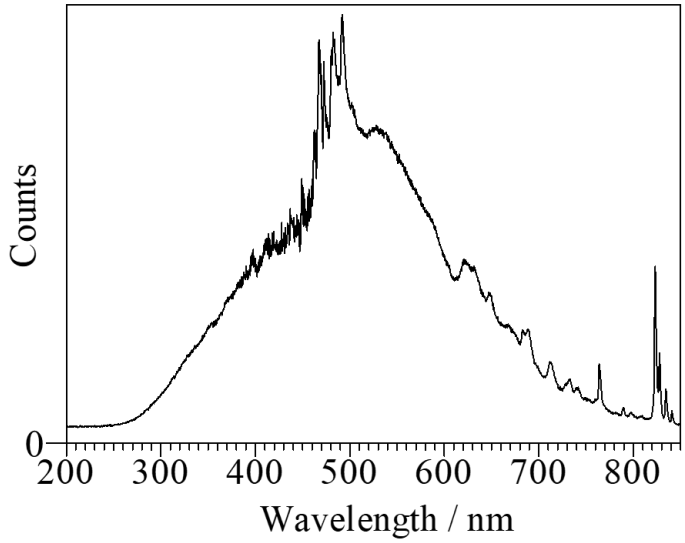

Figure 2 Spectral output of the Xe-lamp.[29,30] The lamp emits continuous light in the wavelength range of 200–800 nm with varying photon output.

4.2.4 Calculations

The yield of hydrocarbons (%) in the reaction is calculated based on eq. 6, 7 and 10 as shown in eq. 1.

$$Yield\ (\%) = \frac{Consumption\ rate\ of\ ethane\ (2\times R_{C4H10}+R_{C2H4}+R_{CH4})}{Introduction\ rate\ of\ ethane} \times 100 \quad (1)$$

The product selectivity (%) based on ethane toward *n*-butane and ethene are calculated as shown below in eq. 2 and 3, respectively.

$$S_{C4H10}\ (\%) = \frac{2\times R_{C4H10}}{2\times R_{C4H10}+R_{C2H4}+R_{CH4}} \times 100 \quad (2)$$

$$S_{C2H4}\ (\%) = \frac{R_{C2H4}}{2\times R_{C4H10}+R_{C2H4}+R_{CH4}} \times 100 \quad (3)$$

The ratio of the obtained hydrocarbons and hydrogen ($R_{HC/H2}$) is defined as follows (eq. 4).

$$R_{HC/H2} = \frac{R_{C4H10}+R_{C2H4}-R_{CH4}}{R_{H2}} \times 100 \quad (4)$$

where R_{C4H10}, R_{C2H4}, R_{CH4}, and R_{H2} are production rates of *n*-butane, ethene, methane, and hydrogen, respectively.

The apparent quantum efficiency (AQE) was calculated by the following equation as the ratio of the number of consumed holes for the butane formation (or ethene formation) and the number of incident photons as shown in eq. 5.

$$AQE\ (\%) = \frac{r \times n \times N}{(I \times A)/(hc/\lambda)} \times 100 \qquad (5)$$

where r = production rate of C_4H_{10} (or C_2H_4) (in mol s^{-1}), n = number of holes consumed for the production of C_4H_{10} (or C_2H_4) (n=2), N = Avogadro constant (in mol^{-1}), I = intensity of the incident light estimated in the wavelength range of 200–420 nm (from the measured value in the wavelength range of 220–300 nm by a UV radiometer and the DR UV-vis absorption spectrum) (in W cm^{-2}), A = Area of the reactor (in cm^2), h = Planck's constant (in J s), c = speed of light (in m s^{-1}), λ = wavelength of incident light (in m).

4.3 Results and Discussion

4.3.1 Reaction tests of the photocatalytic direct ethane conversion

Several samples were examined for the reaction tests of photocatalytic direct ethane conversion under non-oxidative conditions in a flow reactor and the results are given in Table 1. The main products observed were *n*-butane, ethene, and methane as well as hydrogen, while very small amounts of other hydrocarbon products such as propene and propane were also found in some cases. No *i*-butane was detected.

n-Butane would be formed via photocatalytic non-oxidative coupling of ethane with hydrogen formation (NOCE, eq. 6) in the same way as non-oxidative coupling of methane (NOCM) in the present conditions. This is a thermodynamically unfavourable reaction with the positive Gibbs energy change. If calculated, the values of the equilibrium constant and the equilibrium conversion for the NOCE at 298 K are 3.03 $\times 10^{-9}$ and 0.011 %, respectively, meaning that the NOCE does not almost takes place at 298 K thermodynamically.

$$2\ C_2H_6 \rightarrow C_4H_{10} + H_2 \qquad \Delta_r G_{298K} = 48.6\ \text{kJ mol}^{-1} \qquad (6)$$

Ethene should be formed via photocatalytic dehydrogenation of ethane (DH), where non-oxidative (eq. 7) or oxidative (eq. 8) pathways are possible. In the former case of non-oxidative dehydrogenation (NODH), ethene and hydrogen are produced, which is also a thermodynamically unfavourable reaction with a much larger value of the positive Gibbs energy change than the NOCE. In the latter case of oxidative dehydrogenation (ODH), the

lattice oxygen (O_L) of the photocatalyst surface is tentatively assumed as the oxidant and ethene and water would be formed.

$$C_2H_6 \rightarrow C_2H_4 + H_2 \qquad \Delta_rG_{298K} = 101 \text{ kJ mol}^{-1} \qquad (7)$$

$$C_2H_6 + O_L \rightarrow C_2H_4 + H_2O \qquad (8)$$

Methane as a very minor product would be formed via hydrocracking (HDC) of ethane with hydrogen (eq. 9) as the reverse reaction of NOCM, where hydrogen should be supplied via the NOCE and the NODH (eq. 6 and 7). Another possible reaction would be oxidative route with the reduction of photocatalyst surface via partial oxidation of ethane to acetic acid and its decomposition[31] (eq. 10) although CO_2 was not detected due to very low sensitivity in the present conditions.

$$C_2H_6 + H_2 \rightarrow 2\ CH_4 \qquad \Delta_rG_{298K} = -68.6 \text{ kJ mol}^{-1} \qquad (9)$$

$$C_2H_6 + 3O_L \rightarrow CH_3COOH + H_2O \rightarrow CH_4 + CO_2 + H_2O \qquad (10)$$

In the present reaction system, no products were observed in the dark, without the photocatalyst, and without ethane in the feed gas, meaning that these reactions would be photocatalytic or photo-induced reactions and the products would be derived from ethane.

Table 1 Results of the reaction tests of photocatalytic direct ethane conversion[a]

Entry	Sample[b]	Production rates[c] / μmol h^{-1}				Yield[d]	S_{C4H10}[e]	S_{C2H4}[f]	$R_{HC/H2}$[g]
		C_4H_{10}	C_2H_4	CH_4	H_2	(%)	[NOCE]	[NODH]	
1	Ga_2O_3	0.054	0.057	trace[h]	0.097	0.002	65.5	34.5	1.1
2	Pd/Ga_2O_3	trace[h]	0.017	nd[i]	trace[h]	0.0003	–[j]	100	–[j]
3	Pd–Bi/Ga_2O_3	nd[i]	0.26	nd[i]	trace[h]	0.004	–[j]	100	–[j]
4[k]	Au(0.4)/Ga_2O_3	0.65	0.14	0.016	0.27	0.021	89.3	9.6	2.9
5	TiO_2	nd[i]	trace[h]	0.043	nd[i]	0.0006	–[j]	–[j]	–[j]
6[k]	Au(0.4)/TiO_2	0.77	0.33	0.031	0.69	0.028	81.0	17.4	1.5
7[l]	Al_2O_3	0.13	0.072	0.028	0.040	0.005	72.2	20.0	4.4
8	Au(0.4)/Al_2O_3	0.091	0.033	nd[i]	nd[i]	0.003	84.7	15.3	–[j]

[a]The reaction conditions were as follows, photocatalyst in a quartz cell = 0.8 g (Ga_2O_3, Pd/Ga_2O_3, Pd–Bi/Ga_2O_3, and Au/Ga_2O_3), 0.6 g (TiO_2 and Au/TiO_2), or 0.4 g (Al_2O_3 and Au/Al_2O_3); photoirradiation area = 4 cm^2; cell volume = 0.4 cm^3; feed gas = 10% of C_2H_6 in Ar (total flow rate 30 mL min^{-1}); contact time = 0.8 s; space velocity (SV) = 4500 h^{-1}; light intensity = *ca.* 20 mW cm^{-2}; reaction temperature = *ca.* 320 K. [b]The loading amount of Au was 0.4 mol% in entries 4, 6, and 8 while the loading amount of Pd and Bi each was 0.18 mol% in entries 2

and 3. [c]The production rates were measured 5.5 h later from the start of the photoirradiation. [d]Calculated as shown in eq. 1. [e]Calculated as shown in eq. 2. [f]Calculated as shown in eq. 3. [g]Calculated as shown in eq. 4. [h]The amount of observed product was less than 0.01 μmol h^{-1}. [i]nd = not detected. [j]Could not be calculated. [k]The reaction tests were done three times and the average values are given here. [l]Very small amounts of many other products like CO, C_3H_6, and C_3H_8 were also detected.

Gallium oxide (Ga_2O_3) is a well-studied material both as catalyst[32–34] and photocatalyst[35–38] for hydrocarbon conversions, which was stable even in the present reductive reaction conditions in contrast to the TiO_2 sample as mentioned later.[25,26] The Ga_2O_3 sample produced *n*-butane, ethene, and hydrogen with the production rates of 0.054, 0.057, and 0.097 μmol h^{-1}, respectively (Table 1, entry 1). The observed hydrogen production rate was comparable to the sum of the production rates of *n*-butane and ethene since both the NOCE and the NODH reactions provide hydrogen as a product and the ratio of hydrocarbons and hydrogen was close to unity, $R_{HC/H2}$=1.1, meaning that these NOCE and NODH reactions proceeded with the stoichiometric ratio of the products without by-products. The production rates for *n*-butane and ethene are almost the same. These facts suggest that both the NOCE and the NODH reactions selectively and competitively occurred (eq. 6 and 7) over the Ga_2O_3 sample. The selectivity based on ethane to form *n*-butane was high such as 65.5%.

Since in our previous studies, Pd/Ga_2O_3 (Chapter 2) and Pd–Bi/Ga_2O_3 photocatalysts (Chapter 3) showed high activity with high selectivity for the NOCM,[25,26] these samples were prepared following the same procedures with the same loading amount described in our last study[26] and examined for the photocatalytic direct ethane conversion. Contrary to expectations, only a small amount of ethene was observed over these samples with trace amount of hydrogen (Table 1, entries 2–3), indicating that these samples are not efficient for the photocatalytic direct ethane conversion to butane. Although the DH reaction proceeded, the NOCE did not take place on the Pd–Bi/Ga_2O_3 sample at all. This result suggests that the required property for the NOCE is not the same as that for the NOCM and the same photocatalyst could not be always efficient for further conversion of the product in the NOCM. In addition, it is expected that these photocatalysts can promote the NOCM selectively without successive coupling of the product.

Gold (Au) is used as a cocatalyst for the photocatalysts in the methane conversion reactions such as the NOCM,[28,39] and the oxidative methane conversion,[40,41] and also in other reactions like organic chemical conversions.[42] It was found that loading of Au cocatalyst on the Ga_2O_3 sample resulted in an increase of the yield, over which *n*-butane, ethene, methane

and hydrogen were produced (Table 1, entry 4). *n*-Butane was obtained as the major hydrocarbon product in photocatalytic direct ethane conversion over the Au(0.4)/Ga_2O_3 sample with its production rate and selectivity being 0.65 μmol h^{-1} and 89.3%, respectively, and the production rate of *n*-butane was 12 times higher than that over the bare Ga_2O_3 sample, meaning that the Au(0.4)/Ga_2O_3 sample efficiently and selectively promotes the NOCE.

Titanium dioxide (TiO_2) is a representative photocatalyst.[28,43] The bare TiO_2 sample mainly yielded methane with a trace amount of ethene without formation of hydrogen and butane (Table 1, entry 5). The color of the bare TiO_2 sample varied from white (Figure 3a) to blue (Figure 3b) during the reaction, especially at the downstream part. The lack of hydrogen formation and the color change suggest that TiO_2 is reduced by ethane and the produced hydrogen, i.e., TiO_2 is unstable in the reductive reaction conditions under photoirradiation. Thus, the most plausible reaction would be a combination of partial oxidation of ethane with the surface oxygen and decomposition of acetic acid (eq. 10) as well as reduction of the TiO_2 surface by methane.

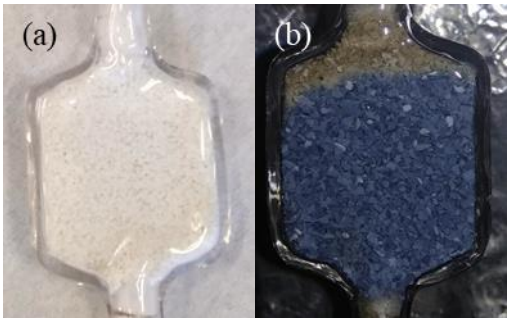

Figure 3 Photographs of the sample cell (a) before and (b) after the reaction test of photocatalytic ethane conversion with the TiO_2 sample. The photograph of the sample cell in b was taken before removing the reactor from the set-up.

Loading the Au cocatalyst drastically increased the activity of the TiO_2 sample also. The Au(0.4)/TiO_2 sample exhibited the high production rate of *n*-butane and ethene such as 0.77 and 0.33 μmol h^{-1}, respectively (Table 1, entry 6), which were higher than those over the Au(0.4)/Ga_2O_3 sample. The Au(0.4)/TiO_2 sample showed the highest products yield among all the samples given in Table 1. Over the Au(0.4)/TiO_2 sample also, *n*-butane was the major hydrocarbon product and its selectivity was 81.0%, meaning that the NOCE was also the major pathway of product formation in the photocatalytic direct ethane conversion over the Au(0.4)/TiO_2 sample. This high performance for the NOCE is consistent with the report of Au loaded TiO_2 photocatalyst as a good photocatalyst for the NOCM.[28] Here, it is to be noted that the Au loaded TiO_2 as an efficient photocatalyst for the NOCM also showed good performance

for the NOCE while the Pd-Bi loaded Ga_2O_3 photocatalyst did not. Thus, a photocatalyst active for the NOCM is not always active for the NOCE and it would depend on the intrinsic properties of the photocatalyst material itself. The Pd/Ga_2O_3 and $Pd\text{-}Bi/Ga_2O_3$ photocatalysts tended to yield not butane but ethene, suggesting these samples enhanced ethane conversion according to a different mechanism. This might be related to the catalytic properties of Ga_2O_3 in hydrocarbon conversion.[44]

Aluminium oxide (Al_2O_3) is usually used as an insulator support and acid-base catalyst,[45] while it has also photocatalytic property for the NOCM as mentioned above.[19,20] In the present reaction conditions, it produced *n*-butane, ethene, methane and hydrogen with a selectivity of *n*-butane and ethene of 72.2% and 20.0%, respectively (Table 1, entry 7). Other products such as carbon monoxide, propene and propane were also observed with Al_2O_3 meaning that the mechanism of photocatalytic ethane conversion on the insulator support such as Al_2O_3 is different from that on the semiconductor photocatalyst such as Ga_2O_3 and TiO_2. A small absorption was shown by the bare Al_2O_3 in the DR UV-vis spectrum (Figure 4). A similar absorption is reported in the literature.[46] Besides, Al_2O_3 has many acid and base sites[44] and the hydroxyl groups on the surface of Al_2O_3 are sometimes considered responsible for its photoactivity.[47] The light can be absorbed by these surface species and then this photoenergy can be transferred to the adsorbed ethane molecules resulting in the formation of products by photocatalytic reactions.

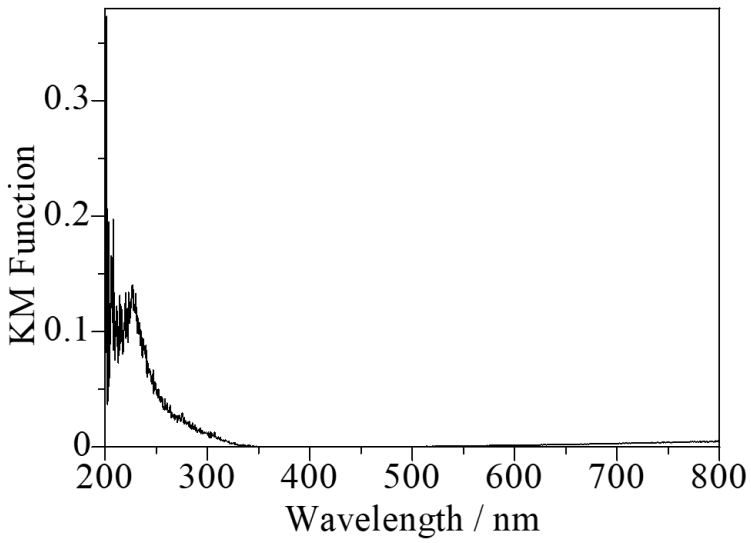

Figure 4 DR UV-vis spectra of the bare Al_2O_3 sample.

In contrast to the above cases, loading of the Au cocatalyst decreased the photocatalytic performance of the bare alumina (Table 1, entry 8). The photocatalytic active sites and the

reaction mechanism on the alumina surface would be definitely different from those on the semiconductor photocatalyst, i.e., the surface sites are excited by photon to promote the reactions and the Au particles would disturb the surface activity.

Among the several samples, the Au(0.4)/TiO_2 sample exhibited the highest photocatalytic performance. Thus, further investigation was carried out on the Au/TiO_2 photocatalysts.

4.3.2 Optimization of the loading amount of Au in Au/TiO_2 samples

The loading amount of Au cocatalyst is varied in the Au/TiO_2 samples, where the loading amount of Au was confirmed to be correct by XRF as shown in Table 2.

Table 2 Loading amount of Au in Au(*x*)/TiO_2 samples

S. No.	Sample [a]	Loading amount of Au (mol %) [b]
1	Au(0.1)/TiO_2	0.08
2	Au(0.2)/TiO_2	0.18
3	Au(0.4)/TiO_2	0.42
4	Au(1.0)/TiO_2	1.04

[a] The samples were prepared by the photodeposition method. [b] Determined by XRF.

The results of the photocatalytic activity tests are shown in Table 3. As opposed to a very small activity with the bare TiO_2 sample (Table 3, entry 1 and also Table 1, entry 5), the activity increased after depositing Au cocatalyst on the TiO_2 sample (Table 3, entries 2–5).

Table 3 Optimization of the loading amount of Au in the Au(*x*)/TiO_2 samples[a]

Entry	Loading amount (mol%)	Production rates[b] / μmol h^{-1}				Yield[c] (%)	S_{C4H10}[d] [NOCE]	S_{C2H4}[e] [NODH]	$R_{HC/H2}$[f]
		C_4H_{10}	C_2H_4	CH_4	H_2				
1[g]	0	nd[h]	trace[i]	0.043	nd[h]	0.0006	–[j]	–[j]	–[j]
2	0.10	2.05	0.090	0.083	0.47	0.062	95.9	2.1	4.4
3	0.20	0.92	0.11	0.055	0.63	0.029	91.8	5.5	1.5
4	0.40	0.77	0.33	0.031	0.69	0.028	81.0	17.4	1.5
5	1.0	0.64	0.28	0.030	0.60	0.023	80.5	17.6	1.5

[a]The reaction conditions were same as those described in the footnote *a* of Table 1. [b]Production rates were measured after 5.5 h. [c]Calculated as shown in eq. 1. [d]Calculated as shown in eq. 2. [e]Calculated as shown in eq. 3. [f]Calculated as shown in eq. 4. [g]Bare TiO_2

sample (P-25) was used in the reaction test and this is the same result listed in Table 1, entry 5. [h]nd = not detected. [i]The amount of observed product was less than 0.01 μmol h^{-1}. [j]Could not be calculated.

A very small amount of Au deposition of 0.1 mol% much increased the yield of the reaction and the *n*-butane formation rate of 2.05 μmol h^{-1} with the selectivity of 95.9% were observed although the value of *R* was high (Table 3, entry 2). On increasing the loading amount to 0.20–1.0 mol%, the yield of the reaction decreased but the value of *R* was improved (Table 3, entries 3–5). Among them, the Au(0.2)/TiO_2 sample showed the best performance with the higher production rates and selectivity of *n*-butane of 0.92 μmol h^{-1} and 91.8 %, respectively with a moderate value of *R* of 1.5 (Table 3, entry 3). The apparent quantum efficiency (AQE) for *n*-butane formation via the NOCE was calculated to be 0.02 % over the Au(0.2)/TiO_2 photocatalyst assuming that two photons were used to form one butane molecule as discussed later. The yield was calculated to be 0.029 % with the Au(0.2)/TiO_2 sample which exceeded the thermodynamic equilibrium conversion.

Although the bare TiO_2 sample was not stable under the reductive reaction conditions and showed no production of hydrogen as mentioned above, after loading the Au cocatalyst we could observe hydrogen with all the Au/TiO_2 samples and the value of $R_{HC/H2}$ was improved to be 1.5 when the loading amount was equal to or higher than 0.2 mol%. This suggests that the loaded Au species on the surface reacts with the unstable sites of the TiO_2 surface to stabilize it as a result, i.e.; the stabilized moieties are scarcely reduced under the reaction conditions or does not take part in the oxidative reactions such as eq. 8 and 10. The number of such stabilized moieties would depend on the loading amount of the Au cocatalyst, i.e., 0.2 mol% of Au loading would be enough to diminish the unstable surface sites and thus the value of $R_{HC/H2}$=1.5, close to an ideal value, was obtained (Table 3, entries 3–5), while a small amount of Au such as 0.1 mol% would not be enough and thus a high value of $R_{HC/H2}$ was obtained (Table 3, entry 2). Such kind of interfacial structure of Au/TiO_2 sample is previously also suggested based on both experimental results[48] and the theoretical calculations.[49,50] It is also reported that a low Au content will enable the small Au species to be imbedded in the surface structure while a high Au content will increase the particle size and give the nanoparticles on the surface.[48] Over all the Au/TiO_2 samples, the NOCE to form *n*-butane was the major reaction pathway with the high selectivity being in the range of 96–80 %.

However, the reaction selectivity to *n*-butane formation varied with the Au loading amount. With the increase of the Au loading from 0.1 to 0.4 mol%, the yield and selectivity for the NOCE decreased while those for the NODH to form ethene increased. The ethene

production rate was the highest on the Au(0.4)/TiO_2 photocatalyst, 0.33 μmol h^{-1}. The AQE for ethene formation on the Au(0.4)/TiO_2 was 0.008 %, where tentatively a two photon process was assumed for the calculation.

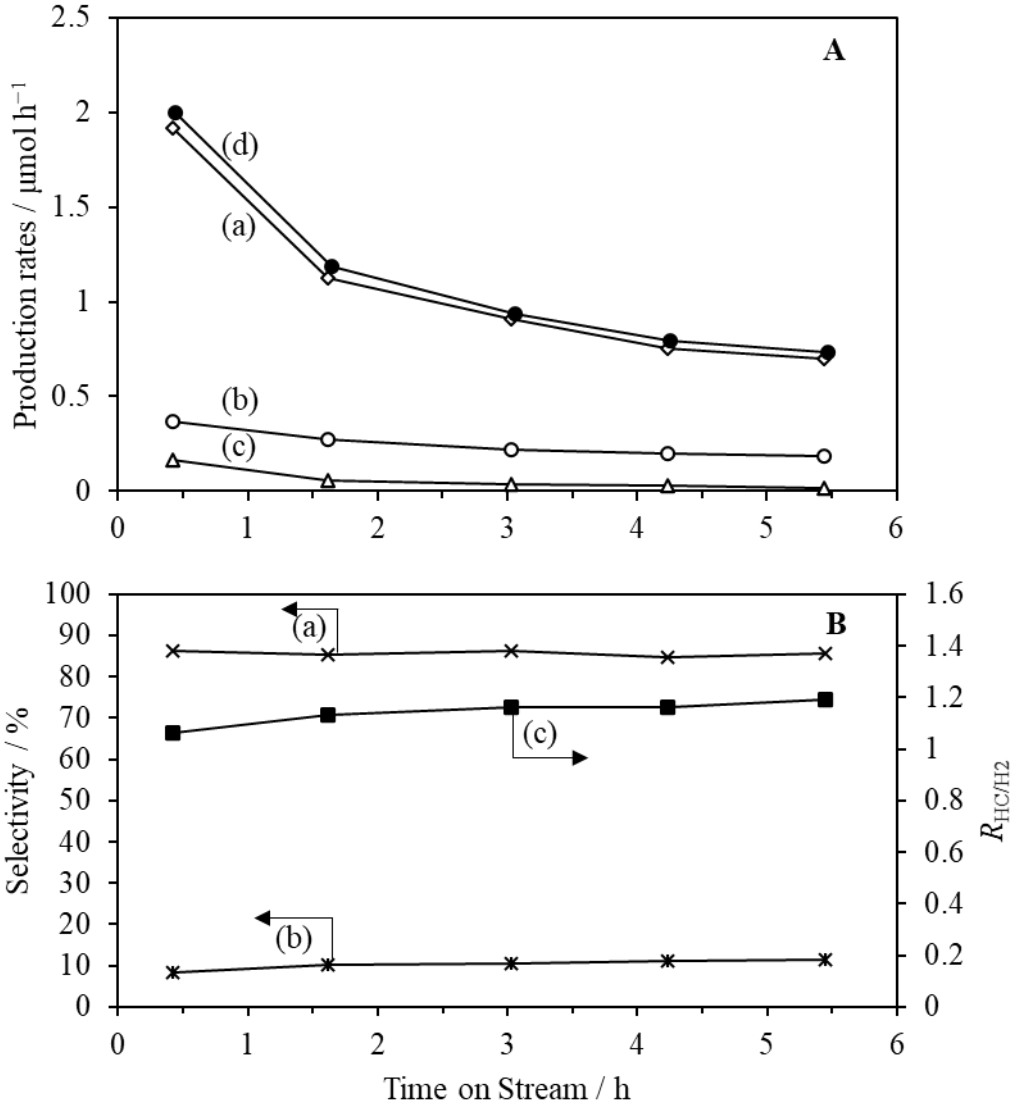

Figure 5 Time course of production rates of (a) butane, (b) ethene, (c) methane, and (d) hydrogen, and (B) Time course of selectivity toward (a) butane, (b) ethene, and (c) the $R_{CH/H2}$ value, in the reaction test of photocatalytic direct ethane conversion with the Au(0.4)/TiO_2 photocatalyst. Reaction conditions were same as those described in the footnote *a* of Table 1.

We studied the variation of the products formation with time in the photocatalytic direct ethane conversion reaction and Figure 5A shows the time course of the production rates with the Au(0.4)/TiO_2 sample as a typical example. The production rates decreased in the beginning and then tended to become stable after 5.5 h of the photoirradiation so that the values at 5.5 h later were listed in Table 1 and Table 3, i.e., the production rates of *n*-butane, ethene, methane

and hydrogen were 0.77, 0.33, 0.031, and 0.69 μmol h^{-1}, respectively after 5.5 h with the yield being 0.028%. The trend of the reaction selectivity to *n*-butane and ethene as well as the *R* value did not change much with time (Figure 5B). However, the activity of the sample decreased in the beginning as shown in Figure 5A. This decrease might be due to the increase in the particle size of Au nanoparticles by its aggregation in the Au(0.4)/TiO_2 sample during the reaction as discussed later.

4.3.3 Characterization

We characterized the Au/TiO_2 samples by some techniques.

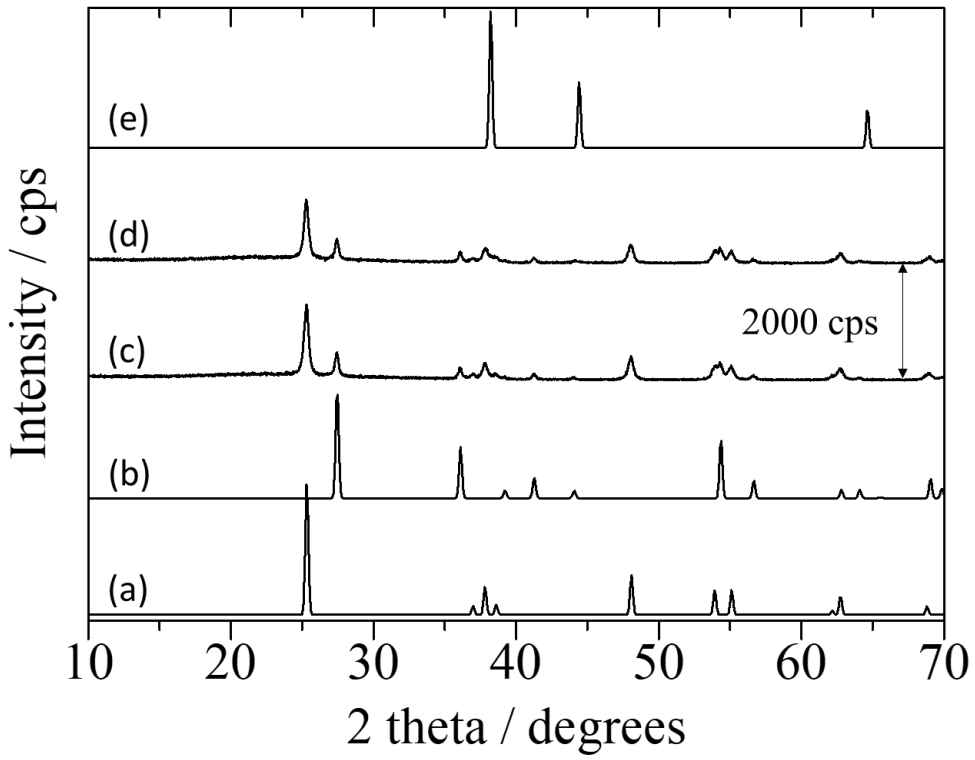

Figure 6 XRD patterns of (a) anatase TiO_2 from a database (ICSD #9852), (b) rutile TiO_2 from the database (ICSD #9161), (c) the TiO_2 sample, (d) the Au(0.4)/TiO_2 sample, and (e) Au from the database (ICSD #52249).

The XRD patterns of various samples are shown in Figure 6. The employed TiO_2 sample (P-25) was a mixed crystal of anatase and rutile phases and it was evident in its XRD pattern (Figure 6c) which consisted of the lines of both the anatase phase (Figure 6a, ICSD #9852)[51] and the rutile phase (Figure 6b, ICSD #9161)[52] with no additional lines. After loading of the Au cocatalyst in Au(0.4)/TiO_2 sample, a very broad and ambiguous diffraction line at 38.2° overlapping with those of anatase TiO_2 was observed (Figure 6d), which is assignable to

the main diffraction of metallic Au (Figure 6e, ICSD #52249).[53] This observation suggests that the Au cocatalyst loaded by the photodeposition method was in metallic state in the Au(0.4)/TiO_2 sample. The XRD patterns of other Au/TiO_2 samples are given in Figure 7. The diffraction lines derived from the Au nanoparticles further became evident in the XRD patterns of the Au(1.0)/TiO_2 sample (Figure 7 e).

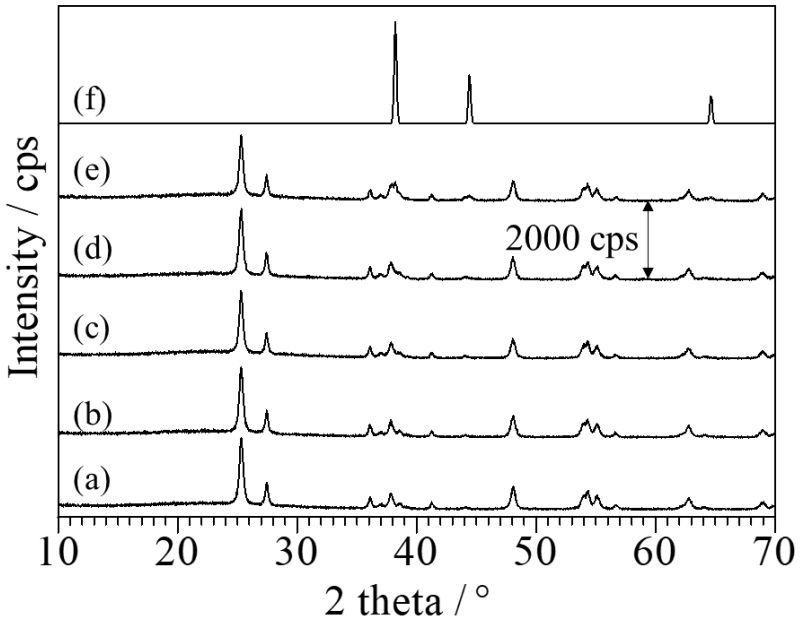

Figure 7 XRD patterns of the samples, (a) TiO_2, (b) Au(0.1)/TiO_2, (c) Au(0.2)/TiO_2, (d) Au(0.4)/TiO_2, (e) Au(1.0)/TiO_2, and (f) Au from the database (ICSD#52249).

The SEM image of the TiO_2 sample and the SEM image and EDX elemental mappings of the Au(0.4)/TiO_2 samples are shown in Figure 8. The agglomerated nanoparticles of TiO_2 were observed with no regular shape (Figure 8a). The morphology did not change much after depositing Au species in the Au(0.4)/TiO_2 sample (Figure 8b). The elemental mappings of the Au(0.4)/TiO_2 sample showed that Au nanoparticles were dispersed on TiO_2 surface (Figure 8c-e).

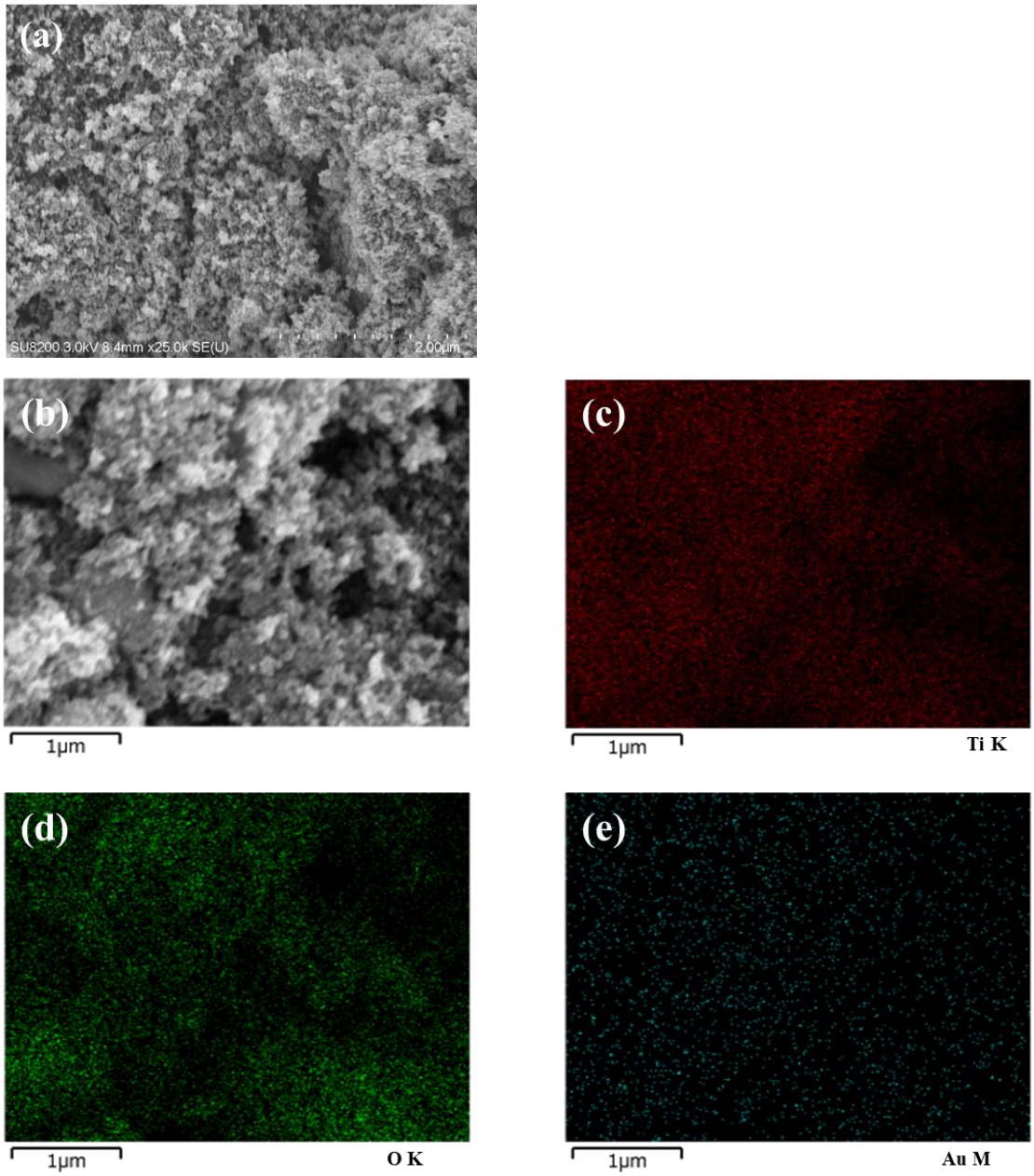

Figure 8 (a) SEM image of the bare TiO_2 sample, and (b) the SEM image and (c-e) elemental mappings of the Au(0.4)/TiO_2 sample.

We further recorded the TEM and STEM images of various Au/TiO_2 samples in order to know the particle size of Au nanoparticles. Spherical Au nanoparticles can be seen in the TEM image of the Au(0.4)/TiO_2 sample (Figure 9a). In the STEM image, Au nanoparticles can be distinguished very easily due to its high contrast to the TiO_2 nanoparticles (Figure 9b). The particle size distribution of Au nanoparticles clarified the average particle size to be 18.1 nm in Au(0.4)/TiO_2 sample (Figure 9c). The average particle size of Au nanoparticles increased to be 20.5 nm after the reaction (Figure 9d, e).

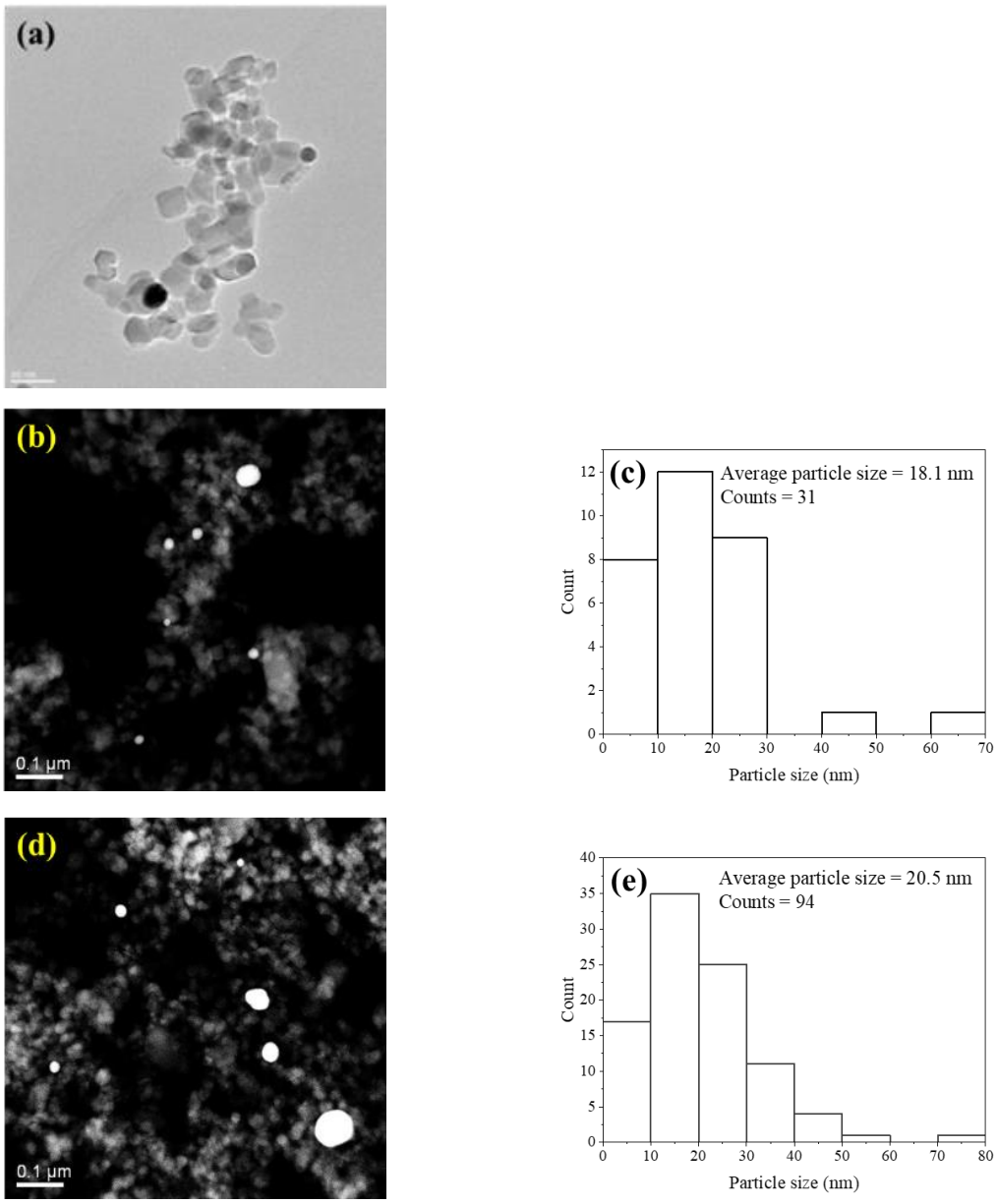

Figure 9 (a) TEM image, (b) STEM image and (c) particle size distribution in the Au(0.4)/TiO_2 sample before the use for the reaction test; and (d) STEM image and (e) particle size distribution of the Au(0.4)/TiO_2 sample after the use for the reaction test.

The STEM images and the particle size distribution of other Au/TiO_2 samples are given in Figure 10. The average particle size of the Au nanoparticles increased with an increase in the loading amount of Au in the Au/TiO_2 samples.

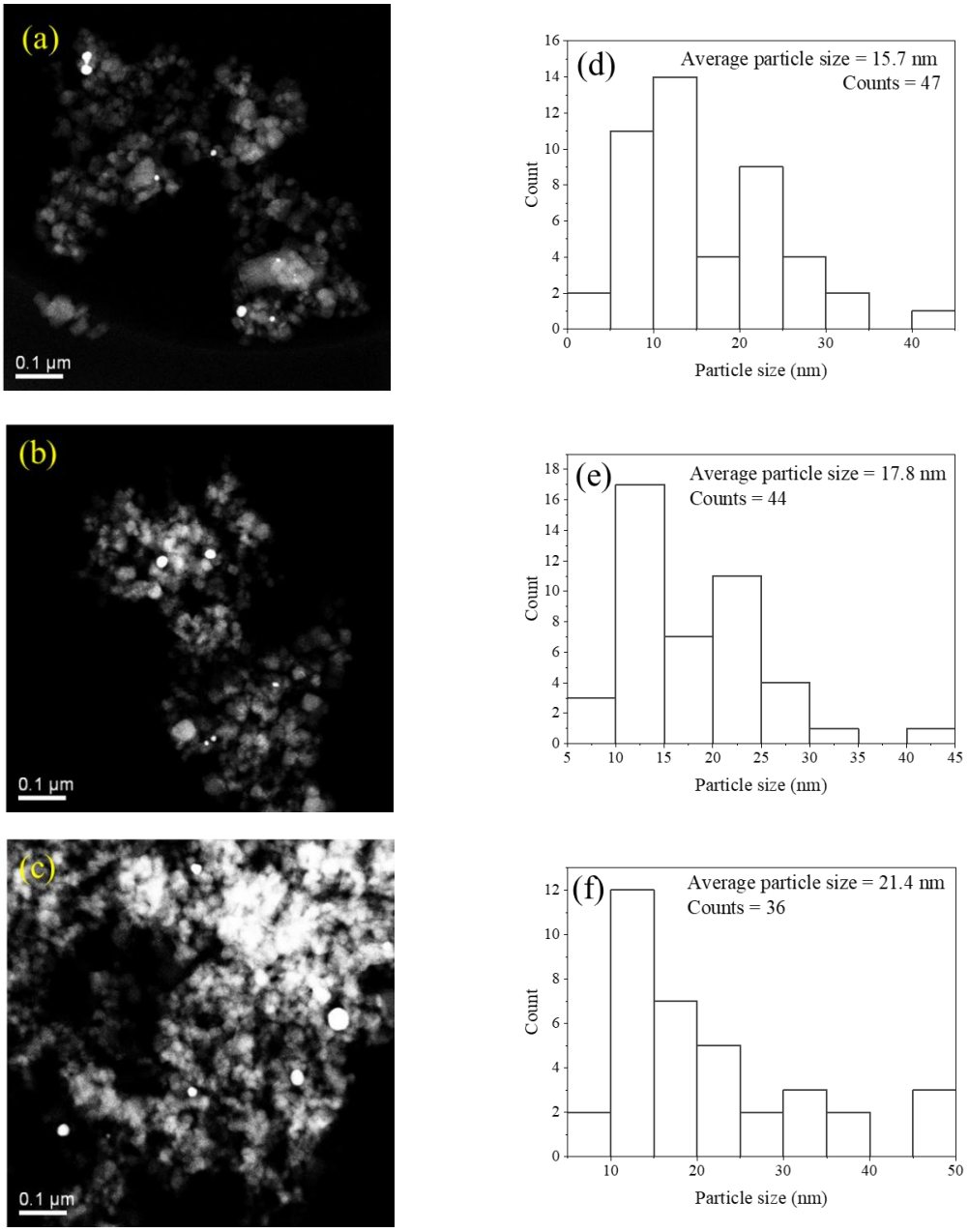

Figure 10 STEM images (a–c) and particle size distribution of Au nanoparticles (d–f) in the Au(0.1)/TiO_2, Au(0.2)/TiO_2, and Au(1.0)/TiO_2 samples.

The photoabsorption properties of the samples were investigated by the DR UV-vis spectroscopy. The bare TiO_2 sample showed a large absorption band below 400 nm in the wavelengths (Figure 11a) from which its band gap was calculated to be around 3.6 eV, which is in agreement with the literature.[28] The Au(0.4)/TiO_2 sample exhibited an additional intense and broad band centred at nearly 550 nm (Figure 11b), which is assignable to the localized surface plasmon resonance (LSPR) band of metallic Au nanoparticles.[28] The tailing part of this LSPR band at shorter wavelength overlapped with the large band of TiO_2, which made the position of the absorption edge to be slightly shifted to longer wavelength. This means that the

Au cocatalyst existed as metallic nanoparticles on the TiO_2 surface in Au(0.4)/TiO_2 sample, in agreement with its XRD profile (Figure 6d and Figure 7d). We also recorded the DR UV-vis spectra of the Au(0.4)/TiO_2 sample after using for the photocatalytic reaction test. The intensity of the characteristic Au LSPR peak is increased and its position is slightly red-shifted (Figure 11c), which indicates the increase in the particle size of Au nanoparticles during the photocatalytic reaction test.[54] Thus, the results in the DR UV-vis spectra were in agreement with the STEM results for the increase in the particle size after the reaction test.

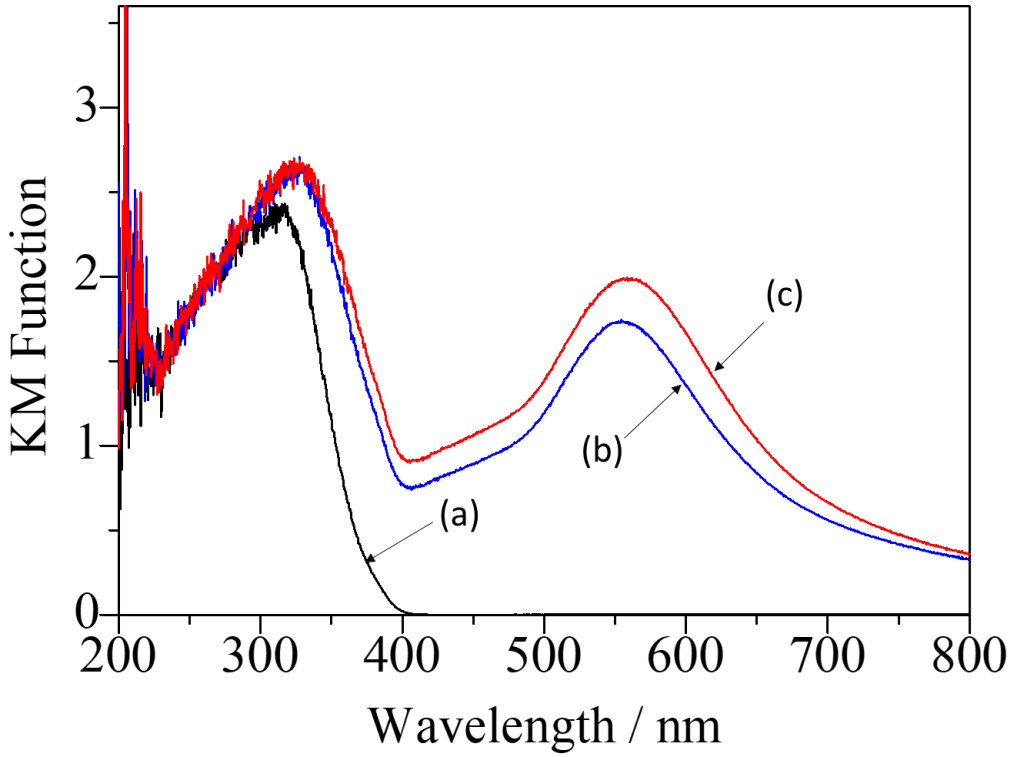

Figure 11 DR UV-vis spectra of (a) the TiO_2 sample and the Au(0.4)/TiO_2 sample (b) before and (c) after the use for the reaction test of photocatalytic direct ethane conversion.

The DR UV-vis spectra of other Au/TiO_2 samples are shown in Figure 12. All the Au/TiO_2 samples showed the absorption band due to the LSPR of the Au nanoparticles and the intensity of this band increased with an increase in the loading amount of Au cocatalyst. This is an expected trend since the number and the particle size of the Au nanoparticles should be increased with an increase of loading amount of Au cocatalyst.

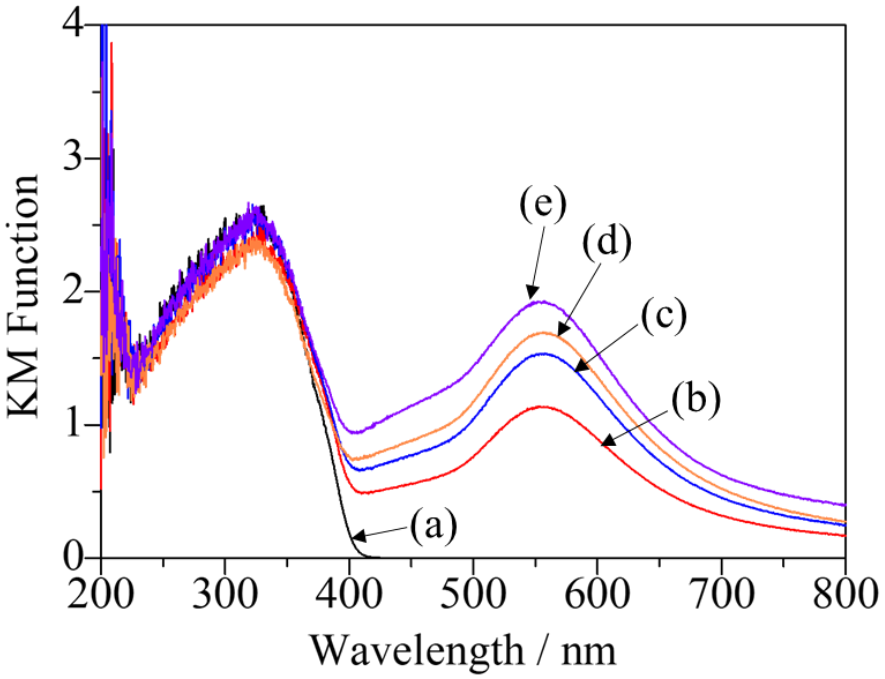

Figure 12 DR UV-vis spectra of the samples; (a) TiO_2, (b) Au(0.1)/TiO_2, (c) Au(0.2)/TiO_2, (d) Au(0.4)/TiO_2, and (e) Au(1.0)/TiO_2.

The Au L_{III}-edge XAFS spectra of the Au foil and the Au(0.4)/TiO_2 sample before and after the reaction are shown in Figure 13A. The shape of the XAFS spectra of the Au(0.4)/TiO_2 sample (Figure 13A, b) was similar to that of the Au foil (Figure 13A, a), suggesting that the state of the Au cocatalyst in the Au(0.4)/TiO_2 sample was metallic. The sample after being used for the photocatalytic reaction test exhibited almost the same XAFS spectra (Figure 13A, c), indicating that the chemical state of the gold didn't change during the reaction in the Au(0.4)/TiO_2 sample. The Au L_{III}-edge k^3-weighted Fourier Transform (FT) EXAFS of the Au(0.4)/TiO_2 sample before and after the reaction is shown in Figure 13B. The peak in the range of 2.0–3.0 Å corresponds to the Au–Au bond[55] and the intensity of this peak is slightly increased after the reaction (Figure 13B, b). This increase in the intensity is due to the increase of the particle size of Au nanoparticles.[55] Thus, the EXAFS results further support the DR UV-vis results.

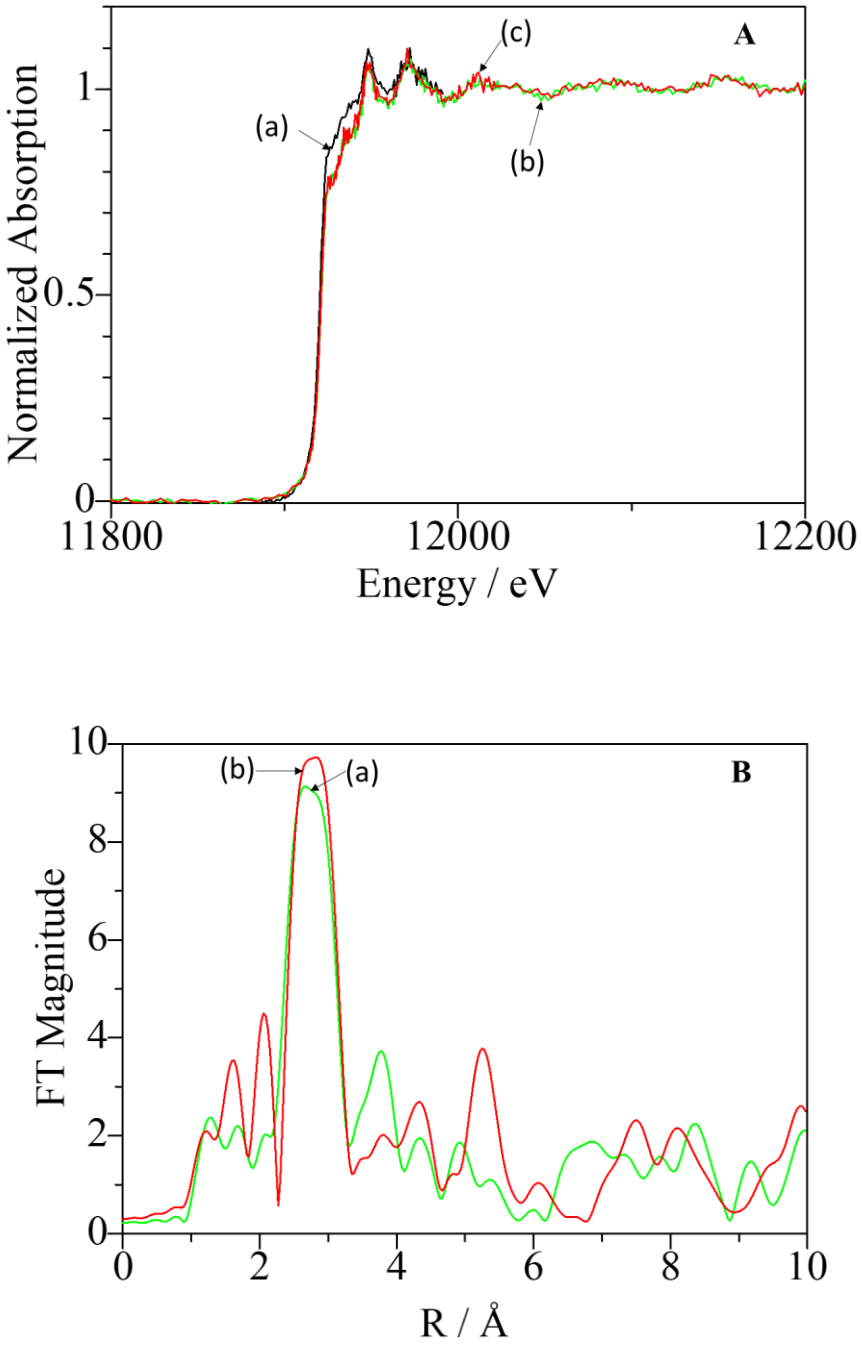

Figure 13 (A) Au L_{III}-edge XANES spectra of (a) the Au foil, Au(0.4)/TiO_2 sample (b) before and (c) after the use for the reaction test, and (B) Fourier Transform of EXAFS of Au(0.4)/TiO_2 sample (a) before and (b) after the use for the reaction test of photocatalytic direct ethane conversion.

4.3.4 Reaction test with optical filter

As mentioned above, the Au cocatalyst was present as metallic Au nanoparticles on the Au(0.4)/TiO_2 photocatalyst and showed the intense LSPR band centred at nearly 550 nm in its

DR UV-vis spectrum (Figure 11b and also Figure 12d). It is well known that the LSPR can contribute to the photocatalytic activity.[39,56–58] In order to know whether or not this absorption contributed to the reaction, an additional reaction test was carried out with an optical filter allowing the light of wavelengths larger than 440 nm to pass and the results are given in Table 4. As opposed to the high activity with no optical filter (Table 4, entry 1), a trace amount of ethene and no other products were observed when the optical filter ($\lambda_{transmission} \geq 440$ nm) was used (Table 4, entry 2). This result indicates that the LSPR of the Au nanoparticles did not contribute to the reaction without photoexcitation of the TiO_2 photocatalyst and the photoexcitation of TiO_2 was required for the photocatalytic reactions over the Au(0.4)/TiO_2 sample. This result is in agreement with the Au/TiO_2 photocatalyst for NOCM.[28]

Table 4 Result of the reaction tests of photocatalytic direct ethane conversion with an optical filter over the Au(0.4)/TiO_2 sample [a]

Entry	Conditions	Production rates[b] / μmol h^{-1}			
		C_4H_{10}	C_2H_4	CH_4	H_2
1	without filter	0.77	0.33	0.031	0.69
2	with filter	nd[c]	trace[d]	nd[c]	nd[c]

[a]The reaction conditions were same as those described in the footnote *a* of Table 1, except for the use of the optical filter ($\lambda_{transmission} \geq 440$ nm) in entry 2. [b]Production rates were measured after 5.5 h of the photoirradiation. [c]nd = not detected. [d]The amount of the product was less than 0.01 μmol h^{-1}.

4.3.5 Effect of thermal energy

Recently, photothermal catalytic reactions on supported metal catalysts have been reported,[59–61] where the light energy absorbed by the metal nanoparticles is converted to thermal energy to promote the catalysis on the metal catalyst. Thus, the reaction tests in the dark were carried out with the Au(0.4)/TiO_2 sample at various temperatures in the flow of ethane with Ar carrier gas to study the effect of thermal energy on the reaction. The results are given in Table 5. No products were observed at 323, 373, 423, and 473 K (Table 5, entries 1–4), meaning that ethane could not be activated by the thermal energy provided at these temperatures in the dark over the Au(0.4)/TiO_2 sample under the present reaction conditions. When we increased the temperature further, ethene, methane and hydrogen were produced on the Au(0.4)/TiO_2 sample and their production rates increased with increasing the temperature

in the range of 523–723 K (Table 5, entry 5–9), which is consistent with literatures,[44] while no *n*-butane was formed in dark even at these temperatures. It was clear that the product distribution in the thermal reaction was not the same as under photoirradiation. Further, this result confirmed that the formation of *n*-butane via the NOCE proceeded photocatalytically under photoirradiation while the dehydrogenation of ethane to ethene can be promoted by thermal energy on the Au catalyst in dark. Thus, it is suggested that at least the NOCE was not photothermal reaction but photocatalytic reaction.

Table 5 Effect of increasing the temperature in dark with the Au(0.4)/TiO_2 sample[a]

Entry	Temperature	Production rates[b] / μmol h^{-1}				
	(K)	C_4H_{10}	C_2H_4	CH_4	C_3H_6	H_2
1	323	nd[c]	nd[c]	nd[c]	nd[c]	nd[c]
2	373	nd[c]	nd[c]	nd[c]	nd[c]	nd[c]
3	423	nd[c]	nd[c]	nd[c]	nd[c]	nd[c]
4	473	nd[c]	nd[c]	nd[c]	nd[c]	nd[c]
5	523	nd[c]	0.026	0.22	nd[c]	0.48
6	573[d]	nd[c]	0.025	0.28	trace[e]	1.1
7	623[d]	nd[c]	0.23	0.27	trace[e]	1.9
8	673[d]	nd[c]	3.3	0.38	trace[e]	7.1
9	723[d]	nd[c]	23.5	0.82	trace[e]	31.2

[a]Other reaction conditions were same as those described in the footnote *a* of Table 1 in the main text. [b]Production rates were measured after 1.5 h at each temperature. [c]nd = not detected. [d]Small amount of CO was also observed. [e]The amount of the product was less than 0.01 μmol h^{-1}.

The similar product distribution and the variation with increasing temperature were also observed on the Au(0.4)/Ga_2O_3 sample (Table 6), where the production rate of ethene was almost equal to that of hydrogen, confirming that ethane dehydrogenation was selectively promoted over the Au catalyst supported on the Ga_2O_3 surface.

Table 6 Effect of increasing the temperature in dark with the Au(0.4)/Ga_2O_3 sample[a]

Entry	Temperature	Production rates[b] / μmol h^{-1}				
	(K)	C_4H_{10}	C_2H_4	CH_4	C_3H_6	H_2
1	323	nd[c]	nd[c]	nd[c]	nd[c]	nd[c]
2	373	nd[c]	nd[c]	nd[c]	nd[c]	nd[c]

3	423	nd[c]	nd[c]	nd[c]	nd[c]	nd[c]
4	473	nd[c]	nd[c]	nd[c]	nd[c]	nd[c]
5	523	nd[c]	trace[d]	0.07	nd[c]	0.17
6	623[e]	nd[c]	8.4	0.10	trace[d]	10.2
7	673[e]	nd[c]	126.2	0.11	trace[d]	128.8

[a]Other reaction conditions were same as those described in the footnote *a* of Table 1 in the main text. [b]Production rates were measured after 1.5 h at each temperature. [c]nd = not detected. [d]The amount of the product was less than 0.01 μmol h^{-1}. [e]Small amount of CO was also observed.

Under photoirradiation, the production rates of ethene were 0.14 and 0.33 μmol h^{-1} over the Au(0.4)/Ga_2O_3 and Au(0.4)/TiO_2 samples, respectively as mentioned above (Table 1). These production rates of ethene correspond to those obtained in dark at 560 and 624 K with the Au(0.4)/Ga_2O_3 sample and the Au(0.4)/TiO_2 sample, respectively; where these temperatures were estimated according to Arrhenius equation based on the results in Table 5 and Table 6. The Xe lamp emits the continuous light in the wavelength range of UV and visible light (Figure 2) and there is a possibility of conversion of visible light to heat. Thus, if the local temperature of the Au nanoparticles were 560 and 624 K under photoirradiation, it is possible to explain that under photoirradiation ethene might be produced through ethane dehydrogenation catalysed by the Au nanoparticles[62] on these supports with thermal energy converted from photoenergy.

4.3.6 Reaction pathways

At least, in the present study, it is clarified that the non-oxidative coupling of ethane (NOCE) was promoted photocatalytically. The reaction scheme of the NOCE would be proposed as follows: TiO_2 and Ga_2O_3 acting as the semiconductor photocatalysts can absorb the photons upon irradiation and electrons and holes are generated at their conduction band (CB) and valence band (VB), respectively. Ethyl radicals and protons are oxidatively produced by the photogenerated holes (eq. 11), and *n*-butane is formed by the coupling of two ethyl radicals (eq. 12), while hydrogen is reductively formed by the photogenerated electrons (eq. 13).

$$2C_2H_6 + 2h^+ \rightarrow 2\ {}^{\bullet}C_2H_5 + 2H^+ \quad (11)$$

$$2\ {}^{\bullet}C_2H_5 \rightarrow C_4H_{10} \quad (12)$$

$$2H^+ + 2e^- \rightarrow H_2 \quad (13)$$

As for the formation of ethene as a by-product, it is proposed that Au metal nanoparticles may promote dehydrogenation of ethane to ethene (eq. 7) as a catalyst[62] by the thermal energy that was converted from the photoenergy, while the possibility of photocatalytic dehydrogenation also could not be ruled out for examples by using one photon (eq. 14–17) or two photons (eq. 14, 15, 17–18) including a disproportionation of ethyl radical (eq. 18).[63] Further careful investigation is required to clarify how the side reaction to form ethene took place under photoirradiation.

One photon process

$$C_2H_6 + h^+ \rightarrow {}^{\bullet}C_2H_5 + H^+ \quad (14)$$

$$H^+ + e^- \rightarrow H^{\bullet} \quad (15)$$

$${}^{\bullet}C_2H_5 + H^{\bullet} \rightarrow C_2H_4 + H^{\bullet} \quad (16)$$

$$H^{\bullet} + H^{\bullet} \rightarrow H_2 \quad (17)$$

Two photons process

$${}^{\bullet}C_2H_5 + {}^{\bullet}C_2H_5 \rightarrow C_2H_4 + C_2H_6 \quad (18)$$

4.4 Conclusion

Photocatalytic direct conversion of ethane under non-oxidative conditions was studied in a flow reactor, and it was found that *n*-butane and hydrogen can be produced as the major products with the Au-loaded Ga_2O_3 photocatalyst and the Au-loaded TiO_2 photocatalysts via photocatalytic non-oxidative coupling of ethane (NOCE). Ethene and methane were also observed as additional hydrocarbon products.

The stability of the photocatalyst under the reductive reaction conditions is an important parameter similar to the case of the NOCM and so the Ga_2O_3 photocatalyst showed production of *n*-butane, ethene and hydrogen in nearly stoichiometric ratio. The Au(0.4)/Ga_2O_3 photocatalyst exhibited 12 times higher production of *n*-butane than the bare Ga_2O_3 photocatalyst along with hydrogen from ethane with the NOCE being the major reaction pathway and the selectivity to *n*-butane was as high as 89%.

Although the TiO_2 photocatalyst was not useful for the NOCE in the present conditions, the Au(0.2)/TiO_2 photocatalyst exhibited a higher photocatalytic activity for the NOCE, giving a high apparent quantum efficiency for butane formation such as AQE=0.02%, a high NOCE selectivity of 92%, and a moderate $R_{HC/H2}$ value of 1.5 and the yield of the reaction was 0.029%.

The reaction mechanism of the photocatalytic NOCE to produce *n*-butane from ethane via radical-radical coupling would be similar to that of the NOCM to form ethane from methane

while other reactions than the NOCE can take place in the photocatalytic direct conversion of ethane under nonoxidative conditions. Although the yield of ethene from ethane as one of the side reactions was also valuable, the mechanism of the ethene formation was unclarified, i.e., it remains possible that a photothermal dehydrogenation might take place under photoirradiation in the present conditions over supported Au catalysts.

Efforts to increase the production rate and the selectivity are needed for the further development of the photocatalytic direct conversion of ethane, and further detailed and careful investigations are required to clarify the reaction mechanisms.

Acknowledgement

The authors thank Mr. Tsutomu Kiyomura (Institute for Chemical Research, Kyoto University) for the measurements of the TEM and STEM images. A part of this work was supported by “Nanotechnology Platform” project of the MEXT, Japan, Grant Number JPMXP09A21KT0030. The XAFS spectra of the samples were measured at the BL12C of the Photon Factory (PF) with the approval of the Photon Factory Program Advisory Committee (Proposal number 2020G667). This work was financially supported by ISHIZUE 2020 of the Kyoto University Research Development Program, a Grant-in-Aid for Scientific Research (B) (21H01975), a Grant-in-Aid for Challenging Research (Exploratory, 20K21108) and a Grant-in-Aid for Young Scientists (19K15359) from the Japan Society for the Promotion of Science (JSPS), and the Program for Element Strategy Initiative for Catalysts & Batteries (ESICB, JPMXP0112101003), commissioned by the MEXT of Japan. S. P. Singh thanks the JICA for providing a scholarship under the FRIENDSHIP project to pursue his Ph.D. in Japan.

References

(1) Hagen, A.; Roessner, F. Ethane to Aromatic Hydrocarbons: Past, Present, Future. *Catal. Rev. - Sci. Eng.* **2000**, *42* (4), 403–437.

(2) Zhu, Y.; Shi, S.; Wang, C.; Hu, Y. H. Photocatalytic Conversion of Ethane: Status and Perspective. *Int. J. Energy Res.* **2020**, *44* (2), 708–717.

(3) Hashiguchi, B. G.; Konnick, M. M.; Bischof, S. M.; Gustafson, S. J.; Devarajan, D.; Gunsalus, N.; Ess, D. H.; Periana, R. A. Main-Group Compounds Selectively Oxidize Mixtures of Methane, Ethane and Propane to Alcohol Esters. *Science (80-.).* **2014**, *343* (March), 1232–1237.

(4) Shilov, A. E.; Shul'pin, G. B. Activation of C-H Bonds by Metal Complexes. *Chem. Rev.* **1997**, *97* (8), 2879–2932.

(5) Chen, H.; Li, L.; Hu, J. Upgrading of Stranded Gas via Non-Oxidative Conversion Processes. *Catal. Today* **2018**, *310* (April 2017), 94–97.

(6) Bañares, M. A. Supported Metal Oxide and Other Catalysts for Ethane Conversion: A Review; *Catal. Today* **1999**; *Vol. 51*, 319–348.

(7) Bywater, S.; Steacie, E. W. R. The Mercury ($^3P_1$) Photo-Sensitized Reaction of Ethane at High Temperatures. *J Chem Phys* **1951**, *19*, 326–329.

(8) Hu, A.; Guo, J. J.; Pan, H.; Zuo, Z. Selective Functionalization of Methane, Ethane, and Higher Alkanes by Cerium Photocatalysis. *Science (80-.).* **2018**, *361* (6403), 668–672.

(9) Wada, K.; Yoshida, K.; Takatani, T.; Watanabe, Y. Selective Photo-Oxidation of Light Alkanes Using Solid Metal Oxide Semiconductors. *Appl. Catal. A, Gen.* **1993**, *99* (1), 21–36.

(10) Brigden, C. T.; Poulston, S.; Twigg, M. V.; Walker, A. P.; Wilkins, A. J. J. Photo-Oxidation of Short-Chain Hydrocarbons over Titania. *Appl. Catal. B Environ.* **2001**, *32* (1–2), 63–71.

(11) Zhang, R.; Wang, H.; Tang, S.; Liu, C.; Dong, F.; Yue, H.; Liang, B. Photocatalytic Oxidative Dehydrogenation of Ethane Using CO2 as a Soft Oxidant over Pd/TiO_2 Catalysts to C_2H_4 and Syngas. *ACS Catal.* **2018**, *8* (10), 9280–9286.

(12) Wada, K.; Yoshida, K.; Watanabe, Y.; Suzuki, T. Selective Conversion of Ethane into Acetaldehyde by Photo-Catalytic Oxidation with Oxygen over a Supported Molybdenum Catalyst. *Appl. Catal.* **1991**, *74* (1), L1.

(13) Wang, X. T.; Zhong, S. H.; Xiao, X. F. Photo-Catalysis of Ethane and Carbon Dioxide to Produce Hydrocarbon Oxygenates over ZnO-TiO_2/SiO_2 Catalyst. *J. Mol. Catal. A*

Chem. **2005**, *229* (1–2), 87–93.

(14) Suzuki, J.; Fujimoto, K.; Mori, T.; Watanabe, M.; Hasegawa, Y. Photocatalytic Reduction of NO with C_2H_6 on a Hollandite-Type Catalyst. *J. Sol-Gel Sci. Technol.* **2000**, *19* (1–3), 775–778.

(15) Wada, K.; Yamada, H.; Watanabe, Y.; Mitsudo, T. A. Selective Photo-Assisted Catalytic Oxidation of Methane and Ethane to Oxygenates Using Supported Vanadium Oxide Catalysts. *J. Chem. Soc. - Faraday Trans.* **1998**, *94* (12), 1771–1778.

(16) Bitterwolf, T. E.; Kline, D. L.; Linehan, J. C.; Yonker, C. R.; Shane Addleman, R. Photochemical Carbonylation of Ethane under Supercritical Conditions. *Angew. Chemie - Int. Ed.* **2001**, *40* (14), 2692–2694.

(17) Yuliati, L.; Yoshida, H. Photocatalytic Conversion of Methane. *Chem. Soc. Rev.* **2008**, *37* (8), 1592–1602.

(18) Yoshida, H. Active Sites of Silica-Based Quantum Photocatalysts for Non-Oxidative Reactions. *Catal. Surv. from Asia* **2005**, *9* (1), 1–9.

(19) Kato, Y.; Yoshida, H.; Hattori, T. Photoinduced Non-Oxidative Coupling of Methane over Silica-Alumina and Alumina around Room Temperature. *Chem. Commun.* **1998**, No. 21, 2389–2390.

(20) Yoshida, H.; Matsushita, N.; Kato, Y.; Hattori, T. Active Sites in Sol-Gel Prepared Silica-Alumina for Photoinduced Non-Oxidative Methane Coupling. *Phys. Chem. Chem. Phys.* **2002**, *4* (11), 2459–2465.

(21) Kato, Y.; Matsushita, N.; Yoshida, H.; Hattori, T. Highly Active Silica-Alumina-Titania Catalyst for Photoinduced Non-Oxidative Methane Coupling. *Catal. Commun.* **2002**, *3* (3), 99–103.

(22) Yoshida, H.; Matsushita, N.; Kato, Y.; Hattori, T. Synergistic Active Sites on SiO_2−Al_2O_3−TiO_2 Photocatalysts for Direct Methane Coupling. *J. Phys. Chem. B* **2003**, *107* (33), 8355–8362.

(23) Yuliati, L.; Hamajima, T.; Hattori, T.; Yoshida, H. Nonoxidative Coupling of Methane over Supported Ceria Photocatalysts. *J. Phys. Chem. C* **2008**, *112* (18), 7223–7232.

(24) Yuliati, L.; Hattori, T.; Itoh, H.; Yoshida, H. Photocatalytic Nonoxidative Coupling of Methane on Gallium Oxide and Silica-Supported Gallium Oxide. *J. Catal.* **2008**, *257* (2), 396–402.

(25) Singh, S. P.; Anzai, A.; Kawaharasaki, S.; Yamamoto, A.; Yoshida, H. Non-Oxidative Coupling of Methane over Pd-Loaded Gallium Oxide Photocatalysts in a Flow Reactor. *Catal. Today* **2021**, *375*, 264–272.

(26) Singh, S. P.; Yamamoto, A.; Fudo, E.; Tanaka, A.; Kominami, H.; Yoshida, H. A Pd-Bi Dual-Cocatalyst-Loaded Gallium Oxide Photocatalyst for Selective and Stable Nonoxidative Coupling of Methane. *ACS Catal.* **2021**, *11*, 13768–13781.

(27) Wang, G.; Mu, X.; Li, J.; Zhan, Q.; Qian, Y.; Mu, X.; Li, L. Light-Induced Nonoxidative Coupling of Methane Using Stable Solid Solutions. *Angew. Chemie* **2021**, *133* (38), 20928–20932.

(28) Lang, J.; Ma, Y.; Wu, X.; Jiang, Y.; Hu, Y. H. Highly Efficient Light-Driven Methane Coupling under Ambient Conditions Based on an Integrated Design of a Photocatalytic System. *Green Chem.* **2020**, *22* (14), 4669–4675.

(29) Lu, Y.; Shen, Z.; Zhou, Y. Spectral Distribution of Xe Lamp Focused by Fresnel Lens on Focal Plane and Design of Fresnel Lens for Solar-Pumped Cr/Nd:YAG Ceramic. *J. Opt. Technol.* **2013**, *80* (8), 474.

(30) Rolt, S.; Clark, P.; Schmoll, J.; Shaw, B. J. R. Xenon Arc Lamp Spectral Radiance Modelling for Satellite Instrument Calibration. *Sp. Telesc. Instrum. 2016 Opt. Infrared, Millim. Wave* **2016**, *9904*, 99044V.

(31) Kraeutler, B.; Bard, A. J. Heterogeneous Photocatalytic Decomposition of Saturated Carboxylic Acids on TiO_2 Powder. Decarboxylative Route to Alkanes. *J. Am. Chem. Soc.* **1978**, *100* (19), 5985–5992.

(32) Michorczyk, P.; Ogonowski, J. Dehydrogenation of Propane to Propene over Gallium Oxide in the Presence of CO_2. *Appl. Catal. A Gen.* **2003**, *251* (2), 425–433.

(33) Zheng, B.; Hua, W.; Yue, Y.; Gao, Z. Dehydrogenation of Propane to Propene over Different Polymorphs of Gallium Oxide. *J. Catal.* **2005**, *232* (1), 143–151.

(34) Hou, Y.; Wu, L.; Wang, X.; Ding, Z.; Li, Z.; Fu, X. Photocatalytic Performance of α-, β-, and γ-Ga_2O_3 for the Destruction of Volatile Aromatic Pollutants in Air. *J. Catal.* **2007**, *250* (1), 12–18.

(35) Shimura, K.; Yoshida, H. Semiconductor Photocatalysts for Non-Oxidative Coupling, Dry Reforming and Steam Reforming of Methane. *Catal. Surv. from Asia* **2014**, *18* (1), 24–33.

(36) Amano, F.; Akamoto, C.; Ishimaru, M.; Inagaki, S.; Yoshida, H. Pressure-Induced Dehydrogenative Coupling of Methane to Ethane by Platinum-Loaded Gallium Oxide Photocatalyst. *Chem. Commun.* **2020**, *56* (47), 6348–6351.

(37) Shimura, K.; Yoshida, T.; Yoshida, H. Photocatalytic Activation of Water and Methane over Modified Gallium Oxide for Hydrogen Production. *J. Phys. Chem. C* **2010**, *114* (26), 11466–11474.

(38) Yuliati, L.; Itoh, H.; Yoshida, H. Photocatalytic Conversion of Methane and Carbon Dioxide over Gallium Oxide. *Chem. Phys. Lett.* **2008**, *452* (1–3), 178–182.

(39) Meng, L.; Chen, Z.; Ma, Z.; He, S.; Hou, Y.; Li, H. H.; Yuan, R.; Huang, X. H.; Wang, X.; Wang, X.; Long, J. Gold Plasmon-Induced Photocatalytic Dehydrogenative Coupling of Methane to Ethane on Polar Oxide Surfaces. *Energy Environ. Sci.* **2018**, *11* (2), 294–298.

(40) Wu, X. Y.; Tang, Z.; Zhao, X.; Luo, X.; John Pennycook, S.; Wang, S. L. Visible-Light Driven Room-Temperature Coupling of Methane to Ethane by Atomically Dispersed Au on WO_3. *J. Energy Chem.* **2021**, *61*, 195–202.

(41) Yi, Z.; Tang, Z.; Wu, X.; Huang, A.; Luo, X.; Xu, G. Q.; Zhu, Y.; Wang, S. L. Photocatalytic Oxidation of Methane to Methanol by Tungsten Trioxide-Supported Atomic Gold at Room Temperature. *Appl. Catal. B Environ.* **2021**, 120919.

(42) Park, S.; Jeong, J.; Fujita, K. I.; Yamamoto, A.; Yoshida, H. Anti-Markovnikov Hydroamination of Alkenes with Aqueous Ammonia by Metal-Loaded Titanium Oxide Photocatalyst. *J. Am. Chem. Soc.* **2020**, *142* (29), 12708–12714.

(43) Lee, S. Y.; Park, S. J. TiO2 Photocatalyst for Water Treatment Applications. *J. Ind. Eng. Chem.* **2013**, *19* (6), 1761–1769.

(44) Nakagawa, K.; Kajita, C.; Ide, Y.; Okamura, M.; Kato, S.; Kasuya, H.; Ikenaga, N.; Kobayashi, T.; Suzuki, T. Promoting Effect of Carbon Dioxide on the Dehydrogenation and Aromatization of Ethane over Gallium-Loaded Catalysts. *Catal. Letters* **2000**, *64*, 215–221.

(45) P. Berteau, S. C. and B. D. Role of the Acid-Base Properties of Aluminas, Modified γ-Alumina, and Silica-Alumina in 1-Butanol Dehydration. *Appl. Catal.* **1987**, *31*, 361–383.

(46) Piña-Pérez, Y.; Tzompantzi-Morales, F.; Pérez-Hernández, R.; Arroyo-Murillo, R.; Acevedo-Peña, P.; Gómez-Romero, R. Photocatalytic Activity of Al_2O_3 Improved by the Addition of Ce^{3+}/Ce^{4+} Synthesized by the Sol-Gel Method. Photodegradation of Phenolic Compounds Using UV Light. *Fuel* **2017**, *198*, 11–21.

(47) Tzompantzi, F.; Piña, Y.; Mantilla, A.; Aguilar-Martínez, O.; Galindo-Hernández, F.; Bokhimi, X.; Barrera, A. Hydroxylated Sol-Gel Al_2O_3 as Photocatalyst for the Degradation of Phenolic Compounds in Presence of UV Light. *Catal. Today* **2014**, *220–222*, 49–55.

(48) Li, H.; Bian, Z.; Zhu, J.; Huo, Y.; Li, H.; Lu, Y. Mesoporous Au/TiO_2 Nanocomposites with Enhanced Photocatalytic Activity. *J. Am. Chem. Soc.* **2007**, *129* (15), 4538–4539.

(49) Wang, S.; Gao, Y.; Miao, S.; Liu, T.; Mu, L.; Li, R.; Fan, F.; Li, C. Positioning the Water Oxidation Reaction Sites in Plasmonic Photocatalysts. *J. Am. Chem. Soc.* **2017**, *139* (34), 11771–11778.

(50) Saqlain, M. A.; Hussain, A.; Siddiq, M.; Ferreira, A. R.; Leitão, A. A. Thermally Activated Surface Oxygen Defects at the Perimeter of Au/TiO_2: A DFT+U Study. *Phys. Chem. Chem. Phys.* **2015**, *17* (38), 25403–25410.

(51) Horn, M.; Schwerdtfeger, C. F.; Meagher, E. P. Refinement of the Structure of Anatase at Several Temperatures. *Zeitschrift für Krist.* **1972**, *136* (273–281).

(52) Baur, W. H.; Khan, A. A. Rutile-Type Compounds . IV . SiO_2 , GeO_2 and a Comparison with Other Ruffle-Type Structures. *Acta Cryst.* **1971**, *27*, 2133–2139.

(53) Owen, E. A.; Yates, E. L. XLI. Precision Measurements of Crystal Parameters . *London, Edinburgh, Dublin Philos. Mag. J. Sci.* **1933**, *15* (98), 472–488.

(54) Kimura, K.; Naya, S. I.; Jin-Nouchi, Y.; Tada, H. TiO_2 Crystal Form-Dependence of the Au/TiO2 Plasmon Photocatalyst's Activity. *J. Phys. Chem. C* **2012**, *116* (12), 7111–7117.

(55) Schwartz, V.; Mullins, D. R.; Yan, W.; Zhu, H.; Dai, S.; Overbury, S. H. Structural Investigation of Au Catalysts on TiO_2-SiO_2 Supports: Nature of the Local Structure of Ti and Au Atoms by EXAFS and XANES. *J. Phys. Chem. C* **2007**, *111* (46), 17322–17332.

(56) Jo, S.; Verma, P.; Kuwahara, Y.; Mori, K.; Choi, W.; Yamashita, H. Enhanced Hydrogen Production from Ammonia Borane Using Controlled Plasmonic Performance of Au Nanoparticles Deposited on TiO_2. *J. Mater. Chem. A* **2017**, *5* (41), 21883–21892.

(57) Tanaka, A.; Sakaguchi, S.; Hashimoto, K.; Kominami, H. Preparation of Au/TiO_2 with Metal Cocatalysts Exhibiting Strong Surface Plasmon Resonance Effective for Photoinduced Hydrogen Formation under Irradiation of Visible Light. *ACS Catal.* **2013**, *3* (1), 79–85.

(58) Tanaka, A.; Hashimoto, K.; Kominami, H. Preparation of Au/CeO_2 Exhibiting Strong Surface Plasmon Resonance Effective for Selective or Chemoselective Oxidation of Alcohols to Aldehydes or Ketones in Aqueous Suspensions under Irradiation by Green Light. *J. Am. Chem. Soc.* **2012**, *134* (35), 14526–14533.

(59) Mateo, D.; Morlanes, N.; Maity, P.; Shterk, G.; Mohammed, O. F.; Gascon, J. Efficient Visible-Light Driven Photothermal Conversion of CO_2 to Methane by Nickel Nanoparticles Supported on Barium Titanate. *Adv. Funct. Mater.* **2021**, *31* (8), 2008244.

(60) Takami, D.; Yamamoto, A.; Yoshida, H. Dry Reforming of Methane over Alumina-

Supported Rhodium Catalysts at Low Temperatures under Visible and near-Infrared Light. *Catal. Sci. Technol.* **2020**, *10*, 5811–5814.

(61) Takeda, K.; Yamaguchi, A.; Cho, Y.; Anjaneyulu, O.; Fujita, T.; Abe, H.; Miyauchi, M. Metal Carbide as A Light-Harvesting and Anticoking Catalysis Support for Dry Reforming of Methane. **2020**.

(62) Xie, Q.; Lei, T.; Miao, C.; Hua, W.; Yue, Y.; Gao, Z. Au/TiO2 for Ethane Dehydrogenation: Effect of Silica Doping. *Catal. Letters* **2020**, *150* (7), 2013–2020.

(63) Skorobogatov, G. A.; Dymov, B. P.; Pogosyan, Y. I.; Khripun, V. K.; Tschuikow-Roux, E. P. Molecular, Thermodynamic, and Kinetic Parameters of the Free Radical C 2H5. in the Gas Phase. *Russ. J. Gen. Chem.* **2003**, *73* (1), 75–84.

5 General Conclusion

In the study described in this dissertation, metal oxide photocatalysts with the focus on the gallium oxide as a stable semiconductor photocatalyst has been developed for the photocatalytic NOCM in a flow reactor under the mild reaction conditions of nearly room temperature and atmospheric pressure. The surface modification of the bare gallium oxide by depositing the single and dual-cocatalyst on its surface has been investigated to enhance its activity towards the photocatalytic NOCM. An attempt has been made to understand the mechanism of the NOCM over the semiconductor photocatalysts.

In Chapter 2, we described the NOCM over the bare gallium oxide (Ga_2O_3) and the palladium-loaded gallium oxide (Pd/Ga_2O_3) photocatalysts in a flow reactor. It was evidenced that NOCM can be promoted continuously for at least 5.5 h over the bare gallium oxide in a flow reactor at nearly room temperature (*ca.* 320 K) and atmospheric pressure. It was the first time a flow reactor was used to evaluate the reaction rates in the photocatalytic NOCM. Flow reactors are suitable for the measurements of exact and real-time reaction rates in contrast to the closed reactors. It was also found that loading of palladium cocatalyst on the gallium oxide photocatalyst was beneficial and a $Pd(0.5\ wt.\%)/Ga_2O_3$ sample showed selective NOCM with the production rates of ethane and hydrogen being 0.22 and 0.23 $\mu mol\ h^{-1}$, respectively and their ratio *R* being 0.96 after 5.5 of photoirradiation. The methane conversion was calculated to be 0.006 % within a short contact time of 0.8 s, which exceeded the thermodynamic limitation. Suitable reaction conditions were investigated and a moderate light intensity, a moderate concentration of methane in the feed gas, and higher flow rate of the feed gas were favorable for the NOCM over the Pd/Ga_2O_3 photocatalysts. Over some samples like Pt/Ga_2O_3 and Rh/Ga_2O_3, a very small amount of ethane and a very large amount of hydrogen was produced. The methane decomposition (MD) to form carbon and hydrogen was suggested to be the competitive reaction which can take place even at low temperatures like 320 K under the reaction conditions. Reaction mechanism for the formation of ethane and hydrogen in the NOCM and also for the formation of carbon in the MD were proposed and the suitable reaction conditions were explained based on this mechanism. The mechanism would provide some insight in developing the novel photocatalysts and their modification to suppress or inhibit the MD to promote the NOCM selectively.

In Chapter 3, we described the selective and stable photocatalytic NOCM over the palladium-bismuth dual cocatalyst loaded gallium oxide ($Pd\text{-}Bi/Ga_2O_3$) photocatalyst in a flow reactor at nearly room temperature (320 K) and atmospheric pressure. Over many dual-

cocatalyst loaded gallium oxide samples such as Pd-Rh/Ga_2O_3, non-equimolar production of ethane and hydrogen were observed and a side reaction of MD to form coke as discussed earlier took place and made the selectivity for the NOCM lower indicated by a small value of *R* over these samples. However, some Pd-Bi/Ga_2O_3 samples showed almost ideal equimolar production of ethane and hydrogen from methane meaning that the MD was suppressed or inhibited completely over the Pd-Bi/Ga_2O_3 photocatalyst. The Pd(0.18)-Bi/(0.18)Ga_2O_3 photocatalyst showed excellent stability for 100 h with the average selectivity for the NOCM being almost 100 % after the initial induction period, meaning that ethane and hydrogen were produced selectivity and continuously from methane and no side reaction occurred. Its recyclability was also tested and the activity as well as the selectivity was intact for at least 3 cycles suggesting that the photocatalyst is stable under the reaction conditions and was not deactivated. This is the first report of long-time photocatalytic NOCM in a flow reactor. The methane conversion (0.033%) exceeded the thermodynamic limitation within a short contact time of 0.8 s and the apparent quantum efficiency was 0.2 % over the optimized Pd(0.18)-Bi(0.05)/Ga_2O_3 sample with the production rates of ethane and hydrogen of 1.10 and 1.24 μmol h^{-1}, respectively, which is one of the best records in literature under similar conditions using a flow reactor.

Metal oxide photocatalysts like TiO_2 and CeO_2 were not stable under the reductive reaction conditions of the NOCM since no hydrogen was observed with these samples meaning that these samples were possibly reduced by the hydrogen. The color of the bare TiO_2 sample varied from white to blue during the reaction test indicating its reduction during the reaction. Thus, the stability of the photocatalyst under the reductive reaction conditions is a perquisite for it to be active and stable for the photocatalytic NOCM.

It was also clearly demonstrated the photocatalytic production rates depend not on the catalyst weight but on the irradiation area of the flow reactor. Thus, the way of expressing the photocatalytic production rate per photocatalyst weight (μmol $g_{catalyst}^{-1}$ h^{-1}) or metal weight (μmol g_{metal}^{-1} h^{-1}) commonly used in recent literatures is not a correct convention to compare the photocatalytic activities of various photocatalysts. Instead, other factors such as the apparent quantum efficiency (AQE) should be employed.

Further, the physical mixture of the Pd/Ga_2O_3 sample and the Bi/Ga_2O_3 sample showed better activity and selectivity for the NOCM than those with the individual samples although the Pd and Bi species were located on the different Ga_2O_3 particles. Similarly, the activity and selectivity for the NOCM with a Pd/Ga_2O_3 sample diluted (physically mixed) with equal weight of Ga_2O_3 were nearly same as those with the Pd/Ga_2O_3 sample itself. These results suggested

that an interparticle mass transfer (transfer of methyl radical and proton) and an interparticle charge transfer (electron transfer) should take place in the present system. This is an important finding in the development of photocatalysis. The interparticle electron transfer will be beneficial to design a suitable architectural structure of the photocatalyst where the separate location of two cocatalysts is desired to minimize the recombination of photogenerated charge carriers and to suppress the undesired reverse reaction of products. On the other hand, a physical mixture of the two photocatalysts can be designed where one component can generate methyl radicals effectively while the other component can act as a coupling site of these radicals avoiding further reactions of radicals (such as decomposition in the NOCM and further oxidation in the OCM; etc.) exploiting the interparticle methyl radical transfer. Increasing the proximity of the Pd and Bi species resulted in better activity and better selectivity in the physical mixtures of Pd/Ga_2O_3 and Bi/Ga_2O_3 and the performance of the co-impregnated sample was only slight better that the tight-contacted mixture (TCM) sample meaning that independently deposited Pd and Bi could enhance the performance. Although we could not rule out the possibility of formation of mixed species like alloy or intermetallic nanoparticles of Pd and Bi species on the Ga_2O_3 particle, such mixed species could not be detected by the spectroscopic analysis (TEM and STEM-EDX) and XRD even in the higher loading amount sample.

Based on above results and discussion, a tentative mechanism is proposed for the NOCM over the $Pd\text{-}Bi/Ga_2O_3$ photocatalyst where gallium oxide acted as a semiconductor photocatalyst, Bi species as coupling sites of methyl radicals to form ethane and to suppress their further dehydrogenation to coke, and Pd species as sites to form reductive hydrogen. The closed location of Pd and Bi sites was beneficial for the effective inter-particle transfer of methyl radicals and electrons.

Another important finding was that the selectivity for the NOCM increased with an increase in the production rates (or activity). A more active photocatalyst can produce a large number of methyl radicals from methane by hole oxidation and provide a high surface concentration of methyl radicals which would result in effective collision giving higher coupling rate of methyl radicals to produce ethane increasing the selectivity for the NOCM. On the contrary, a less active photocatalyst will give less methyl radicals upon photoirradiation and thus the probability of the effective collision will also be less resulting in their further dehydrogenation to form carbon decreasing the selectivity for the NOCM. A dual-cocatalyst modified semiconductor photocatalyst approach can be extended to other photocatalysts and novel dual-cocatalyst would be explored in the photocatalytic NOCM.

In Chapter 4, attempts have been made for the photocatalytic direct conversion of ethane under non-oxidative reaction conditions to useful chemicals. *n*-Butane, ethene, and methane were found to be the main hydrocarbon products with hydrogen production upon photoirradiation when ethane was fed as the reactant. Like NOCM, the reduction resistant property is a prerequisite for a photocatalyst to be stable for photocatalytic direct ethane conversion. Gallium oxide which is a stable photocatalyst in the photocatalytic NOCM was also active in the photocatalytic direct ethane conversion and produced *n*-butane, ethene, and hydrogen in the stoichiometric ratio. Loading of Au increased the yield and an Au(0.4)/Ga_2O_3 sample showed production rate of *n*-butane of 0.65 μmol h^{-1}, which was 12 times higher than that over the bare Ga_2O_3 sample along with hydrogen production from ethane and the non-oxidative coupling of ethane (NOCE) was the main reaction pathway with the selectivity of *n*-butane being 89 %. Bare TiO_2 showed a very low yield because it was not stable and was reduced under reaction conditions of photocatalytic ethane conversion. Loading of Au also changed the performance of the bare TiO_2 sample drastically and an Au(0.2)/P-25 sample gave a higher production rate of *n*-butane of 0.92 μmol h^{-1} with the selectivity of 92 % and the moderate ratio of hydrocarbon to hydrogen production ($R_{HC/H2}$) of 1.5 after 5.5 h of photoirradiation at nearly room temperature (*ca.* 320 K) and atmospheric pressure. The NOCE was also the major reaction pathway with the Au/TiO_2 samples. Thus, Au is an efficient cocatalyst for the photocatalysts employed in both the NOCM and the NOCE. The apparent quantum efficiency (AQE) for *n*-butane formation over the Au(0.2)/TiO_2 sample was 0.02 %. The yield was 0.029 % which exceeded the thermodynamic equilibrium conversion. Reaction tests with the optical filter revealed that the SPR of the Au nanoparticles didn't contribute to the reaction without excitation of TiO_2 semiconductor photocatalyst. The formation of *n*-butane is explained by the NOCE, which is the major reaction pathway of product formation in the present study. The reaction mechanism of photocatalytic NOCE would be similar to photocatalytic NOCM. However, the mechanism of ethene formation was not clear and a possibility of photothermal dehydrogenation of ethane to ethene over supported Au catalysts can be expected. In the present study, gold was found to be an efficient cocatalyst since both Au/Ga_2O_3 and Au/TiO_2 photocatalysts showed good activity for butane formation via NOCE. Thus, further gold-loaded photocatalysts will be developed for the photocatalytic direct ethane conversion. Surprisingly, Pd/Ga_2O_3 and Pd-Bi/Ga_2O_3 samples as the efficient photocatalysts for the photocatalytic NOCM were not active for photocatalytic NOCE under the present reaction conditions. This result suggests that the properties important for the photocatalytic NOCE are not same as those of photocatalytic NOCM and the photocatalyst for the NOCM

can always not be used the photocatalytic NOCE. This important aspect will be helpful in the mechanical understanding of the photocatalytic NOCE.

In conclusion, we developed the performance of gallium oxide photocatalyst for the NOCM by depositing cocatalysts on its surface. The ethane production rate was increased more than 21 times with the Pd-Bi/Ga_2O_3 photocatalyst in comparison to the bare Ga_2O_3. High selectivity (nearly 100%) and long-term stability (100 h) was obtained for the photocatalytic NOCM. Tentative mechanism was proposed where possibility of the interparticle transfer in the photocatalytic system is discussed. Another important finding of a high selectivity with a high activity of the photocatalyst for the NOCM is found. The non-oxidative ethane conversion was also attempted and *n*-butane, ethene, methane and hydrogen were found to be the main products. The photocatalytic NOCE was the major reaction pathway for the product formation over the Au/Ga_2O_3 and Au/TiO_2 photocatalysts with the selectivity of *n*-butane formation being 89 % and 80-96 %, respectively. These observations and findings contributed significantly in the field of the photocatalytic non-oxidative methane and ethane conversion.

List of Publications

Chapter 2

1. Non-oxidative coupling of methane over Pd-loaded gallium oxide photocatalysts in a flow reactor; Surya Pratap Singh, Akihiko Anzai, Satoru Kawaharasaki, Akira Yamamoto, Hisao Yoshida, *Catalysis Today*, **2021**, *375*, 264-272.

Chapter 3

1. A Pd-Bi dual-cocatalyst-loaded gallium oxide photocatalyst for the selective and stable nonoxidative coupling of methane; Surya Pratap Singh, Akira Yamamoto, Eri Fudo, Atsuhiro Tanaka, Hiroshi Kominami, Hisao Yoshida, *ACS Catalysis*, **2021**, *11*, 13768-13781.

Chapter 4

1. Nonoxidative coupling of ethane with gold loaded photocatalysts; Surya Pratap Singh, Akira Yamamoto, Hisao Yoshida, *Catalysis Science & Technology*, **2022**, *published online*, DOI: 10.1039/D1CY02193A.

1. Non-oxidative coupling of methane over Pd-loaded gallium oxide photocatalysts in a flow reactor;
Surya Pratap Singh, Akihiko Anzai, Satoru Kawaharasaki, Akira Yamamoto, and Hisao Yoshida
(Catalysis Today, Sep. 2021, Volume 375, pages 264-272, doi: 10.1016/j.cattod.2020.04.023).
The final publication is available at Elsevier via https://doi.org/10.1016/j.cattod.2020.04.023.

2. A Pd-Bi dual-cocatalyst-loaded gallium oxide photocatalyst for selective and stable nonoxidative coupling of methane;
Surya Pratap Singh, Akira Yamamoto, Eri Fudo, Atsuhiro Tanaka, Hiroshi Kominami, Hisao Yoshida
(ACS Catalysis, Oct 2021, Volume 11, pages 13768-13781, doi: 10.1021/acscatal.1c03786).
The final publication is available at ACS Publications via https://doi.org/10.1021/acscatal.1c03786.

3. Nonoxidative coupling of ethane with gold loaded photocatalysts;
Surya Pratap Singh, Akira Yamamoto, and Hisao Yoshida
(Catalysis Science & Technology, 2022, advance article, first published online on 14 Jan 2022).
The final publication is available at ACS Publications via https://doi.org/10.1039/D1CY02193A.